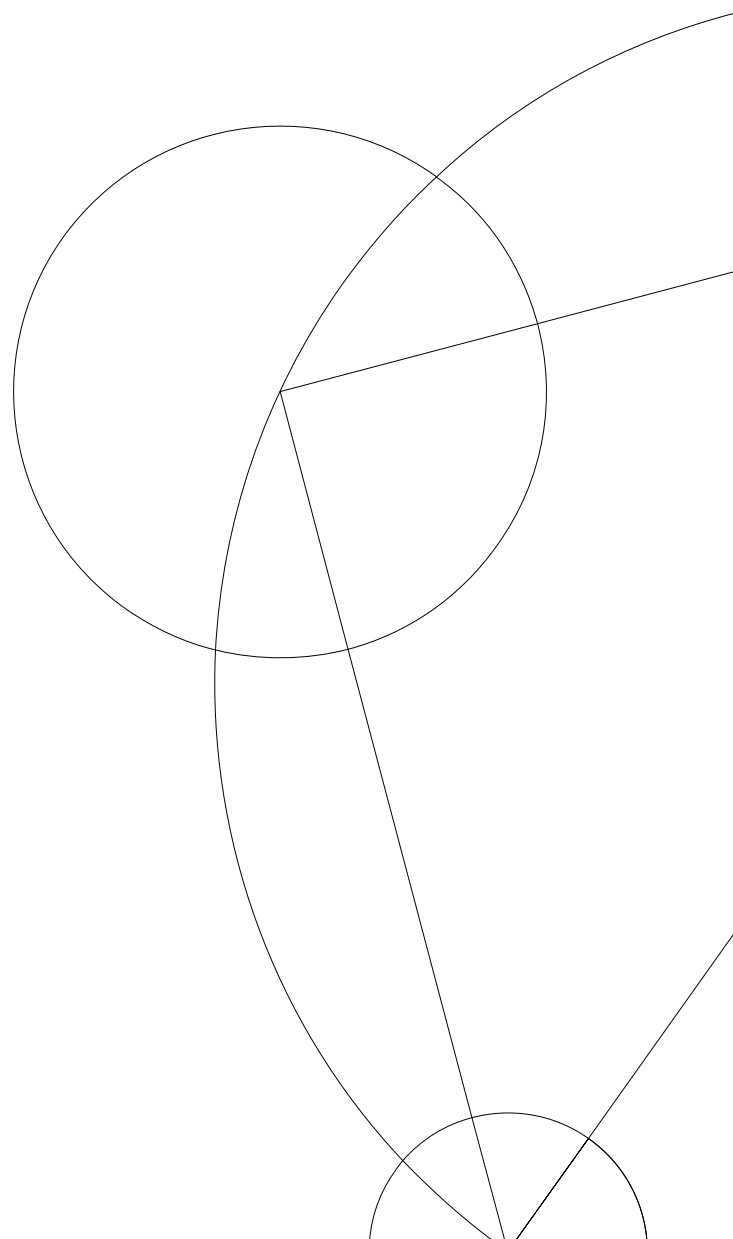## PhD Thesis

Jesper Mirsa Skottfelt

Improving Lucky Imaging Photometry
Using the Two-Colour EMCCD Instrument at the Danish 1.54m telescope

Supervisor: Uffe Gråe Jørgensen

November 3, 2014

Improving Lucky Imaging Photometry

Jesper Mirsa Skottfelt

Niels Bohr Institute

University of Copenhagen

A thesis submitted for the degree of

Philosophiæ Doctor

November 3, 2014

Abstract

For most ground-based optical and near-infrared telescopes today, seeing is the limiting factor in spatial resolution. Turbulence in the layers of the atmosphere distorts the wavefront of light coming from astronomical objects and effectively smears out the signal over a larger area in the focal plane, called the seeing disc. Even at the best observatory sites, located at several kilometres above sea level, the seeing rarely falls below $0\rlap{.}''5$, and a seeing below $1''$ is considered to be good. For comparison a seeing of $1''$ corresponds to the resolution limit of a 10 cm telescope. Adaptive optics systems can be used to mitigate the effects of the atmospheric turbulence, but these systems are very complicated and expensive and therefore not cost-effective for smaller telescopes.

Another solution for this problem is the use of high frame-rate imaging. At very short exposure times ($\sim$ 10 ms) it is possible to make snapshots of the wavefront before it is changed to a new configuration by the atmospheric turbulence. By analysing the speckle pattern in each snapshot, one may counteract the atmospheric disturbances by stacking the brightest speckles on top of each other and thus improve the spatial resolution. Even using longer exposure times ($\sim$ 100 ms) this method can be used to mitigate the effect of image motion created by atmospheric turbulence.

The Lucky Imaging technique makes use of the fact that there is some probability that the wavefront on some of these snapshots has traverse the atmosphere almost unperturbed. If only these snapshots are stacked, it is possible to achieve very high spatial resolution.

Due to the readout noise it is not feasible to use conventional CCDs for high frame-rate imaging, unless bright sources are observed. In an electron multiplying CCD, or EMCCD, the signal is cascade amplified before it is read out, thus rendering the readout noise negligible compared to the signal. EMCCDs thus makes high frame-rate imaging feasible, even when observing faint objects.

In this thesis I describe the Two-Colour EMCCD Instrument (TCI) that has been designed for the SONG 1m telescopes and for the Danish 1.54m telescope. The motivation behind the TCI is to enable simultaneous red and visual band observation, thus providing instantaneous colour information and maximising the de-

i

tected wavelength range without losing spatial information.

My main contribution has been developing the software for controlling the TCI and reducing the EMCCD data. This software includes, for instance, a fully automated routine for observing and processing microlensing events, such that light curves are automatically uploaded to a central server.

With the high spatial resolution that can be achieved with the TCI, it has, among other things, been possible to obtain high precision time-series photometry of crowded fields. I detail the discovery of two previously unknown variable stars in the Galactic globular cluster NGC 6981, and the search for variable stars in the five metal-rich ([Fe/H] > -1) globular clusters: NGC 6388, NGC 6441, NGC 6528, NGC 6638, NGC 6652.

Danish summary

For de fleste jordbaserede optiske og nær-infrarøde telescoper i dag, er *seeing* den begrænsende faktor i rumlig opløsning. Turbulens i de atmospæriske lag forstyrrer lyset fra astronomiske objekter og spreder det ud over et større område, og det er bredden af dette område man kalder seeing. Selv på observatorier placeret flere kilometer over havets overflade, opnår man sjældent en seeing bedre end $0\rlap{.}{''}5$ og er den bedre end $1''$ anses den for at være god. Til sammenligning svarer en seeing på $1''$ til den højeste rumlige opløsning man kan opnå med et 10 cm teleskop.

Adaptiv optik (AO) kan bruges til at modvirke effekterne af den atmosfæriske turbulens. Dette gøres ved at analysere bølgefronten med få millisekunders mellemrum og korrigere et spejl, der ligger i lysets bane, mens observationerne foregår. AO systemer er dog meget komplicerede og dyre, og derfor ikke rentable for mindre teleskoper.

En anden løsning på dette problem er at lave korte exponeringer hurtigt efter hinanden. Ved meget korte exponeringstider ($\sim 10\,\mathrm{ms}$) er det muligt at fastfryse bølgefronten, før den bliver ændret af den atmosfæriske turbulens. Ved at analysere hver af disse korte exponeringer, kan man modvirke de atmosfæriske forstyrrelser og derved opnå en højere rumlig opløsning når man lægger exponeringerne sammen. Selv ved længere exponeringstider ($\sim 100\,\mathrm{ms}$) er det muligt at begrænse effekten af billedbevægelse skabt af turbulens i atmosfæren.

I en lille del af disse korte exponeringer, vil bølgefronten være nået hele vejen igennem atmosfæren stort set uden at blive forstyrret. Hvis man kun lægger disse 'heldige' exponeringer sammen, kan man opnå meget høj opløsning. Denne metode kaldes *Lucky Imaging*.

På grund af udlæsestøj giver det for det meste ikke mening at bruge konventionelle CCD'er til at lave korte exponeringer. I en elektron multiplicerende CCD (EMCCD) bliver signalet forstærket før det bliver læst ud, og det gør udlæsestøjen ubetydelig i forhold til signalet, selv ved meget korte exponeringer.

I denne afhandling beskriver jeg et to-farve EMCCD instrument, der er blevet designet til The Stellar Observation Network Groups (SONG) 1m teleskoper og det Danske 1.54m teleskop, samt det bidrag jeg har givet til instrumentets design, konstruktion og tests, og udvikling af pipeline- og reduktions-software.

Motivationen bag dette instrument er at muliggøre simultane observationer i det røde og visuelle bånd, og derved give øjeblikkelig farveinformation og maksimere de detekterede bølgelængder uden at miste rumlig opløsning. Instrumentet har nu været brugt til regelmæssige observationer i flere år, ved hjælp af den software jeg har udviklet specielt til dette formål.

Som en del af afhandlingen har jeg lavet en analyse af instrumentets ydeevne på det Danske teleskop. Denne viser, at den rumlige opløsning bliver forbedret med op til en faktor to, når man bruger Lucky Imaging metoden, og at en opløsning på under $0\farcs4$ kan opnås regelmæssigt. Det bliver desuden vist at instrumentet leverer en meget høj fotometrisk precision, især i områder, der er meget tæt besat af stjerner.

Instrumentet skal hovedsageligt bruges til at finde planeter om andre stjerner end Solen, ved hjælp af en metode kaldet gravitationel mikrolinsning. Det er dog også blevet brugt til en række andre videnskabelige programmer, som for eksempel fundet af to ringe rundt om det lille asteroide-lignende objekt (10199) Chariklo. Derved blev Chariklo det mindste objekt i solsystemet, hvorom ringe er observeret.

Afhandlingen beskriver også de første resultater fra et studie, hvor et antal kuglehobe er blevet observeret regelmæssigt over en periode på over et år. Selvom de fleste af disse kuglehobe er velstuderede, er jeg i stand til at finde en lang række hidtil ukendte variable stjerner i disse, ved at udnytte den høje opløsning og præcise fotometri som to-farve instrumentet leverer.

Acknowledgements

Writing this thesis has only been possible due to a number of persons, for whom I owe much gratitude.

First of all I would like to thank my supervisor Uffe Gråe Jørgensen for giving me this opportunity, for all his help and advice, and his ability to make things happen.

A special thanks to Dan Bramich for all his help and inspiration, and for believing in my ideas and helping me to accomplish them.

Further I would like to thank

Roberto Figuera, Noe Kains, and Armando Arellano for introducing me to the wonders of globular clusters,

Michael I. Andersen, Per Kjærgaard, Anton Sørensen, Kennet Harpsøe and Niels Michaelsen for interesting and lively discussions about instrumentation, software and statistics,

Markus Hundertmark and Rachel Street for help and guidance with pipeline and reduction issues,

the people of MiNDSTEp for collecting data, publishing articles and assisting me in getting the two-color instrument and my software to work. Some of these people are, in no order of importance: Martin Dominik, Colin Snodgrass, John Sourthworth, Diana Juncher, Andrius Popovas, Troels Haugbølle, Heidi Korhonen, Simona Ciceri, Markus Rabus, Tobias Hinse, Christine Liebig, Sebastiano Calchi Novati, Luigi Mancini, Valerio Bossa, Jean Surdej, and Frederic Hessman,

the SONG project for funding, and the people tirelessly working on improving the SONG telescopes, including Frank Grundahl, Mads F. Andersen, Søren Frandsen, Eric Weiss, Hans Kjeldsen, and Jørgen Christensen-Dalsgaard,

Contents

List of Figures

List of Tables

Chapter 1

Introduction

For most ground-based optical and near-infrared (NIR) telescopes today, seeing is the limiting factor in spatial resolution. Turbulence in the layers of the atmosphere distorts the wavefront of light coming from astronomical objects and effectively smears out the signal over a larger area in the focal plane, called the seeing disc. In order to mitigate the effects of the atmospheric distortion, observatories are therefore often placed at sites located several kilometres above sea level. However, even at the best sites the seeing rarely falls below $0\rlap{.}''5$, measured in the full width at half maximum (FWHM) of the point spread function (PSF), and a seeing below $1''$ is considered to be good. The theoretical limit for the spatial resolution of a telescope is known as the diffraction limit and it can be calculated as $1.22\lambda/D$, where λ is the wavelength and D is the telescope diameter. A seeing of $1''$ thus corresponds to the diffraction limit of a $10\,\mathrm{cm}$ telescope at $500\,\mathrm{nm}$.

Adaptive optics (AO) systems can be used for correcting the wavefront, by performing a real-time analysis of a bright nearby star, or a laser guide star. AO systems on large telescopes (>5m) have been shown to reach spatial resolutions down to a few tens of milliarcseconds (mas), but they are very complicated and expensive systems and they are therefore not cost-effective for smaller telescopes. An alternative method for improving the spatial resolution is high frame-rate imaging. At very short exposure times ($\sim 10\,\mathrm{ms}$) it is possible to make snapshots of the wavefront before it is changed to a new configuration by the atmospheric turbulence. By analysing the speckle pattern in each snapshot, one may counteract the atmospheric disturbances by stacking the brightest speckles on top of each other and thus improve the spatial resolution. This technique, known as speckle imaging (or just shift-and-add), is based on the work by Fried (1966). Even using longer exposure times ($\sim 100\,\mathrm{ms}$) it is possible to mitigate the effect of image motion created by atmospheric turbulence, by doing shift-and-add.

In Fried (1978) it is shown that there is some probability of obtaining a lucky short exposure, i.e. an exposure where the wavefront has passed almost unperturbed

through the atmosphere. If only these few lucky frames are used, then it is possible to achieve very high spatial resolution; a technique known as Lucky Imaging. However, as this probability is inversely proportional to the telescope diameter, only very few lucky frames can be obtained on large telescopes.

Charge-couple devices (CCDs) are unsurpassed for visual and NIR observations as they provide spatial information, high quantum efficiency, and linear response. However, using conventional CCDs for high frame-rate imaging is only feasible for observing bright targets, due to the noise added in the readout process. This has changed with the invention of the Electron Multiplying CCD, or EMCCD. In an EMCCD the signal from each pixel is cascade amplified before it is read out. This renders the readout noise negligible compared to the signal, and faint sources are thus also observable with the high frame-rate technique. Performing Lucky Imaging using EMCCDs is described in numerous articles (e.g Mackay et al., 2004; Law et al., 2006), and by combining Lucky Imaging with an AO system, Law et al. (2009) were able to do diffraction limited imaging at the 5m Palomar telescope, thus reaching a spatial resolution of 35 mas FWHM at 700 nm.

The use of EMCCD data to do high precision photometry is an area that is just starting to be explored. We have developed a method were the best percentage exposures are combined into a high-resolution reference frame. Using this reference frame in a difference imaging analysis (DIA) of other observations, including those with suboptimal resolution, makes it possible to take advantage of the best possible spatial resolution at the same time as keeping the total number of photons, in order to give best possible S/N, leading to substantial improvements in analyses of dense stellar regions. EMCCD cameras available as off-the-shelf products provide an excellent opportunity to improve the spatial resolution, and thus perform precise time-series photometry of crowded fields on smaller telescopes.

Chapter 2 gives a short introduction to EMCCDs and high-frame rate imaging.

One area where the Lucky Imaging technique can be used, is for the detection of cool low-mass exoplanets. Of the exoplanet detection techniques, gravitational microlensing is currently the only technique capable of obtaining population statistics on cool low-mass planets. Detecting exoplanets down to Mars mass requires a photometric precision down to a few percent on Galactic bulge main-sequence stars. To do this it is necessary to separate them from brighter stars, and angular resolutions below $\sim 0.''4$ are thus necessary (Bennett et al., 2002). As it is not possible to reach such high resolutions from the ground using conventional CCD detectors (without an AO system), space mission like WFIRST (Wide-Field Infrared Survey Telescope, Spergel et al., 2013) are therefore widely considered to be the only way to obtain population statistics on cool low-mass planets (see Fig. 1.1).

However, by using the Lucky Imaging technique to improve the spatial resolution
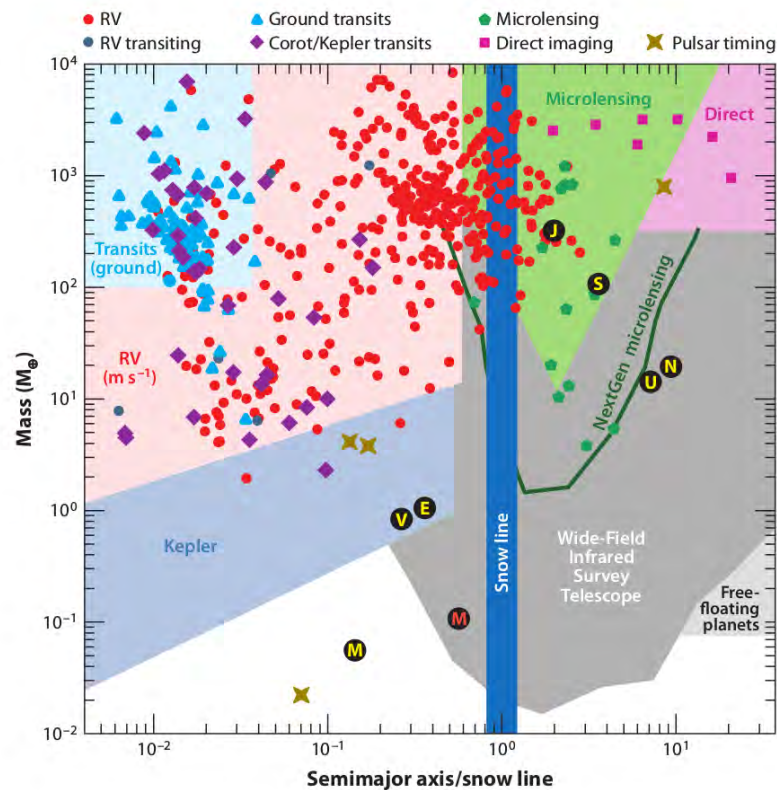
Figure 1.1: Reported exoplanets by detection technique as a function of mass and orbital separation relative to the snow line, as well as estimated discovery spaces for various methods and experiments (figure from Gaudi, 2012).

when doing follow-up observations of gravitational microlensing events, it might also be possible to reach that level of photometric precision.

Using EMCCD data for exoplanet detection is one of the cornerstones of the Stellar Observations Network Group (SONG) project, which will be part of the MiNDSTEp consortium operation (Dominik et al., 2010) to detects exoplanets using the gravitational microlensing method. The SONG project aims at establishing a network of 1m robotic telescopes around the globe, and for these telescopes a two-colour EMCCD instrument (TCI) has been developed.

The purpose of the TCI is to enable simultaneous red and visual band observations, thus providing instantaneous colour information and maximising the detected wavelength range without losing spatial information.

To test the capabilities of the TCI before the commissioning of the SONG telescope prototype, a single EMCCD camera, and then later a full copy of the TCI, was installed at the Danish 1.54m Telescope (DK154) at the ESO La Silla Ob-

servatory in Chile. Regular EMCCD operations have been running at the DK154 for several years, and the TCI is, to the best of our knowledge, the first routinely operated multi-colour instrument providing LI photometry.

In chapter 3 the Two-Colour Instrument is presented along with an analysis of its performance and some of the scientific results it has achieved.

The TCI at the DK154 have mainly been used for gravitational microlensing follow-up, which has resulted in several new exoplanets being published (e.g. Tsapras et al., 2014) or in the process of analysis, but other scientific programs have also been carried out. This has, for instance, lead to the discovery of two rings around the small asteroid-like object (10199) Chariklo (Braga-Ribas et al., 2014).

Another successful scientific program carried out with the TCI, is a variability study of the cores of dense Galactic globular clusters. This was started after the detection of two previously unknown variables stars in the well-studies globular cluster NGC 6981 (Skottfelt et al., 2013b, Chapter 4 of this thesis). The first results of this program is presented in Skottfelt et al. (2014a), that contains a search of variable stars in the five metal-rich ([Fe/H] > -1) globular clusters: NGC 6388, NGC 6441, NGC 6528, NGC 6638, NGC 6652. This study is presented in chapter 5 of this thesis.

Chapter 2

EMCCDs and high frame-rate imaging

EMCCDs, and the mathematical theory behind them, are described in great detail by in previous works (e.g. Mackay et al., 2001; Basden et al., 2004; Harpsøe et al., 2012a; Harpsøe et al., 2012b), and only a short introduction will be given here.

When a conventional Charged-Coupled Device (CCD) is read out, each row in the imaging area is shifted in turn to the serial, or readout, register and the pixels in each row are read-out successively through an output amplifier, where the electrons are converted into ADUs (Analog to Digital Unit). The lowest noise output amplifiers can determine the charge with a precision down to a few photons, but if one wants to speed up the readout frequency, the noise in the readout increases to tens or hundreds of electrons. It is therefore undesirable to do high frame-rate imaging of faint sources with a conventional CCD, as the signal would be lost in readout noise.

An EMCCD has an extended readout register, or EM register, that amplifies the signal before it is read out. This is done by shifting the charges in each step of the EM register with a significantly higher voltage than normally. Each time an electron is shifted, there is a small probability p_m that an impact ionisation will occur, resulting in an extra electron. This creates a cascade amplification over the length of the EM register (see Fig. 2.1)

The amplification of a single electron over m steps in the multiplication register, is given by the multiplicative gain

$$\gamma = (1 + p_m)^m \; .\tag{2.1}$$

Based on this, the probability density function (PDF) for a certain number of output electrons x given a number of input electrons n, can be estimated as

$$P(X = x \,|\, n) = x^{n-1} \frac{e^{-x/\gamma}}{\gamma^n \Gamma(n)} \; ,\tag{2.2}$$
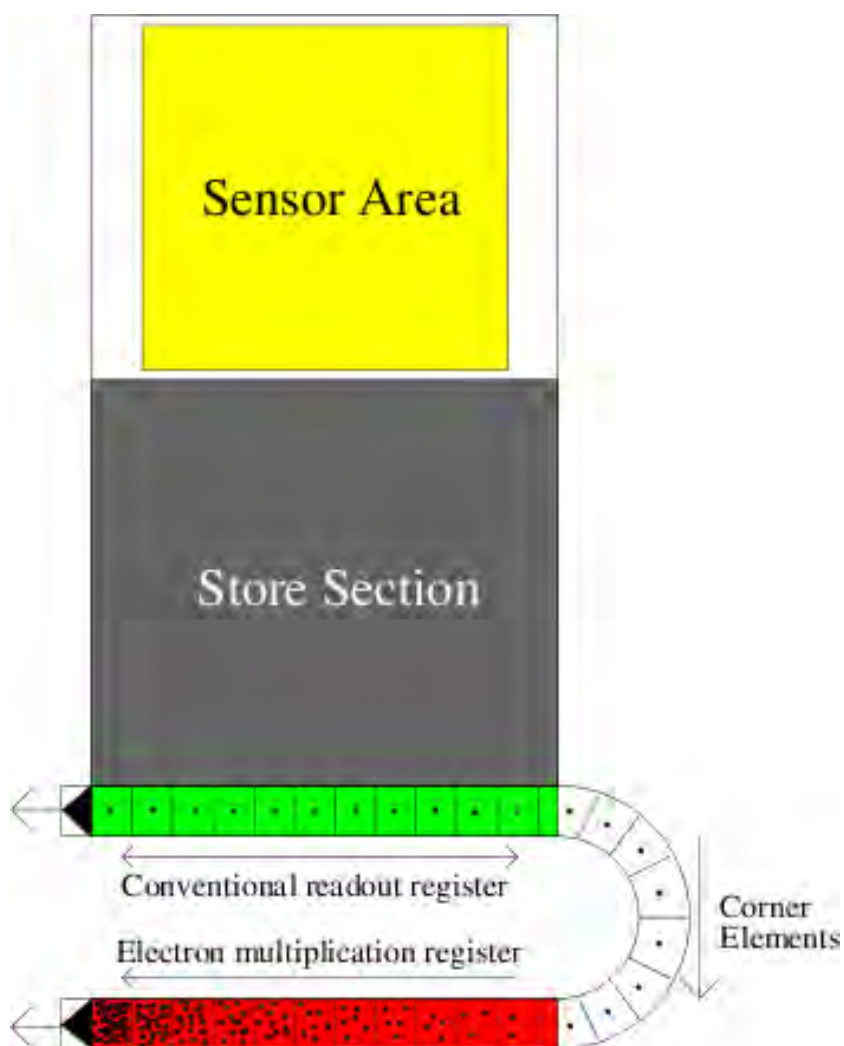
Figure 2.1: Schematic drawing of a frame transfer EMCCD. After exposure, the image is rapidly shifted into the storage area, where it is read out via the green serial register. The red register is an extension of the serial register, where the pixels are shifted with significantly higher voltages, hereby generating cascade amplification via impact ionisation. (Harpsøe et al., 2012a, figure 1).
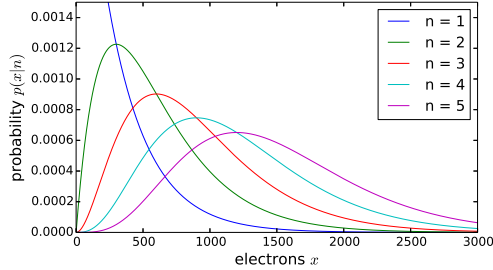
Figure 2.2: Plot of the Erlang distribution as defined in Eqn. 2.2 and for $\gamma = 300\,e^-$/photon. As γ is a scale parameter, it will only scale the numbers on the x-axis. It will not change the functional form (Adopted from Harpsøe et al., 2012b, figure 2).
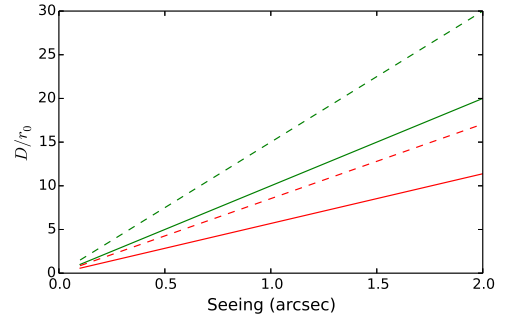
Figure 2.3: Plot of D/r_0 as function of seeing is plotted for 500 nm (green) and 800 nm (red) for a 1 m (solid line) and 1.5 m (dashed line) telescope.

where Γ is the gamma function. This distribution is known as the Erlang distribution and it is a special case of the gamma distribution.

A plot of the Erlang distribution for different values of n is shown in Fig. 2.2, illustrating that there are large overlaps between the possible outcomes.

In conventional CCDs the photon noise, or shot-noise, is given by the Poisson distribution, which means that the signal-to-noise ratio can be determined as S/N $= S/\sqrt{S}$. The stochastic nature of the cascade amplification contributes an extra factor of 2 to the variance, usually known as the excess noise factor. The S/N for the EMCCD therefore becomes

$$\text{S/N} = \frac{S}{\sqrt{2S}} \ . \tag{2.3}$$

Another drawback of the EMCCD is the signal coming from spurious charges. Spurious charges are electrons that arise in the CCD during the readout, as an effect of the vertical or horizontal shift operations. These events are usually rare (they only happen in a few percent of the pixels) and realease a single electron in each event. In conventional CCDs they are undistinguishable from the readout noise. However, for an EMCCD where all electrons are cascade-amplified, spurious charges give rise to a detectable signal. Unless the EMCCD is used for photon-counting purposes, the signal from the spurious charges is assumed to be negligible.

With the signal amplified in the EM register, for instance by a value of $\gamma = 300\,e^-$/photon, the readout noise becomes negligible even at high readout speeds.

EMCCDs thus make it feasible to do high frame-rate imaging, which has a number of advantages that we will discuss in the following.

By shifting and adding the individual exposures, it is possible to compensate the blurring effects of atmospheric disturbances and achieve a better spatial resolution. This method is known as speckle imaging, or just shift-and-add. Fried (1978) showed that the probability of obtaining a good short exposure (i.e. an exposure where the wavefront area over the aperture is less than 1 rad^2), is

$$P = 5.6 \exp\left(-0.1557(D/r_0)\right) \quad (\text{for } D/r_0 \geq 3.5), \tag{2.4}$$

where r_0 is the Fried parameter. The Fried parameter is a measure of the optical aberrations caused by atmospheric disturbances and is defined as the diameter of a circular area over which the rms of the wavefront aberrations is 1 rad. The Lucky Imaging technique makes use of this theory, by only stacking the few percent best frames to obtain very high spatial resolution. Shifting-and-adding some percentage of the best frames is referred to as *percentage selection.*

The improvement of the Strehl ratio using high frame-rate imaging was examined by Smith et al. (2009, hereafter S09). Strehl ratio is a measure of image quality defined as the ratio of the peak intensity in an observed image, to the maximum attainable intensity in a diffraction limited system. Using standard *V* and *I*-band observations of bright stars, S09 examined D/r_0 ratios between 3 and 30. For comparison, a plot of D/r_0 versus seeing for a 1 and 1.5 m telescope, is shown in Fig. 2.3.

At short exposure times, below 10 ms, S09 found that the Strehl ratio of the shift-and-added frames is between 2 and 3 times higher than stacked frames with no shifting. For a 1% selection the improvement is between 4 and 6, with a peak at $D/r_0 \sim 7$. The effect of the single frame exposure times, t, was also examined, though only for a 1% selection. Here the shortest exposure time, $t = 1$ ms, gave the best results with Strehl ratios of up to six times higher. At longer exposure times the improvement decreased, but even at $t = 640$ ms, the Strehl ratio was improved by a factor of two.

The very short exposure time that is used when doing high frame-rate imaging makes it possible to observe even quite bright objects without saturating the CCD. The required S/N for the fainter objects can then be reached by combining the required number of exposures at a later stage, thus achieving a very high dynamical range. This makes it possible to perform high precision photometry for both bright and faint stars in the same field, something that can be hard to obtain when doing conventional CCD imaging.

Chapter 3

Two-Colour EMCCD Instrument

3.1 Telescopes

The Two-Colour EMCCD Instrument was originally designed for the SONG telescope prototype, but in order to test the capabilities of the TCI, a copy was made for the DK154. A short introduction to the telescopes is given here.

3.1.1 Danish 1.54m Telescope

The DK154, built by Grubb-Parsons, was commisioned in 1979. The telescope is situated at the ESO La Silla Observatory, Chile ($70°44'662''$W $29°15'14''235$S), at an altitude of 2340 metres.

Since its commissioning, the telescope has been refurbished a number of times. In 2012, a complete overhaul of the electrical and mechanical systems was done by the Czech company Projectsoft[1]. A new telescope control system (TCS), also developed by Projectsoft, and other subsystems were also installed. It is thus now possible to control the telescope remotely, such that remote observations without on-site staff can be done.

The telescope has an off-axis equatorial mount and the optics are of a Ritchey-Chrétien design. The main instrument is the Danish Faint Object Spectrograph and Camera (DFOSC), which was installed in 1996 (Andersen et al., 1995), though since 2004 scaled down to exclude the spectroscopic capability. The DFOSC uses a 2K×2K thinned Loral CCD chip with a pixel scale of $0''4$/pix, exhibiting a FoV of $13'7 \times 13'7$.

---

[1]www.projectsoft.cz

3.1.2 SONG

The Stellar Observations Network Group (SONG) project aims at constructing a network of fully robotic 1m telescopes for doing time-domain astronomy, in particular asteroseismic observations and exoplanet studies (Grundahl et al., 2006; Grundahl et al., 2009; Grundahl et al., 2014). To ensure the continuous coverage of both northern and southern targets, eight telescope nodes are required, and these should be placed on existing observatory sites around the globe.

The prototype for the SONG telescope is delivered by the German company Astelco[2], while its two instruments are assembled at the workshops at Aarhus University (the spectrograph) and at University of Copenhagen (the TCI). The telescope is carried by an Alt-Az mount driven by magnetic torque motors ensuring fast pointing (up to $20°$ per second) with high precision (within $3''$ of the pointing model).

A detailed description of the SONG optical system, including schematics, is given in Grundahl et al. (2009), so only a short introduction will be given here. The 1m primary mirror is only 5 cm thick and employs an active correction system based on Shack-Hartmann measurements of bright stars. With this system the telescope will have nearly diffraction limited optics.

A high resolution spectrograph is installed at the Coudé focus. This will be used to do high precision radial-velocity measurements.

The TCI is installed at the Nasmyth focus and is part of the Nasmyth unit that also contains a de-rotator and an atmospheric dispersion corrector (ADC).

To take advantage of the diffraction limited optics, and the high frame-rate capabilities of the EMCCD cameras, a sampling of $0.''09$/pix was chosen. This will ensure a sampling better than 2 pixels of the *I*-band diffraction limit. With a seeing of $1''$, the D/r_0 ratio for the SONG telescope is between 5 and 6 at a wavelength of 800 nm. As described in Sect. 2, this is near the optimal regime for the Lucky Imaging method.

The SONG telescope prototype has been installed at the Observatory del Teide on Tenerife, Spain, and a second SONG node has been built in China.

3.2 Two-Colour Instrument

The motivation behind the Two-Colour Instrument was that it would provide instantaneous colour information about the observed objects and maximise the detected wavelengths without losing spatial information.

In 2009, a single Andor EMCCD camera was installed at an auxiliary port on the DK154, to be used for testing the capabilities of the TCI, in anticipation of the

---

[2]http://www.astelco.com/
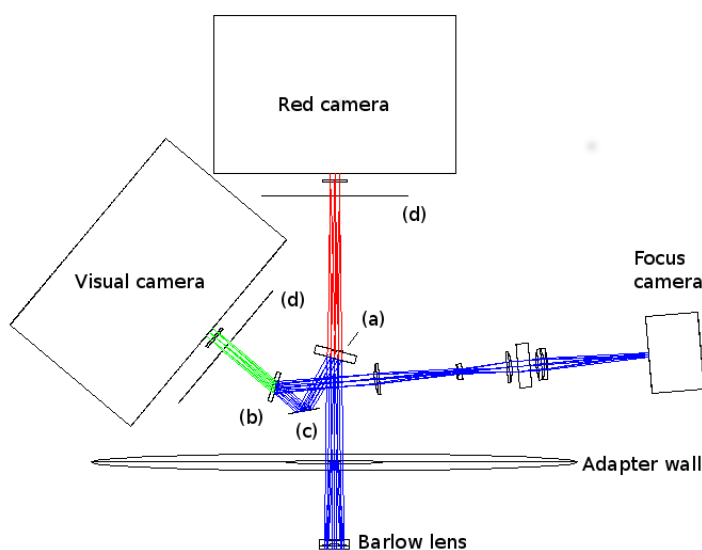
Figure 3.1: Optical design for the TCI at DK154. Here (a) is the red/vis dichoic, (b) is the vis/blue dichroic, (c) is the folding mirror, and (d) marks the filter wheels.

SONG commissioning. The camera was therefore equipped with a special long-pass filter with a cut-on wavelength of 650 nm (Thorlabs FEL0650), to mimic the transmission of the red/vis dichroic mirror in the TCI, and had a sampling of 0″.09/pix.

After a few years of successful testing it was decided in late 2012, to build and implement a full version of the TCI on the DK154.

3.2.1   Optical design

The TCI basically consists of two dichroic mirrors, two EMCCD cameras, and a focus system. The first (red/vis) dichroic mirror transmits the red band to one EMCCD camera (the 'red' camera), and reflects the visual-blue band towards the second dichroic mirror. Here the visual band is transmitted to the second EMCCD camera (the 'visual' camera), and the blue band is reflected towards the focus system. The focus system is described in Sect. 3.2.4.

In order to achieve the same sampling on the DK154 as on the SONG telescope, a Barlow lens is added to the system before the red/vis dichroic mirror. It was also necessary to add an extra folding mirror on the DK154 TCI after the red/vis dichroic mirror and to rearrange the cameras, in order to create a system that could be mounted at the auxiliary port on the DK154. The optical design for the TCI on the DK154 is shown in Fig. 3.1.

The SONG TCI has a filter wheel in front of each EMCCD camera. In the DK154

TCI there are no filter wheels installed, but room has been allocated for them, so that they can be installed at a later stage.

3.2.2 EMCCD camera

The Andor iXon+ 897 EMCCD was chosen as the detector for both the red- and the visual-band of the Two-Colour Instrument (TCI). The camera has an active imaging area of 512×512 pixels, and with the chosen pixel scale of $0\rlap{.}''09$/pix, this gives a field-of-view (FoV) of about $45'' \times 45''$. The EM readout amplifier has a maximum pixel readout rate of 10 MHz, and is thus able to readout ~ 35 full frames per second.

The typical readout noise at maximum readout rates is $\sim 50\,e^-$, but by using the EM gain, which can be as high as $\gamma = 1000\,e^-$/photon, the readout noise becomes negligible compared to the signal even at a single photon level, and the camera can thus be said to be photon counting. However, to protect the camera, Andor suggest that the EM gain is not set higher than $\gamma = 300\,e^-$/photon in normal operations, and that EM gain values above this are only used on special occasions.

The camera has a thermoelectric (Peltier) cooling system that can cool the camera down to -85°C. At this temperature the typical dark current in the camera is 0.001 e^-/pix/sec. The typical spurious charge rate is 0.005 e^-/pix/sec.

The camera is also equipped with a conventional readout amplifier with pixel readout rates of 3 or 1 MHz, and with a typical readout noise of 6 electrons for the latter.

The wavelength coverage goes from 300 nm to 1100 nm. The quantum efficiency (QE) curve for the camera is plotted in Fig. 3.2.

3.2.3 Instrument efficiency

The efficiency of the TCI has been calculated based on the supplied transmission/reflection curves of the dichroics and assuming that the telescope has a transmission efficiency of 65%. For the TCI on the DK154, a small loss in the Barlow lens ($\sim 3\%$) would have to be taken into account, but this has not been included here. The plot in the top of Fig. 3.2 shows the reflection and transmission efficiency of the dichroics, the QE of the Andor EMCCD camera, and the QE for the Sony ICX285 CCD chip used by the focus camera (see Sect. 3.2.4).

In the middle panel of Fig. 3.2 the relevant efficiencies are multiplied with the QE of the cameras and the transmission efficiency of the telescope to give the instrument efficiency for the three channels. The lower panel of the figure shows the normalised passbands of the Johnson-Cousins *UBVRI* photometric system (Bessell, 1990) and the sensitivity of the Sloan Digital Sky Survey (SDSS) camera through the $u'g'r'i'z'$ filter system (Gunn et al., 1998) for comparison purposes.
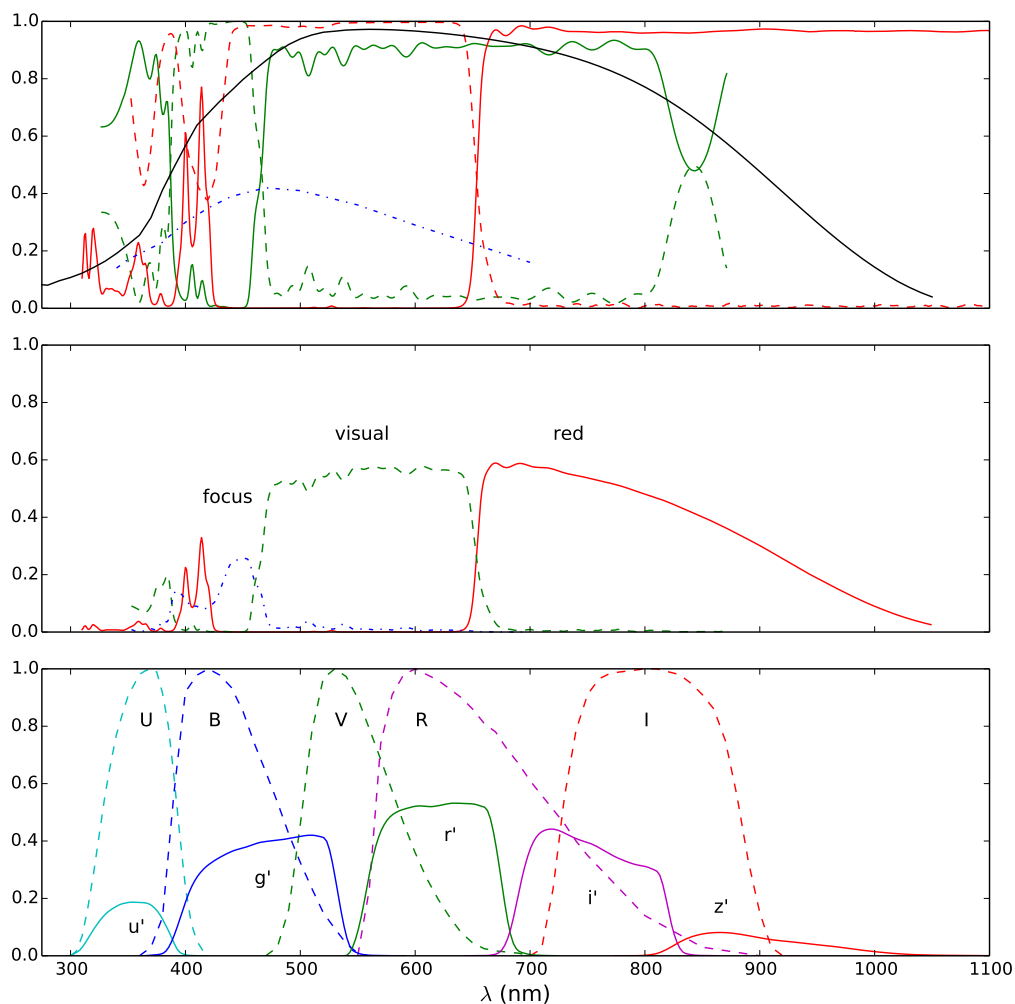
Figure 3.2: The top panel shows the transmission (solid) and reflection (dashed) of the red/vis (red) and vis/blue (green) dichroics, respectively, the QE of the EM-CCD camera (solid black), and the QE of the focus camera (dot-dashed blue). The middle panel shows the instrument efficiency of the red (solid red line), visual (dashed green line), and focus channel (blue dot-dashed line). In the bottom panel the normalised passbands of the Johnson-Cousins *UBVRI* photometric system (dashed lines) are plotted along with the system sensitivity of the SDSS $u'g'r'i'z'$ camera (solid lines). The latter is based on a sensitivity determination made by Jim Gunn in June 2001, which is available as a FITS file at `http://www.sdss3.org/instruments/camera.php`.

The passbands of the TCI are defined by the dichroics and are significantly wider than the standard photometric filter systems, with effective bandwidths of ~ 250 nm and ~ 185 nm in the red and visible channel, respectively.

The red/vis dichroic has a cross-over wavelength $\lambda_c^r \simeq 655$ nm and the red channel therefore corresponds roughly to a combination of the SDSS $i' + z'$ filters. There is a leak in the dichroic between 350-430 nm, which will influence the photometric output. The effect of this can be eliminated by using a long-pass filter in front of the red camera.

With a $\lambda_c^v \simeq 466$ nm for the vis/blue dichroic, the visual channel does not match any of the standard photometric systems. The cut-on wavelength is right in the middle of the SDSS g' filter, and the cut-off wavelength $\lambda_c^r \simeq 655$ nm is about 40 nm from the red end of the SDSS r' filter at 695 nm. There is also a contribution to the visual channel for wavelengths shorter than 390 nm. Again this can be eliminated by using a (long-pass) filter in front of the visual camera.

Only a small part of the light, $\sim 390 - 460$ nm, is reflected towards the focus system by the vis/blue dichroic. The loss in the focus optics is not accounted for, but the efficiency below $\lambda = 400$ nm is usually poor, and combined with the leak in the red/vis dichroic, this means that the focus system will mainly use wavelengths between 420 and 460 nm.

The displayed spectral responses for the red and visual channels can of course be changed if filters are added to the system. This could, for instance, include filters for standard photometric systems in order to obtain a colour output that is more comparable to other studies.

3.2.4   Focus system

For the EMCCD cameras to reach their full potential it is important that the telescope is in the correct focus at all times. The TCI therefore has a focus system that uses the light reflected by the vis/blue dichroic. The light is collimated and sent through a four-quadrant wedge 'focus pyramid'. When the light from the focus pyramid is focussed onto the focus camera by the camera lens, each quadrant will be slightly displaced, and the distance between the spots depends linearly on the focus offset. By using a script that can analyse the focus data and calculate the current focus offset, it is possible to do an automatic focus correction of the telescope.

A Prosilica GC1350 CCD camera from Allied Vision Technologies, using the Sony ICX205 CCD chip, was initially chosen as a focus camera. However, as only a small wavelength range ($\sim 420 - 460$ nm) is available for the focus system, and since the Prosilica camera has no cooling system and a rather high readout noise level, it was not possible to detect a reasonable signal even for relatively bright stars.

After analysing the problem, it was found that the Atik 314L+ camera solves the problem. This camera uses the Sony ICX285 CCD chip, and has a cooling system and a lower readout noise level of around $5\,e^-$. Calculations show that with this CCD camera using 2x2 pixel binning, an integration time of $10\,\text{s}$, and a seeing of $0.''5$, it should be possible to focus the telescope if there is a star brighter than about $m_B = 17\,\text{mag}$ in the field. Based on Allen (1973), we find that with this limit, the sky coverage is over 70% on average and over 95% near the Galactic plane. At a seeing of $1''$ the magnitude limit is $m_B \simeq 16.5\,\text{mag}$, and the sky coverage thus drops to 60% on average and 90% near the Galactic plane. It should be noted that the data from Allen (1973) used for these calculations is criticised in Bahcall et al. (1980) for up to a 40% too high density.

3.2.5 Technical Implementation

A technical drawing of the instrument is shown in Fig. 3.3. This figure also shows the positions of the filter wheels inside the instrument housing.

Andor has developed a special PCI controller card to control the EMCCD cameras. Each camera thus needs to be connected with the PCI controller-card using a two metre long signal cable.

On the SONG telescope, the Andor PCI cards are installed in two lightweight computers attached directly on the telescope mount, which transfer the data from the cameras to a server using a gigabit ethernet connection.

On the DK154 we have chosen to use the Adnaco[3] S1A PCI/PCIe fiber-optics extension system. The Adnaco system consists of

(a) a small motherboard, with two PCIe and two PCI slots, in one of which the Andor controller-card is attached,

(b) a PCIe card, that is installed in a computer in the control room, and

(c) a 50 metre fibre cable connecting (a) and (b).

The control room computers are now able to use the PCI/PCIe slots on (a), and thus the Andor controller card, as if they were installed directly in the computer. Using this system ensures a fast and very stable connection to the EMCCD camera and physical access to the computer running the camera even when the telescope is being operated. It also eliminates any mechanical wear that would otherwise have been caused on hard disks (HDDs) and other moving parts attached to a moving telescope. The focus camera is attached to a USB PCIe card that is connected to a PCIe slot on (a). This makes it possible to run the focusing routine described in Sect. 3.2.4 on the control room computer. See also the schematic in Fig. 3.5.

---

[3]http://www.adnaco.com
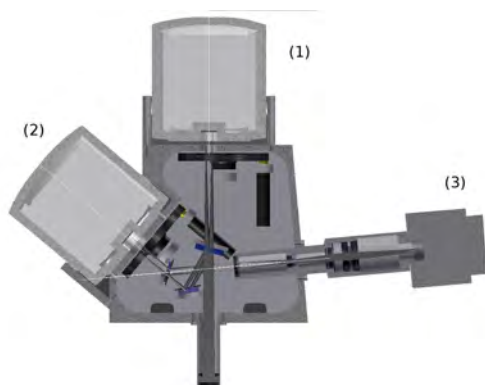
Figure 3.3: Technical drawing of the TCI at the DK154. Attached to the instrument housing are (1) the red, and (2) the visual EMCCD cameras, and (3) the focus camera. Filter wheels are included in the drawing, although these are currently not installed.
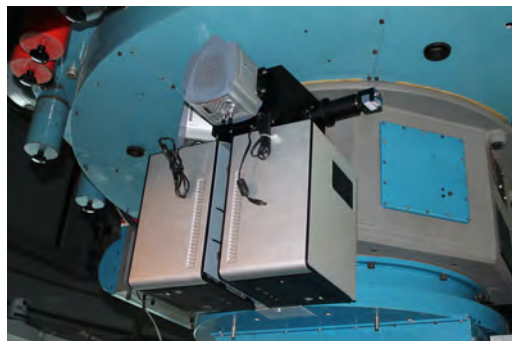
Figure 3.4: Picture of the TCI installed on DK154. Beneath the instrument housing and the cameras are the two cabinets that contain the Adnaco fiber-link motherboards, and the Andor PCI cards.

Fig. 3.4 is a picture of the TCI installed on DK154. Here the two cabinets containing the two Adnaco and Andor cards, one for each EMCCD camera, can be seen attached to the telescope beneath the instrument housing and cameras.

Each of the cameras are run by a HP Compaq Elite 8300 PC, employing a quad-core processor and 24 GB RAM. The computers are running the Ubuntu 12.04 LTS distribution of Linux. The computers are responsible for acquiring, saving, and processing the high frame-rate data. At a 10 Hz frame-rate, this is about 300 MB/min, and thus up to 200 GB/night/camera. Besides a 500 GB HDD for the control system and other software, the computers are therefore equipped with both a 1 TB and a 4 TB HDD.

The TCI was installed at the DK154 in the spring of 2013. There were some hardware problems delaying the operations of the visual camera. These problems were fixed in the summer of 2014, and both EMCCD cameras are now working.

3.3 Software

A new software system, called *Odin*[4], has been developed for the TCI.

The Odin system makes use of a server-client structure in order to run the two cameras simultaneously, and to enable it to run on different hardware set-ups. The

---

[4]*Odin* is the Alfather of the gods from the Norse mythology. He is one-eyed and uses his two ravens, Huginn and Muninn ("Thought" and "Memory"), to keep an eye on the world.

system has built-in communication with the TCS, enabling it to do automated observations, focus adjustment etc. It has an automatic pointing correction routine, that ensures a pointing precision of better than $0\!.\!''5$ for previously observed targets. The latter is especially important given the relatively small FoV of $45'' \times 45''$.

The software system for an instrument like the TCI will always evolve, as more and/or different functionality is required. The Odin system has evolved a lot, and will most likely evolve in the future. However, using some version of this software has made it possible to carry out regular EMCCD observations at the DK154 for several years.

3.3.1 Overview

The Odin system consists of a number of modules that are running as daemon (or background) processes:

- The **camera servers** handle the communication with the cameras and save the raw data.

- The **Odin server** handles the communication with the camera servers and the TCS.

- The **EM reduction software** calibrates the raw data, and saves it as FITS files.

- An **SQL database** is used for storing, and sharing information about the telescope and camera status between different parts of the system.

- The **autofocus script** is described in Sect. 3.2.4.

For the DK154 a graphical user interface (GUI), called the Odin client, has been implemented for controlling the Odin server. The Odin client can be used either locally at the telescope, or from a remote location, depending on the physical location of the observer. For the SONG telescope, which is fully robotic and therefore does not have an observer present, a virtual observer module will control the Odin server.

An overview of the TCI and the Odin software are given in Fig. 3.5 and the different parts of the system will be described in more detail below.

We have chosen to implement the system in Python, due to its widespread use in astronomy, rapid development capability, and large number of existing modules. To communicate between the servers we use the `Pyro` (PYthon Remote Objects) module, as this is completely written in Python, stable, and easier to use than, for instance, XML-RPC. Due to the complexity of the system and that many tasks need to be performed in parallel, the `multiprocessing` and `threading` modules
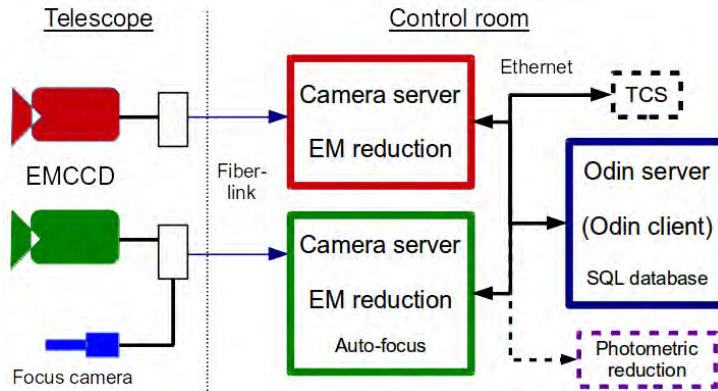
Figure 3.5: Overview of the TCI and the Odin system at DK154. The EMCCD cameras, and the focus camera, are attached to two cabinets, which each are connected to a computer, running the camera server and EM reduction software. The camera servers are controlled by the Odin server running on a third computer. The Odin server also handles the communication with the TCS. The Odin server can be controlled by the Odin client, which can be operated either locally at the telescope or remotely. After the data is reduced by the EM reduction software, it is ready for a photometric reduction.

have been used to create parallel processes and threads, and the `Queue` module is used to interact between them.

An elaborate error handling system has been implemented, such that all errors will be caught and dealt with, either by the system itself or via a message to the observer through the GUI. This part of the software is crucial as the system, in case of an error, would otherwise be left in a state that would require a complete reboot.

To make the system as versatile as possible we have made an effort to gather the telescope and/or site specific parameters in a single configuration file, and have arranged the TCS communication functions in a single module. This means that only very few files need to be telescope specific, making the Odin software easier to implement and maintain at multiple telescopes.

3.3.2   Camera servers

The main purposes of the camera servers are to control the relevant camera and to save the data that it produces. Andor delivers a Linux driver for their cameras in the form of a shared library, which can be controlled from Python using the `pyandor` project[5]. This means that the Andor cameras can be controlled directly

---

[5]http://code.google.com/p/pyandor/

from Python and the data from the cameras can be read directly into `NumPy` arrays.

The camera servers contain all the functions that are needed to change the settings of the camera, such as gain, temperature, etc., and these changes are reported to the SQL database. Whenever an acquisition is started (and ended), the SQL database is updated with information about the type of acquisition, the starting time, etc., so that this information is available to the GUI. The server also has an internal lock, ensuring that an acquisition cannot be started while another is running.

3.3.2.1 Calibration data

The camera server also includes routines for obtaining calibration data, i.e. bias and flat-field correction frames for the EM readout register.

A master bias frame $B(i, j)$ is created by reading out $k = 1000$ frames using the chosen gain. In order to remove the contribution from spurious charges, the 5% highest values for each (i, j) pixel over all k frames are rejected. For the remaining pixel values the mean value over each (i, j) pixel is calculated. This corresponds to the 5% truncated mean from above.

The flat-field frame $F(i, j)$ is meant to correct for gradients caused by variations in the pixel-to-pixel sensitivity of the EMCCD and attenuations in the optical path. The flat-field frames are therefore done with a gain value of $\gamma = 1 \, e^-/$photon. This means that a special master bias frame with $\gamma = 1 \, e^-/$photon is needed for the flat-field frames, and a routine for this has been made.

Both a dome flat-field and a sky flat-field routine are available for the user. For the dome flat routine, the telescope should be pointed towards a uniformly illuminated screen attached to the dome and $k = 20$ exposures are made. The sky-flat routine needs to be run in either evening or morning twilight, with the telescope pointed at a part of the sky with as few stars as possible. A start exposure time is set and when the exposure is done, the mean value of the frame is used to determine the next exposure time. The sequence automatically stops when the exposure time gets too long (or too short), but it can also be stopped by the observer at any time. To avoid systematic errors from stars in the field, the telescope is moved slightly (dithered) between each exposure, and the observer is also able to reject any bad frames when the sequence has ended.

When the k exposures have been made, each frame is bias subtracted and the mean value for each (i, j) pixel over all k frames is found. The resulting frame is normalised and used as the master flat-field frame F.

When using the conventional imaging mode, another readout amplifier is used, and another set of calibration data are therefore needed.

3.3.2.2 Data acquisition

There are three ways of acquiring data. The simplest one is the `snapshot` function, which makes a single integration of the chip, and then reads it out using the EM readout register with the chosen EM gain. The image is then saved directly as a FITS file, without doing any calibration.

To do high frame-rate imaging, one has to use the `Spool` function. This function acquires the requested number of exposures using the chosen exposure time and EM gain. Using the `PyTables` project (Alted et al., 2002-2014), all of the exposures are saved into a HDF5 format file, along with the necessary calibration frames and header information (A description of the HDF5 files and their content is given in Sect. 3.4.1). The exposures are acquired from the camera in blocks of 100 exposures, and each block of exposures is then saved to the HDF5 file while the next block is acquired. This is done to avoid having to store many GBs of data in the virtual memory of the computer until the acquisition is done, which might lead to an unstable system. The start of each block gets a timestamp, which is also saved in the HDF5 file together with the necessary metadata for the observation. While data is being saved in the HDF5 file, a `.tmp` suffix is appended to the file name. When the the observation is done and the last exposures are saved, the suffix is removed.

Parallel with the acquisition a drift correction routine is running. The first block of exposures is stacked into a single frame which is stored as a reference. Each subsequent block is also stacked and the pixel shift between this frame and the reference frame is found using cross-correlation. If the shift is above five pixels, a message is sent to the Odin server, which can then correct the offset. To avoid destroying an observation due to an error in the cross-correlation, an upper correction limit of 10 pixels is set.

A function, `Conventional`, to do conventional imaging has also been implemented. This uses the conventional readout register that has much lower readout noise than the EM register (see Sect. 3.2.2), and produces a single FITS file.

3.3.2.3 Pointing correction

Due to the relatively small FoV, $45'' \times 45''$ (see also Sect. 3.2.2), it is important that a target can be revisited with a high pointing accuracy. The DK154 has a pointing accuracy of about $8''$ rms, which corresponds to about 20% of the width of the frame.

For that purpose, a pointing correction routine has been implemented. The first time a target is visited, the pointing is adjusted manually (or just used as it is) and a 10 s observation of the target is made. This observation is reduced and saved as a FITS file, and is used as a pointing reference. The next time the target

is visited, the `PointingCorrection` function will make a new 10 s observation and compare this to the pointing reference, finding the pixel shift between the two. This shift is then returned to the Odin server, so that the offset can be corrected. With this pointing correction routine, we can achieve a pointing accuracy better than $0''.5$. Accuracy below this limit is hard to achieve as the centroid of the stars starts to be dominated by atmospheric disturbances in this regime.

The PSF width (FWHM) of the 10 s observation is also found and reported back to the SQL database. This can then be used as a measure for the current seeing.

3.3.3 Odin server

The Odin server is the top-level module for the Odin system, and links the (virtual) observer, the camera servers, and the TCS.

When the Odin server is running, it can be connected to one or both cameras, and one can choose to use one or both cameras. All the functionality described in Sect. 3.3.2 is now available. The functions are, however, wrapped in code that makes it possible to operate the two cameras simultaneously, and to report any messages back to the observer.

All communication with the TCS is gathered in a single module, such that this can be easily customised for different telescopes. The TCS module provides the necessary functions to move the telescope, adjust the pointing, and change the focus position. It also has functions to get the status of all of the parts of the telescope that are needed to do successful observations.

Before an observation is started, the camera is checked to make sure it is available for observation (i.e. that it is idle, cooled to the specified temperature, etc.). Also a check of the telescope is made, to make sure that observations are possible. If the celestial coordinates of the target are given, the telescope will be moved to that position, and if a pointing file for the target exists, the pointing will be corrected. The observation can now be started, using one or both cameras, depending on which camera is connected and chosen. If any problem arises before, during, or after an observation, a message and/or question will be relayed to the observer.

Provided a list of targets with celestial coordinates and length of the observations (i.e. exposure time $\times$ number of exposures), the Odin server can automatically observe each target on the list, without the need for observer interaction.

3.3.3.1 Focus routine

In addition to the focus system detailed in Sect. 3.2.4, a routine for focusing the telescope using the EMCCD cameras has been implemented. This works by acquiring a number of 10 s observations at different focus positions and measuring
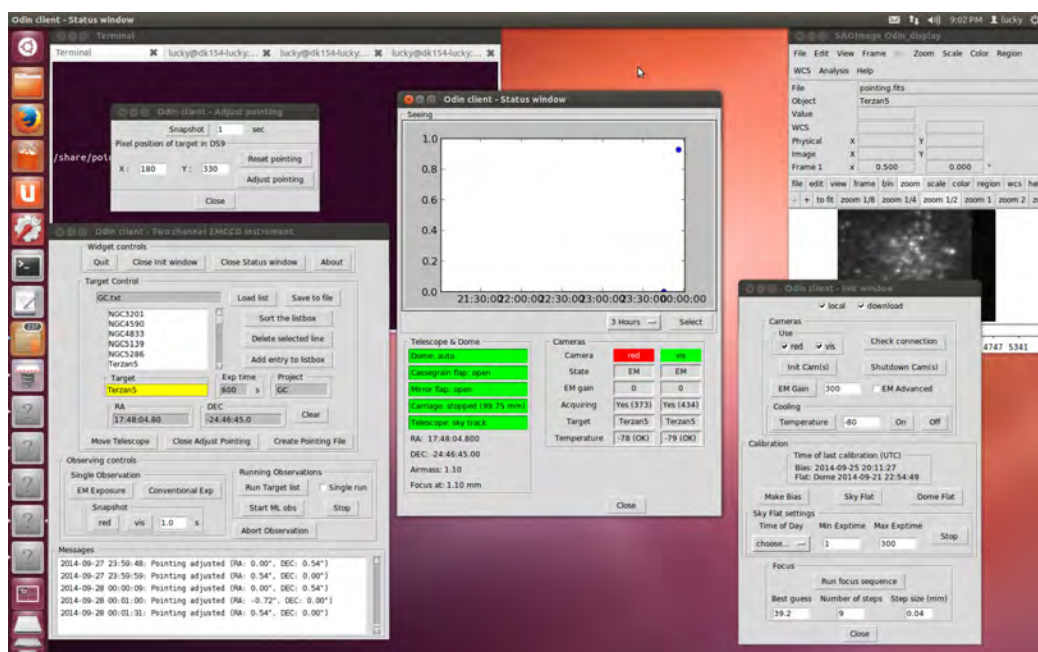
Figure 3.6: Screenshot of the windows for the Odin client. The main *Odin client* window is shown in the lower left corner. Next to this is the *Status* window, and then the *Init* window below a *SAOimage DS9* window. Above the main window is the *Adjust pointing* window.

the PSF width of these. A quadratic fit of the PSF width versus focus position is made, and the minumum PSF width provides the best focus setting.

It should be noted that the PSF width measurement does not work if the telescope is so much out of focus that donut-shaped PSFs are created. The observer therefore needs to provide an initial estimate of the focus, the focus position step size, and the number of steps.

After the focus sequence is done, the observer will be able to examine the fit and each focus observation.

3.3.4 Odin client

The Odin client is a GUI for controlling the Odin server. A screenshot of the Odin client and its windows is shown in Fig. 3.6.

When starting the Odin client, the main *Odin client* window and an instance of the *SAOimage DS9* FITS file viewer[6] are opened.

The main window contains a list box for selecting and providing the information

---

[6]http://ds9.si.edu/

needed to make an observation. For each entry in the list box, one can give a name, celestial coordinates, the length (in seconds) of the observation, and a project name. This information can also be read in as a text file. The different types of observations can be started, including *Running Observations* that will observe all targets in the list box. At the bottom there is a message window that displays messages from the Odin and camera servers.

The *DS9* window will automatically display the created bias, focus, reference, snapshot images, etc., when these are made.

In the *Init* window different settings for the camera can be controlled, and calibration data and focus sequences can be obtained.

The *Status* window displays the PSF width measurements obtained by the pointing correction routine over some selectable time interval. It also shows the current status and different values for the telescope and cameras.

To adjust the pointing of the telescope, an (x, y) pixel position from the *DS9* window can be put into the *Adjust pointing* window. The required pointing offset to move the (x, y) pixel position to the middle of the frame will be applied.

The communication between the Odin client and server has been made lightweight, making it possible to run the Odin client at a remote location. It is, however, also possible to use VNC (Virtual Network Computing) to remotely control the Odin client.

3.3.5 EM reduction

After the HDF5 files have been finalised, they are automatically picked up by the EM reduction software, where each exposure is bias, flat and tip-tilt corrected, and the instantaneous image quality is found, using the algorithm described by Harpsøe et al., 2012b.

As the bias level is subject to variations between the single exposures, the bias correction of an exposure is a two step process. First the bias frame B is subtracted from the exposure. This will correct the overall bias pattern in the frame. Then the offset between the overscan region of the exposure and the overscan region of B is found and subtracted from the exposure. This offset represents the exposure-to-exposure variation in the bias level.

A flat-field correction is done as in conventional imaging, i.e. by dividing each exposure with the flat-field frame F.

The tip-tilt correction and image quality are found using the cross correlation theorem. Given a set of k exposures, a comparison image $C(i, j)$ is constructed by taking the average of 100 randomly chosen exposures. The cross correlation $P_k(i, j)$ between C and a bias- and flat-corrected exposure $I_k(i, j)$ can be found

using

$$P_k(i, j) = \left| FFT^{-1} \left[FFT(C) \cdot \overline{FFT(I_k)} \right] \right| \tag{3.1}$$

where FFT is the fast Fourier transform. The appropriate shift, that will correct the tip-tilt error, can now be found by locating the (i, j) position of the global maximum in P_k.

A measure for the image quality q_k is found by scaling the maximum value of P_k with the sum of its surrounding pixels within a radius r

$$q_k = \frac{P_k(i_{\max}, j_{\max})}{\sum_{\substack{|(i-i_{\max}, j-j_{\max})|<r \\ (i,j)\neq(i_{\max}, j_{\max})}} P_k(i, j)} \ . \tag{3.2}$$

Using this factor, instead of just the maximum value of the pixel values in the frame (Smith et al., 2009), helps to mitigate the effects of fluctuations in atmospheric extinction and scintillation that can happen over longer time scales.

To improve the tip-tilt correction and image quality, a new comparison image C is made based on the 100 exposures with the highest q values. The final shifts and q values are then found, using the algorithms described above, based on this new comparison image. This is done to avoid the effects of sub-quality exposures among the randomly chosen exposures for the first comparison image.

The FFT transformation is done using the `FFTW3` library (Frigo et al., 2005), linked to Python via the `PyFFTW` project. This has proven to be about 20 times faster than the FFT implementation from `NumPy`.

Cosmic rays from the exposures are detected and corrected using a routine based on algorithms from Harpsøe et al. (2012a). As the noise in EMCCD data are exponentially distributed, and not normally distributed as in conventional CCD data, a sigma clipping method cannot be used. Instead the rate of photons is estimated for each (i, j) pixel in the frame over all k exposures. Using this photon rate at each pixel position, the probability p for the observed pixel values in each exposure can be calculated. If a pixel value is too improbable, a new value is generated from a random number generator based on p and the Erlang PDF.

The reduced exposures are not saved in the HDF5 file, but the necessary information (bias offset, quality factor, pixel shift, and cosmic ray information) is saved for each exposure as described in Sect. 3.4.1. Using this information the exposures can easily be reduced, combined, and saved in whatever way is required. The default output is the ten-layer FITS cube described in Sect. 3.4.2.

3.4 High frame-rate data formats

As described in Sect. 3.3, the Odin software will provide two outputs for each high frame-rate observation; a HDF5 spool file, and a FITS cube. A description

of the two file formats and their contents is given below.

The file naming convention for the two formats are *TARGET_TIC_YYMMDD_NNNNN.EXT*, where

TARGET is the name of the observed target,

T is a one letter telescope identifier (L for the DK154),

I is the instrument identifier (`l` for the EMCCD camera in EM mode, and `c` for conventional mode),

C is the channel (`r` for red, and `v` for visual),

YYMMDD contains the numerical values for year, month, and day, respectively, in UT,

NNNNN is a five digit running number, and

EXT is the file extension (`.h5` for HDF5 files, and `.fits` for FITS files).

An example of a file name could therefore be `NGC6441_Llv_140603_00011.fits`, for an observation of NGC 6441, made with the visual EMCCD camera at the DK154 as the 11th observation on June 3rd, 2014. With this naming convention, it is certain that all file names are unique. Observations made simultaneously with the two EMCCD cameras will have the same running number, but will keep their uniqueness due to the channel identifier. The *TARGET* identifier is therefore not necessary for file name uniqueness, but has been included for convenience.

3.4.1   HDF5 spools

The Hierarchical Data Format version 5 (The HDF Group, 1997-2014), or just HDF5, is used to store the raw data from the EMCCD cameras. The HDF5 files, often referred to as spools, are sorted in a tree structure with a root, that can hold branches and leaves. Leaves can be attached to branches, and information is stored on a leaf as either a value, a tuple, or an array.

When an observation is done the HDF5 file will contain

a `bias` leaf, with the most recent bias frame,

a `flat` leaf, with the most recent normalised flat-field frame,

an `imageData` branch, containing a leaf for each exposure, such that the single exposures are accessible without having to read a large cube with all exposures into the memory. On the branch there are also stored metadata about the observation. These metadata include information about the telescope, date and time of the observation, exposure time, EM gain, WCS data, etc.

A `timingData` leaf containing an array with the time stamps for each block of 100 exposures.

With this information it is possible for the EM reduction software to process the exposures. After this process is done, two extra branches are added to the HDF5 file;

a `reducedData` branch, containing a leaf for each exposure. Each leaf contains a tuple with the bias offset, the quality factor, and the pixel shift for the exposure.

A `cosmicData` branch, which contains a leaf for each pixel contaminated by a cosmic ray. Each leaf thus contains a tuple with the exposure number, the pixel position, and a new value for that pixel position.

Using these data, and the bias and flat-field frames, the exposures can easily be reduced, combined, and saved as FITS-files.

3.4.2   FITS cubes

When the EM reduction software has processed the exposures, it will produce a ten-layer FITS cube. Each layer in this cube represents the sum of some percentage of the shifted-and-added exposures after the exposures have been organised into ascending order by image quality. To preserve as much spatial information as possible, the layers have the following percentage cuts: (1, 2, 5, 10, 20, 50, 90, 98, 99, 100). The layers are non-cumulative, however, which means that any exposure is only included in one layer, and the percentage of exposures in the layers are thus: (1, 1, 3, 5, 10, 30, 40, 8, 1, 1). This means that the first layer contains the sum of the best 1% of the exposures in terms of image quality, the second layer the second best 1%, the third the next 3%, and so on.
If the required shift exceeds 20 pixels for a given exposure, the exposure is rejected. This is done to ensure that, except for a 20 pixel border, each pixel in a layer has a uniform number of input exposures. The total number of exposures used to create the ten-layer image cube might therefore be lower than expected. The layers are saved as a single cube in the FITS file, and not as individual extensions.

The metadata from the HDF5 file are saved in the FITS file header along with information about the number of exposures, and FWHM for the single layers and for an image made by stacking all the layers.

3.5 System performance

This section contains a brief analysis of the improvement in spatial resolution compared to conventional imaging that is achieved with the TCI, and how updated photometric methods for high frame-rate imaging can improve the photometric precision.

To be able to perform the tip-tilt correction and quality estimates of the individual exposures as described in Sect. 3.3.5, it is necessary to have a signal of a certain strength. The standard setting for the EM system at the DK154, is therefore to use an EM gain of $\gamma = 300 \, e^-$/photon and a $10 \, \text{Hz}$ frame-rate. Simulations of stellar populations based on the Besançon model (Robin et al., 2003), show that with these settings there will be stars bright enough in, for instance, all pointings towards Baades window to estimate the exposure quality. Using a higher frame-rate would decrease the signal in the individual exposures, and thus limit the possible pointings.

3.5.1 Spatial resolution

To get an idea of how the EM system performs in terms of improving the spatial resolution compared to conventional imaging, we have performed a test similar to the one made in Smith et al., 2009, which is described in Sect. 2. However, instead of looking at Strehl ratios, the improvement in PSF width has been examined. For over 80% of the red-band observations from the 2014 season, the FWHM of different percentage selections have been found. To mimic an observation made with a conventional CCD, all the exposures in each observation have been stacked without doing any shifts, and from this we find a 'conventional' FWHM. In the left column of Fig. 3.7 the 1, 5, 50, and 100 percentage FWHM are plotted against the conventional FWHM.

We find that $\sim 25\%$ of the FWHMs in the 1% selection are below $0\rlap{.}''5$, while about 8% are below $0\rlap{.}''4$. For the 100% selection, these numbers are 4% and 0.1%, respectively, while for the conventional FWHM they are 0.1% and 0.01%, respectively. At spatial resolutions below $0\rlap{.}''5$, we start to see effects from the telescope optics at the DK154. As the telescope is not designed for such high-resolution instruments, a triangular coma originating from the mirror support dominates the PSF more and more as the PSF width decreases. This effectively puts a limit on the spatial resolution that is higher than the diffraction limit of $\sim 0\rlap{.}''13$ at $800 \, \text{nm}$.
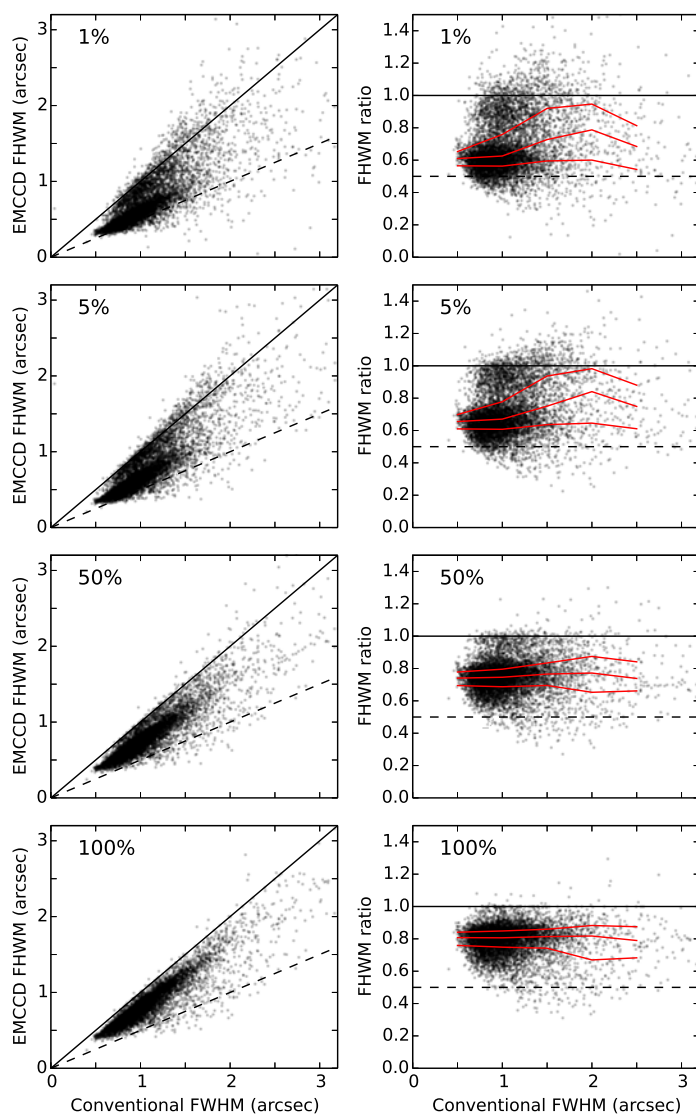
Figure 3.7: Left column: For each observation, the FWHM of the 1%, 5%, 50%, and 100% of the best frames in an observation is compared to the FWHM of the corresponding 'conventional' observation (see text for details). The solid line is unity, i.e. no improvement, while the dashed line shows the half of the conventional FWHM. Right column: Similar to the left column, but showing the ratio between the shift-and-added and 'conventional' FWHM. The red lines give the median (50%) and the inter-quartile points (25%, 75%) of each half-arc second bin. The plots are based on FWHM measurements of 7648 observations from the 2014 season at the DK154.

Table 3.1: Robust mean and rms values of the FWHM ratios.

%	1	5	10	50	90	100
μ	0.64	0.69	0.71	0.75	0.79	0.81
rms	0.17	0.16	0.16	0.1	0.09	0.08

Notes. Robust mean (μ) and rms values (Beers et al., 1990) of the FWHM ratios between different selection percentages and a 'conventional' observation.

To see if a good FWHM for the 1% selection image also means a good FWHM for the other selections, and vice versa, the correlation coefficient $\rho_{X,Y}$ between the different selections was found. Between the 1% and 5% selection FWHMs a value of $\rho_{1\%,5\%} = 0.94$ was found and this number decreases for larger selections ending in $\rho_{1\%,100\%} = 0.85$. The same pattern is seen for the other percentages, though with the lowest ρ being $\rho_{5\%,100\%} = 0.91$ and the highest $\rho_{90\%,100\%} = 0.996$. Thus there seems to be a fairly good correlation between the FWHMs of the different selections, with the 1% selection as a slight outlier.

The right column of Fig. 3.7 shows the improvement in PSF width, as the ratio of the shifted-and-added FWHM to the conventional FWHM. On top of this the median (50%) and the inter-quartile points (25%, 75%) of each half-arcsecond bin is plotted.

For the 1% selection, $\sim 10\%$ of the observations have a FWHM ratio better than 0.5, and the majority are below 0.7, but $\sim 25\%$ of the observations are worse than 0.8. Most of these are between 0.8 and 1, but $\sim 6\%$ are above 1. This pattern repeats itself for the 5% selection.

One reason for this could be that when a short observation is made, only very few exposures go into the 1% (and 5%) image. This means that the S/N is very low and this might make it hard to determine the FWHM in a robust way. A proof of this would be if there were a correlation between the observation length and the FWHM ratio, but this is not found to be the case. Another reason could be that these bad observations were made at high airmass, but only a very weak correlation of $\rho \simeq 0.4$ has been found between airmass and FWHM ratio, and this value is the same for all selections. Another explanation could be that the 10 Hz frame-rate used for these observations is not high enough in some weather conditions, for instance during high winds. A more thorough analysis of the affected observations and reduction algorithms is needed to sort out this issue, but this is not within the scope of this article.

For the 50% and 100% selections the scatter in FWHM ratio is reduced. Fig. 3.7 shows that the FWHM is improved for almost all observations at the higher percentage selections when doing shift-and-add. Table 3.1 shows the robust mean μ and rms values (based on median absolute deviation, cf. Beers et al., 1990) for

the FWHM ratios at different selection percentages. This indicates that the average improvement of doing shift-and-add versus conventional imaging, is about a fifth of the PSF width on average for the 100% selection, and ~ 35% for the 1% selection. It also shows that virtually no improvement in FWHM is achieved by omitting the worst 10% of the exposures.

It should be noted that shifted-and-added EMCCD data generally have a PSF shape that is more like a core-halo structure than a Gaussian profile. A FWHM measurement of this kind of profile therefore has an intrinsic uncertainty. We have, however, chosen to use this measure, as we believe it provides the best basis for comparison with other systems.

3.5.2   Photometric stability

The photometric performance of the TCI was investigated in the high-precision domain by monitoring one transit of the planetary system OGLE-TR-56 (Konacki et al., 2003). This object consists of a gas giant (mass $1.4\,M_{Jup}$, radius $1.7\,R_{Jup}$) transiting an F-type star (mass $1.3\,M_{\odot}$, radius $1.7\,R_{\odot}$) every 1.21 days (Southworth, 2012). The comparatively large component radii and short orbital period make OGLE-TR-56 a good candidate for the detection of tidally-induced orbital decay (Birkby et al., 2014). This is potentially detectable by measuring the progressively earlier occurrence of transits compared to a linear ephemeris, by an amount which is predicted to be roughly 30 s over a decade (Birkby et al., 2014). On the night of 2014/05/08 we monitored OGLE-TR-56 (magnitudes $V = 16.6$ and $I = 15.30$) for 4.5 h centred on the predicted midpoint of a transit of duration 2.2 h. We used the red camera and specified 1000 exposures at a 10 Hz frame-rate with a gain of $300\,e^-$/photon. The seeing was ~ 0.5 ″ as measured from the best 1% of images, but the sky conditions were not photometric.

Data reduction was performed on the fits cubes (see Section 6.2) after stacking multiple layers together to obtain images containing the best 90% of the original observations, corresponding to a combined exposure time of 90 s. Tests with different numbers of layers showed that the best photometry was obtained using a high fraction of the original images, as expected for this relatively faint star. Differential photometry versus up to five comparison stars was obtained using the DEFOT pipeline (Southworth et al., 2009b) modified to use the PSF photometry routines available in the NASA ASTROLIB[7] which are an early version of DAOPHOT (Stetson, 1987) ported to the IDL[8] programming language.

---

[7]The ASTROLIB subroutine library is distributed by NASA. For further details see: http://idlastro.gsfc.nasa.gov/.

[8]The acronym IDL stands for Interactive Data Language and is a trademark of ITT Visual Information Solutions. For further details see: http://www.ittvis.com/ProductServices/IDL.aspx.
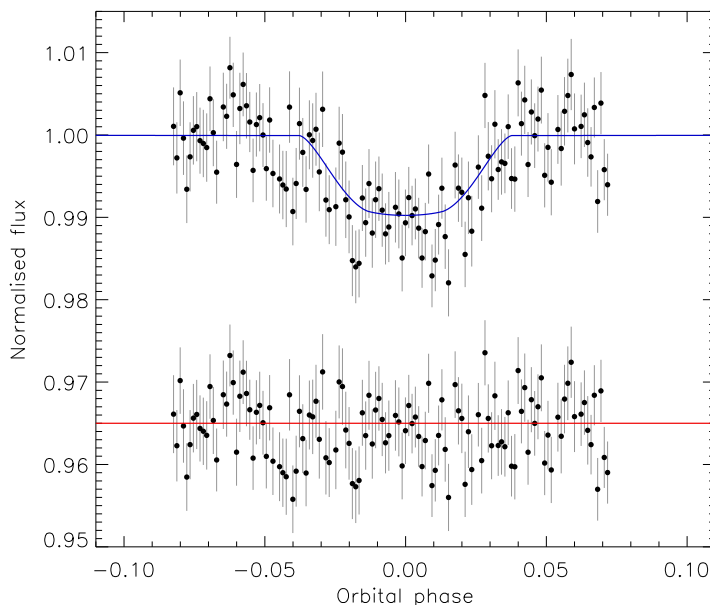
Figure 3.8: Light curve of the transiting planetary system OGLE-TR-56 obtained using the red camera of the TCI. The black points show the light curve(top) and residuals (bottom). The blue line shows the JKTEBOP best fit and the red line the value the residuals have been shifted to.

The resulting light curve has a scatter of 4.4 mmag around the best fit, and shows a clear detection of the transit of depth 10 mmag (see Fig. 3.8). For comparison the photometric precision using a conventional CCD and defocussed photometry has been estimated as 3.4 mmag using the S/N calculator described in Southworth et al. (2009b). The light curve was modelled using the JKTEBOP code (Southworth, 2008) with all parameters fixed at known values (Southworth, 2012) except for the time of transit midpoint. The transit time was measured to a precision of 314 s. We conclude that the TCI on the Danish telescope is capable of high-precision photometry, but that the results achievable for OGLE-TR-56 are too limited by photon noise to be useful for transit timing studies of this system.

3.5.3 Photometric improvement

Due to the improvement in spatial resolution that the EMCCD cameras can provide, these cameras are optimally suited for crowded fields.
To test the photometric stability of the TCI in crowded fields, Harpsøe et al. (2012b) have made a photometric reduction of the very dense central part of the globular cluster ω Cen. The 1.5 hour observation, consisting of 50, 000 single exposures, was stacked into 100 images consisting of 500 consecutive exposures,

using the algorithms described in Sect. 3.3.5. A reference image using the best 1000 exposures was created and this had a FWHM of $\sim 0\!\!.''4$. Using this reference frame the time series photometry was extracted from the 100 images using the standard PSF fitting photometry package DAOPHOTII (Stetson, 1987). The upper panel of Fig. 3.9 shows the RMS magnitude deviation for the 2523 light curves extracted by DAOPHOTII. The light curves have been approximately calibrated to Johnson *R* magnitudes using aperture photometry of 3 reasonably isolated stars, and their corresponding F675W filter magnitudes taken from Hubble Space Telescope WFPC2 camera data. The plot also shows the photon noise and excess noise limits, and the noise limit for a $18.5\,\mathrm{mag}/\square''$ background signal.

To see if the photometric reduction could be improved, the same ω Cen dataset was reduced using the `DanDIA`[9] pipeline (Bramich, 2008; Bramich et al., 2013). `DanDIA` uses difference imaging analysis (DIA), which is particularly apt at extracting precise photometry in crowded regions. Instead of modelling the kernel as a combination of Gaussian basis functions, `DanDIA` uses a flexible discrete-pixel kernel. This has been shown to give improved precision in very crowded regions (Albrow et al., 2009).

To accommodate the advantages of high frame-rate imaging, a few modifications have been made to the pipeline. For each observation, the single exposures can be combined in two ways:

Quality-binned: exposures are binned after they have been organised into acsending order by image quality.

Time-binned: exposures are grouped into time bins, such that the required S/N is achieved.

The quality- and time-binned images can either be constructed directly from the HDF5 spools, as described in Skottfelt et al. (2013b), or they can be made from the FITS cubes. If the latter method is used (see Skottfelt et al., 2014a), the single layers can be saved as quality-binned images, and the whole cube, or some subset hereof, can be stacked into a time-binned image. The pipeline is then able to stack the sharpest of the quality-binned images to make a high-resolution reference image from which reference fluxes and positions are measured. The reference image, convolved with the kernel solution, is subtracted from each of the time-binned images to create difference images, and, in each difference image, the differential flux for each star is measured by scaling the PSF at the position of the star (cf. Bramich et al., 2011). Compared to conventional CCD data, EMCCD data has different noise model (Harpsøe et al., 2012b), and this has also been implemented.

---

[9]`DanDIA` is built from the DanIDL library of IDL routines available at http://www.danidl.co.uk
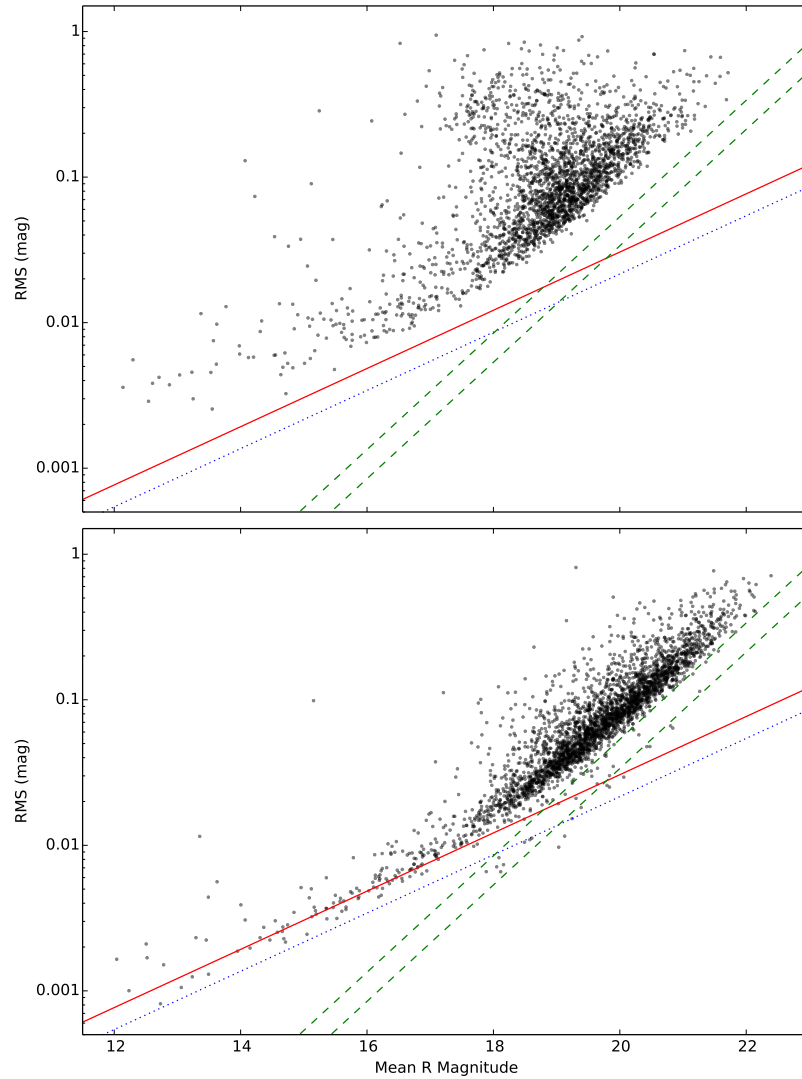
Figure 3.9: Plots of the RMS magnitude deviation versus the mean magnitude for the 2523 and 3010 calibrated *R* light curves, extracted by DaoPhotII (upper panel) and the modified version of `DanDIA` (lower panel), respectively, for the central region of the ω Cen cluster. The photon noise and excess noise limits are shown as a blue dotted, and a red solid line, respectively. The dashed green line shows the noise limit for a $18.5 \, \mathrm{mag}/\square''$ background signal.

The RMS magnitude deviation for the 3010 light curves extracted with `DanDIA` is shown in the lower panel of Fig. 3.9. Johnson R magnitudes have been approximated using the same three stars as in the DAoPHoTII reduction. It is apparent that the DIA reduction is superior to the DAoPHoTII reduction, in that the majority of the photometric scatter falls much closer to the theoretical limits. There is an improvement of the mean rms for all magnitude bins, ranging from a factor of ~ 2 for the brightest magnitudes, to a factor of 7 at 19th mag. For magnitudes fainter than about 19, the photometric precision is limited by the equivalent of a $18.5\,\mathrm{mag}/\square''$ background signal, which most likely originates in the unresolved dense stellar population in the central part of the cluster.

3.5.4 Two-colour capabilities

With a red and visual camera running simultaneously, it is easy to obtain colour information for the observed stars. As the visual camera only came online this summer (2014), no scientific results have yet been published using visual band data from the TCI.

To test the two-colour capabilities of the TCI, six observations of the central parts of the globular cluster NGC 288 ($\alpha = 00^{\mathrm{h}}52^{\mathrm{m}}45.24^{\mathrm{s}}$, $\delta = -26°34'57.4''$ at J2000.0) were obtained on the night of September 21st, 2014. The observations were done in the red and visual band simultaneously, and the data were analysed using the modified version of the `DanDIA` pipeline described above. The instrumental magnitudes found by the pipeline are denoted v and i for the visual and red band, respectively, and are based on reference images combined from 6780 and 6060 exposures, respectively, which corresponds to ~ 10 minutes of observation. A PSF width of $0.''48$ and $0.''46$ FWHM are found for the v and i reference images, respectively.

The NGC 288 cluster is part of *The ACS Survey of Galactic Globular Clusters* (Sarajedini et al., 2007) made with the ACS instrument on the Hubble Space Telescope (HST), and the survey is available online[10]. The data files include celestial coordinates, ACS F606W filter Vega magnitudes (denoted V), and ACS F814W filter Vega magnitudes (denoted I) (Sirianni et al., 2005), Fig. 3.10 shows the visual and red reference images for NGC 288 together with a HST ACS image of the same field.

Using the celestial coordinates we were able to find 430 matching stars, and from these a conversion between the instrumental magnitudes and ACS magnitudes was found. This was done by fitting a linear relation to the difference between the ACS and instrumental magnitudes, and the instrumental $v - i$ colour of each of the stars with $V < 19$. The resulting relations are shown in Fig. 3.11.

---

[10]www.astro.ufl.edu/~ata/public_hstgc/
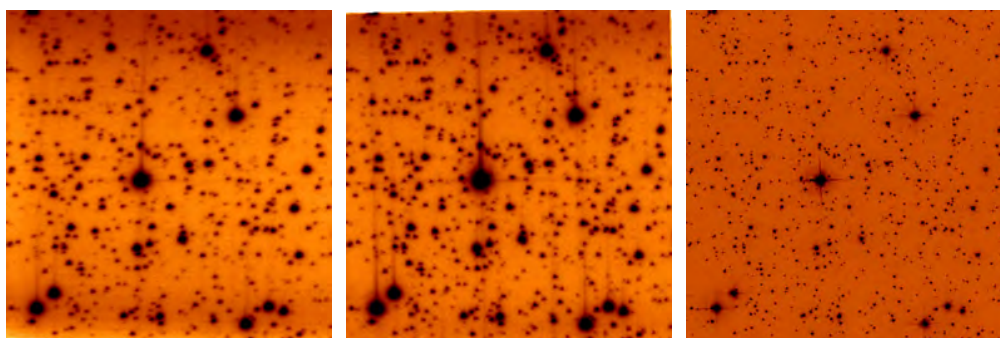
(a) Visual reference image **(b)** Red reference image **(c)** HST ACS image

Figure 3.10: Visual *v* and red *i* reference frames for the NGC 288 cluster and a HST ACS image of the same field as comparison. North is up and East is to the left. The image size is about $45'' \times 45''$.
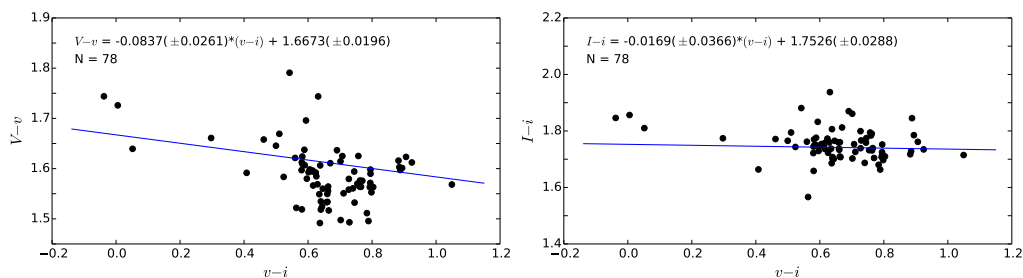
Figure 3.11: Relations used to convert from instrumental to ACS magnitudes for the *V* (top) and *I* (bottom) bands.

Using the calibrated *V* and *I* magnitudes, a colour-magnitude diagram was produced. This is shown in Fig. 3.12 together with the corresponding HST/ACS photometry. Especially for the brighter stars there is a good agreement between the two sets of photometry. For the fainters stars there seems to be the same trend, but with a much higher scatter in the TCI data. Some differences between the two data sets are not surprising considering that there are difference between the HST/ACS and TCI filters and that we are comparing photometry of faint stars from a 1.5m ground telescope with a 2.5m space telescope.

In Mattila et al. (1996) the sky brightness for a moonless night at the La Silla observatory is reported as being $V = 21.75(\pm0.08)\,\mathrm{mag}/\square''$ and $I = 19.48(\pm0.05)\,\mathrm{mag}/\square''$. The background signal will therefore contribute significantly to the noise at the fainter magnitude levels and leads to increased scatter. Signal from background stars will also have an effect on the scatter, but as the central region of NGC 288 is not very dense, the contribution is negligible compared to what was found for ω Cen.
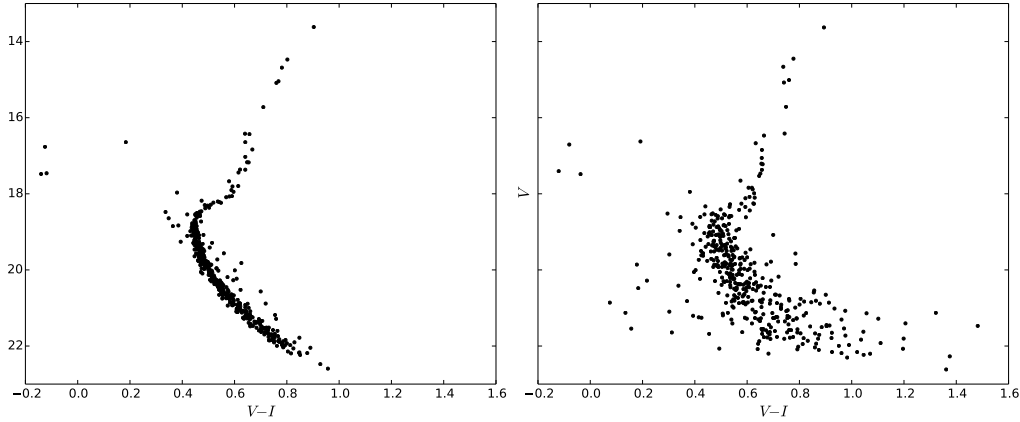
Figure 3.12: $(V - I)$, V Colour-magnitude diagram of 430 stars in the central part of NGC 288. Upper panel are the HST/ACS data, and the lower panel are TCI data calibrated using the HST/ACS data.

3.6   Scientific results

Since 2012 the red EMCCD camera has been used for regular operations at the DK154, initially as the single red camera and during the last two years a full version of the TCI.

The main purpose of the TCI is to follow-up gravitational microlensing events towards the Galactic centre in order to detect exoplanets, i.e. planets orbiting stars other than the Sun. However, a number of other scientific results have also been achieved in this period.

3.6.1   Gravitational microlensing of low-mass exoplanets

During the last 20 years over 2000 exoplanets have been detected using a number of different techniques. The by far most successful techniques, in terms of number of detections, are the radial-velocity technique and observations of transiting planets. These techniques are, however, skewed towards detecting high-mass planets orbiting close to the host star, and this has left us with an incomplete picture of the exoplanet population statistics (Gaudi, 2012)

The only technique currently available for obtaining population statistics of cool low-mass planets is gravitational microlensing. When a background star and a foreground star become near-perfectly aligned with an observer, the foreground star will act as a gravitational lens, magnifying the light from the background star. Such an event lasts about a month, and creates a characteristic bell-shaped light curve for the background star. If a planet is orbiting the lens star, it will perturb the

gravitational lensing effect, and thus create a feature in the light curve, lasting from days to hours, depending on the mass of the planet (Mao et al., 1991). Subsequent analyses and modelling of the light curve can provide information about the lens star and planet, such as masses and distances, etc.

To detect planets of Earth-mass and below, one needs to have a photometric precision of Galactic bulge main sequence stars to within a few percent, and this requires angular resolutions below $\sim 0\rlap{.}''4$ (Bennett et al., 2002). Reaching such high spatial resolution from the ground is difficult with conventional CCD imaging unless an AO system is available, but it can be done with EMCCDs. As discussed in Sect. 3.5.1, the TCI at the DK154 is only just capable of obtaining angular resolutions below $0\rlap{.}''4$, due to imperfections in the optics. With the near diffraction limited optical system on the SONG telescopes, these should be able to achieve spatial resolutions down to $\sim 0\rlap{.}''2$ at 800 nm. Preliminary test observations during the summer of 2014 reached a resolution of $\sim 0\rlap{.}''25$.

Observations made with the TCI at the DK154 are done as part of the MiNDSTEp consortium (Dominik et al., 2010), and this will also be the case for SONG.

3.6.2 Variable stars in the cores of globular clusters

Based on observations made with the red EMCCD camera over two nights in August 2012, Skottfelt et al. (2013b, hereafter S13) were able to find two previously unknown variable stars in the crowded central region of the globular cluster NGC 6981. The variable star population of the cluster had been examined previously, latest in Bramich et al. (2011, hereafter B11), where 11 new RR Lyrae (RRL) stars and 3 new SX Phoenicis stars were found. The two new variable stars, denoted V57 and V58, are located close to a bright star (see Fig. 4.1). In B11, which used conventional CCD imaging, the bright star was saturated and the two variable stars were therefore in a region that could not be measured due to the saturated pixels. The S13 data was analysed using the modified version of DanDIA described in Sect. 3.5.3, and from the light curves retrieved, V57 was found to be an RRL star, while it was not possible to classify V58.

Shortly after the publication of S13, another analysis of the variable star population in NGC 6981 was published by Amigo et al. (2013). This analysis was based on archive data from, among other, the FORS1 instrument made at one of the 8.0m VLT telescopes. Here the authors were also able find V57, and two other RRL stars outside the FoV of B11, but they were not able to detect V58.

The results from S13 lead to the start of a survey of variability in Galactic globular clusters using the TCI (Kains et al., 2014). The survey has so far been running at the DK154 during the 2013 and 2014 MiNDSTEp observing campaigns, with bi-weekly observations of about 30 globular clusters. The first results from the survey have recently been published in Skottfelt et al. (2014a, hereafter S14).

In S14 the analysis of time series observations from 2013 and 2014 of five metal-rich ([Fe/H] > -1) clusters is presented. In the analysis 48, 49, 7, 8, and 2 previously unknown variables are found in NGC 6388, NGC 6441, NGC 6528, NGC 6638, and NGC 6652, respectively. Due to the relatively small FoV of $45'' \times 45''$ of the TCI, only the dense central part of the clusters is observed.

Especially interesting is the case of NGC 6441, for which the variable star population of about 150 stars has been thoroughly examined by previous studies, including a HST study. Of the 49 new variable stars presented in the S14 article, one (possibly two) are RRL stars, two are W Virginis stars, and the rest are long period semi-regular/irregular variables on the red giant branch. Furthermore the first double mode RR Lyrae was detected in the cluster.

The S13 and S14 articles thus demonstrate the power of EMCCDs combined with DIA for high-precision time-series photometry in crowded fields, and the feasibility of large-scale observing campaigns using these methods.

3.6.3 The rings of Chariklo

On June 3rd, 2013, the Centaur (10199) Chariklo occulted a background star. Chariklo is an asteroid-like object of about 125 km in radius, orbiting between Saturn and Uranus with a semi-major axis of 15.8 AU.

As reported by Braga-Ribas et al. (2014) the stellar occultation by Chariklo was observed from eight sites in South America. The occultation by Chariklo itself was only recorded at three sites in Chile, but seven sites detected an indication of a secondary event in the form of rapid stellar flux interruptions. However, it was only from the DK154 data that the ring structure could be clearly identified. With a 10 Hz frame-rate, the TCI was able to resolve these secondary events into two sub-events, lasting only ~ 0.1 and ~ 0.3 seconds, with a 0.2 second gap.

The best interpretation of the observations is that Chariklo has two rings. With the high precision data from the TCI, the width of the two rings was determined to be ~ 7 and ~ 3 km wide, with a few hundred metres precision, and located at orbital radii of ~ 391 and ~ 405 km, respectively.

The presence of rings, partly composed of water ice, around Chariklo explains a dimming observed in the Chariklo system between 1997 and 2008 and the gradual disappearance of ice and other absorption features in its spectrum over that period.

Previous stellar occultations by main-belt asteroids have not revealed any rings, so it is not known if rings around minor bodies are generic or exceptional features. However, the fact remains that Chariklo is, so far, the smallest solar system object known to have rings.

3.6.4 Locating faint stars near transiting planetary systems

Using defocused observations of transiting planets, it has been possible to reach photometric precisions down to a few tenths of a millimagnitude with the DFOSC instrument at the DK154 (e.g. Southworth et al., 2009b; Southworth et al., 2010). There is however a risk that faint nearby stars can contaminate the signal from the target stars. Such objects would dilute the transit and cause the radius of the planet to be underestimated, or, if the contaminant is an eclipsing binary, render the planetary nature of the system questionable.

To search for faint stars close to the target star which are not visible on conventional CCD images, the TCI can be used to observe the target stars, as the high frame-rate imaging capabilities of the TCI allows for long exposures of a bright target, without saturating the CCD. After the observation, some percentage of the best exposures can be combined to get a high dynamical range without losing spatial resolution. In Southworth et al. (2014) and Mancini et al. (2014a) this method was used, and it was found that there were either no nearby stars, or that the closest stars could only have a negligible effect on the results.

3.7 Conclusion

A two-colour EMCCD instrument for the SONG 1m telescopes and the Danish 1.54m telescope has been developed and we have detailed the design and implementation of this instrument. The TCI is the first routinely operated multi-colour instruments providing LI photometry. The Odin software framework enables these routine observations and has been prepared to control the TCI locally and remotely.

The EMCCD cameras are used to do high frame-rate imaging in the visual and red bands simultaneously. We show that by shifting-and-adding the EMCCD data, the spatial resolution is improved compared with conventional imaging, even at the 10 Hz frame-rate, that is the default at the DK154.

For a 1% selection we find that the FWHM is 35% sharper on average compared to conventional observations, and for the best $\sim 10\%$ of the 1% selections the FWHM is improved by 50% or more. For the 100% selection the FWHM is about 20% sharper on average. At the 1% selection, $\sim 25\%$ of all observations have a FWHM below $0.\!\!''5$, while $\sim 8\%$ are below $0.\!\!''4$. These numbers drop to 4% and 0.1%, respectively, at the 100% selection, while for conventional imaging they are an order of magnitude lower.

Imperfections in the DK154 optics introduce a triangular coma that becomes very distinct at spatial resolutions below $0.\!\!''5$, and thus limit the achievable resolution. With the near diffraction limited system on the SONG telescopes, we expect to

reach spatial resolutions down to $0\rlap{.}''2$.

We find that it is possible to reach a photometric precision of a few millimagnitudes for a $I = 15.3$ mag star using the TCI and that high-precision photometry of EMCCD data in crowded fields is possible. Using `DanDIA` (a difference image analysis pipeline using discrete pixel kernels), we are able to achieve a photometric precision several times better than that achieved with the PSF fitting photometry package DaoPhotII for observations of the dense globular cluster ω Cen.

EMCCD observations have been performed on a regular basis at the DK154 for several years now. This has lead to a number of interesting results including the detection of new microlensing exoplanets, the detection of previously unknown variable stars in the cores of crowded, and well-studied, globular clusters, and the discovery of rings around the asteroid-like object Chariklo, which thus became the smallest solar system object known to have rings.

Chapter 4

New variables in NGC 6981

A census of the variable stars in the globular cluster NGC 6981 was performed by Bramich et al. (2011, hereafter B11). Using data from 10 nights of observations with a conventional CCD they were able to confirm the variability of 29 stars and refute the suspected variability of 20 others. Furthermore, 11 new RR Lyrae stars and 3 new SX Phoenicis stars were found in the study, bringing the total number of confirmed variable stars in NGC 6981 to 43.

A problem with using a conventional CCD is that to obtain a reasonable signal-to-noise ratio (S/N) for the fainter objects in an image, the pixels in the brightest stars may well be saturated. For DIA, which is currently the best way to extract precise photometry in crowded star fields (e.g. towards the Galactic bulge, in the central regions of globular clusters, etc.), the saturation of the brightest stars is even more problematic because the saturated pixels affect nearby pixels during the convolution of the reference image. Hence we cannot perform photometric measurements using DIA near saturated stars in conventional CCD images, which has a negative impact on the completeness of variability studies in crowded fields. In B11, there are 4 saturated stars in the central region of their V reference image for NGC 6981, and it is therefore conceivable that their variable star census could have missed relatively bright variable stars (e.g. RR Lyraes). An improved completeness in variability studies makes it possible to draw firmer conclusions about Oosterhoff classification (Smith, 1995) and to examine whether there is a gradient in the physical properties between the central and outer parts of the cluster.

Electron-Multiplying CCDs (EMCCDs) are conventional CCDs with an extended serial register where the signal is amplified by impact ionisation before it is read out. This means that the readout noise is negligible when compared to the signal, even at very high readout speeds (10-100 frames/s), enabling the possibility of high frame-rate imaging. Numerous articles have described the possibility of using EMCCDs to obtain very high spatial resolution; see for instance Mackay et al. (2004) and Law et al. (2006). However, using EMCCDs to perform precise

time-series photometry without throwing away photons (i.e. *not* Lucky Imaging) is a new area of investigation and the applications are just starting to be explored. With high frame-rate imaging much brighter stars can be observed without saturating the CCD and the individual exposures can be combined into stacked images at a later stage in order to achieve the required S/N for the objects of interest. We note that EMCCD exposures need to be calibrated in a different way to conventional CCD imaging data. The algorithms required to do this have already been developed and described by Harpsøe et al. (2012b).

A previous attempt to study variability in the central region of a globular cluster using EMCCD data has been made by Díaz-Sánchez et al. (2012). They used FastCam at the 2.5m Nordic Optical Telescope to obtain 200000 exposures of the globular cluster M15 with an exposure time of 30 ms. To study the variable stars, they made a Lucky Imaging selection of the 7% sharpest images in each time interval of 8.1 minutes. This resulted in 20 combined images each of exposure time 21 s, where each image comes from the combination of 700 short exposures. To extract the photometry they used standard DAOPHOT PSF fitting routines. They did not find any new variable stars and no analysis of the photometric precision achieved is offered.

The DIA technique, first introduced by Alard et al. (1998), has been improved by revisions to the algorithm presented by Bramich (2008) and Bramich et al. (2013) and is the optimal way to perform photometry with EMCCD data in crowded fields. This method uses a numerical kernel model instead of modelling the kernel as a combination of Gaussian basis functions and can thus give better photometric precision even in very crowded regions (Albrow et al., 2009). The method is also especially adept at modelling images with PSFs that are not well approximated by a Gaussian.

Using the superior resolution provided by high frame-rate imaging EMCCDs in tandem with DIA we can probe the surroundings of bright stars for variable stars which are inaccessible with conventional CCD imaging. Using this technique we are able to present EMCCD photometry of two new RR Lyrae stars in the central region of NGC 6981.

4.1   Data and reductions

The data were obtained over two half nights (26th and 27th August 2012) at the Danish 1.54m Telescope at La Silla Observatory, Chile, using the Andor Technology iXon+ model 897 EMCCD camera. The imaging area of the camera is 512x512 16μm pixels with a pixel scale of 0$.''$09 which gives a 45×45 arcsec^2 field-of-view (FOV). With such a small FOV, we chose to target the crowded central region of NGC 6981 including the saturated stars from B11. The camera is

equipped with a special long-pass filter with a cut-on wavelength of 650nm. The cut-off wavelength is determined by the sensitivity of the camera which drops to zero 0% at 1050 nm over about 250 nm. The filter thus corresponds roughly to a combination of the SDSS i'+z' filters (Bessell, 2005). A total of 44 observations with a frame-rate of 10 Hz were obtained. Each observation contains between 3000 to 3500 exposures.

Using the algorithms described in Harpsøe et al. (2012b), each exposure is bias, flat, and tip-tilt corrected, and the instantaneous image quality (PSF width) is found. Then, for each observation, the exposures are combined into images in two distinct ways:

Quality-binned: exposures are grouped according to a binning in image quality and combined to produce images that cover a range in point-spread-function (PSF) width.

Time-binned: exposures are grouped into time bins of width 2 minutes to achieve a reasonable S/N at the brightness of the RR Lyrae stars. As opposed to Lucky Imaging, all frames are used. This gives a total of 125 data points in each light curve.

To extract the photometry from the time-binned images we used the `DanDIA` pipeline[1] (Bramich, 2008; Bramich et al., 2013). The pipeline has been modified to stack the sharpest of the quality-binned images to create a high-resolution reference image from which the reference fluxes and positions of the stars are measured. The reference image, convolved with the kernel solution, is subtracted from each of the time-binned images to create difference images, and, in each difference image, the differential flux for each star is measured by scaling the PSF at the position of the star (see B11 for details). Note that we have further modified the `DanDIA` software to employ the appropriate noise model for EMCCD data (Harpsøe et al., 2012b).

4.2 Results

In order to detect new variable stars in our data, we constructed and visually inspected an image representing the sum of the absolute-valued difference images with pixel values in units of sigma. We found two new variable stars which we assign names V57 and V58, and the details of which are given in Table 4.1. Both stars are located close to a bright star as can be seen in Fig. 4.1. In the B11 data, both of these variables are within the area that cannot be measured because of the saturated pixels from the bright star. Using the saturation limits from B11 it can

---

[1] `DanDIA` is built from the DanIDL library of IDL routines available at http://www.danidl.co.uk

Table 4.1: Details of the two new variable stars found in NGC 6981.

Variable Star ID	Var. Type	RA (J2000.0)	Dec. (J2000.0)	T_{max} (d)	P (d)
V57	RR1	20 53 27.38	-12 32 13.3	6166.779	0.334
V58	?[a]	20 53 27.12	-12 32 13.9	6166.76	0.285

Notes. The celestial coordinates correspond to the epoch of the reference image, which is the heliocentric Julian date ~2456167 d. The epoch of maximum light is given as a heliocentric Julian date (2450000 +) in column 5 and the period is given in column 6. [a] We are unable to classify this variable (see Sec. 4.2)
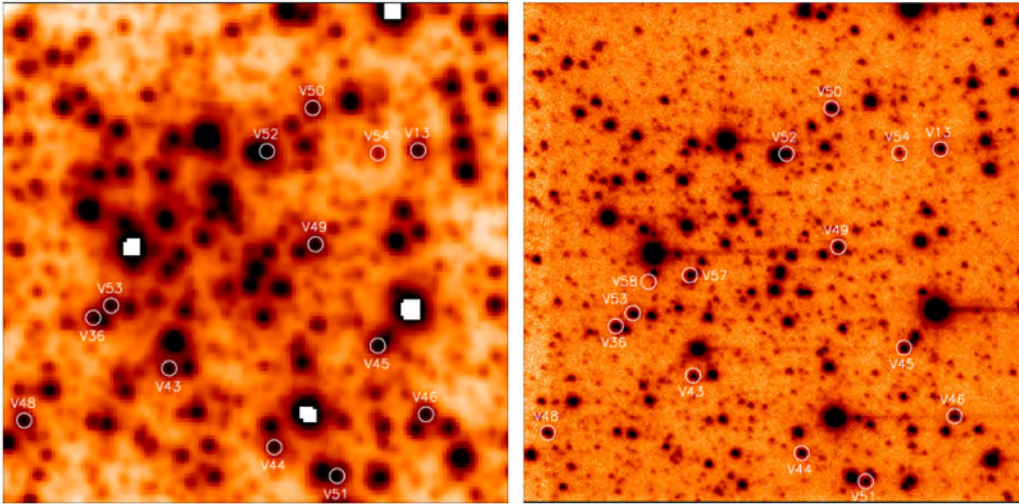
Figure 4.1: Left: A cut-out of the B11 V reference image corresponding to the field of view of the EMCCD camera. Right: Finding chart (constructed using our reference image) for the variables confirmed by B11 and the two new variables V57 and V58 (note that V58 is not the star that is located at the upper right edge of the circle). North is up and East is to the right. The image size is 45×45 arcsec^2. Notice the greatly improved resolution compared to the B11 finding chart.

be concluded that the bright star is brighter than 14th magnitude in V. In our data we find that the bright star is about 4 magnitudes brighter than the RR Lyrae stars, which suggest that it is V~ 13 mag.

The light curves for the two variables are shown in Fig. 4.2. There is increased scatter towards the end of each night which is due to a combination of high airmass and deteriorating seeing. The variable star periods were estimated using the string-length statistic S_Q (Dworetsky, 1983) and the phased light curves are shown in Fig. 4.3.

V57: With a period of 0.334 days, a sinusoidal-like light curve, and a brightness

(a) V57

(b) V58
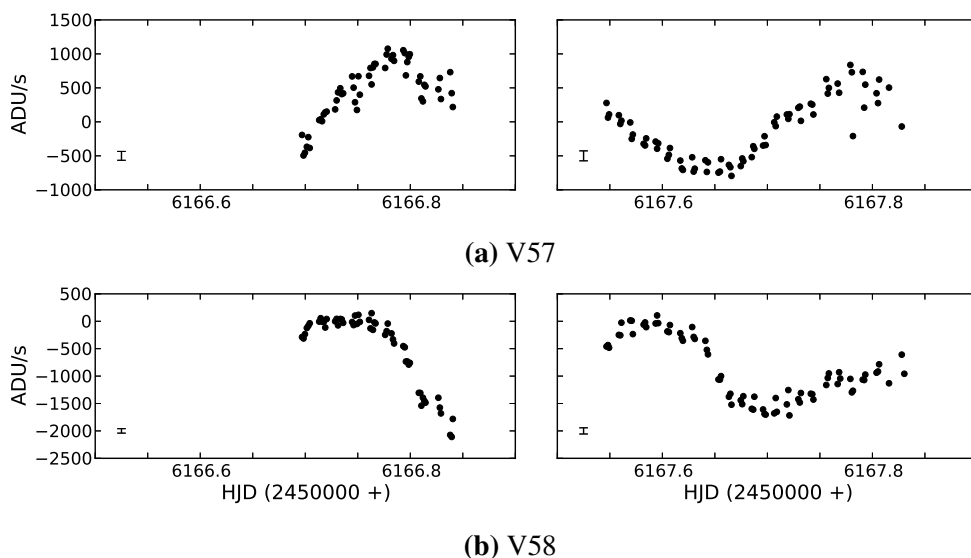
Figure 4.2: Light curves, plotted in differential flux units, for the two new variable stars. Left and right panels show the first and second nights, respectively. The typical photometric uncertainty is plotted as an error bar in each panel.

on the reference image similar to that of the other RR Lyrae stars, we can safely classify this variable as a first-overtone RR Lyrae star (RR1).

V58: This object has no detectable PSF-like peak in the reference image even though it shows clear PSF-like variations in the difference images. Hence the associated object is fainter than the cluster RR Lyrae stars. The period of 0.285 days is typical of an RR1 star, although the light curve clearly deviates somewhat from being sinusoidal with relatively flat peaks and sharp drops in intensity. This star could be an eclipsing binary or an RR1 star behind the cluster. However, due to the lack of decisive evidence for either classification, we prefer to leave the variable as unclassified.

The discovery of a new RR1 variable in NGC 6981 changes the mean period of the RR1 stars from 0.308 d (B11) to 0.312 d. The updated ratio of the number of RR1 to RR Lyrae stars is found to be ~0.17 (compared to ~0.14 in B11). Both of these quantities still agree very well with the classification of NGC 6981 as an Oosterhoff type I cluster (Smith, 1995).

4.3 Conclusions

Using EMCCD data with DIA we found two previously unknown variable stars in the crowded central region of the globular cluster NGC 6981. We have classified
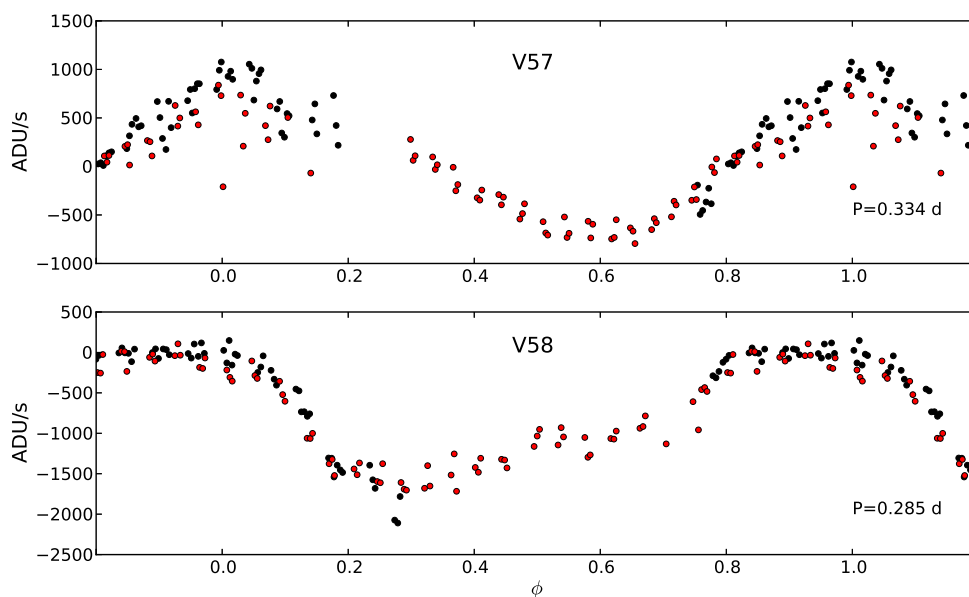
Figure 4.3: Phased light curves for the two new variable stars, plotted in differential flux units and using the periods from Table 4.1. Black and red dots represent the data from the first and second nights of observation, respectively. The typical uncertainty in the period is about 0.01 d for both variables

one variable as a first-overtone RR Lyrae and we have been unable to classify the other. The discovery of the new RR1 star consolidates the classification of NGC 6981 as an Oosterhoff type I cluster.

Both variables are located in a crowded field and close to a much brighter star. The previous study by B11 employing conventional CCD data with DIA failed to find these variables. Our discovery of these new variables in a carefully studied globular cluster is thus one of the first results to demonstrate the power of EMC-CDs for high-precision time-series photometry in crowded fields. This means that EMCCDs can improve the results in a number of areas in astrophysical research, for instance the search for Earth-mass exoplanets in gravitational microlensing events, or, as mentioned here, a better constraint on the physical parameters of globular clusters.

Chapter 5

Variables in five metal-rich clusters

Galactic globular clusters represent some of the oldest stellar populations in the Galaxy and their study can provide important insights into the formation and early evolution of the Galaxy. The stars in globular clusters are believed to have formed roughly at the same time (although there is also mounting evidence for some clusters having formed via several episodes of star formation), from the same primordial material, and with the same composition. This should lead to a homogeneity in certain fundamental properties of the stars within each cluster, but with differences between the clusters. Knowledge about these properties, such as metallicity, age and kinematics, are therefore important.

One way to obtain better constraints on some of these physical parameters is to study the population of variable stars, especially RR Lyrae stars.

As part of a series of papers on detecting and characterising the variable stars in globular clusters (e.g. Kains et al., 2013a; Kains et al., 2012; Figuera Jaimes et al., 2013; Skottfelt et al., 2013b; Arellano Ferro et al., 2013b; Bramich et al., 2011), we present our analysis of EMCCD observations of five metal-rich ([Fe/H] > -1) globular clusters. The clusters are listed in Table 5.1 along with their celestial coordinates, metallicity, and central concentration parameter.

The variable star populations of all five clusters have been examined previously, but the dates, methods, and completeness of these studies varies a lot.

NGC 6388 and NGC 6441 have been thoroughly studied. The observations made by Pritzl et al. (2001) and Pritzl et al. (2002), where PSF-fitting photometric methods were used, were re-analysed by Corwin et al. (2006) using image subtraction methods, and this revealed a number of new variables, especially in the crowded central regions. NGC 6441 was furthermore included in a Hubble Space Telescope (HST) snapshot program where many new variables were detected (Pritzl et al., 2003).

Although NGC 6528 has been heavily studied due to its very high metal abundance, no variable stars have been found to date.

Table 5.1: Coordinates and physical parameters of the five clusters

Cluster	RA (J2000.0)	Dec. (J2000.0)	[Fe/H]	c
NGC 6388	17:36:17.23	-44:44:07.8	-0.55 ± 0.15	1.75
NGC 6441	17:50:13.06	-37:03:05.2	-0.46 ± 0.06	1.74
NGC 6528	18:04:49.64	-30:03:22.6	-0.12 ± 0.24	1.5
NGC 6638	18:30:56.10	-25:29:50.9	-0.95 ± 0.13	1.33
NGC 6652	18:35:45.63	-32:59:26.6	-0.81 ± 0.17	1.8

Notes. The celestial coordinates are taken from Harris (1996) (2010 edition). Col. 4 gives the metallicity of the cluster (from Roediger et al., 2014). Col. 5 gives the central concentration $c = \log_{10}(r_t/r_c)$, where r_t and r_c are the tidal and core radii, respectively (from Harris, 1996, (2010 edition)).

Since the central region of NGC 6638 is not heavily crowded, Rutily et al. (1977) were able to find several variable stars very close to the centre using only photographic plates. They were, however, not able to determine their periods.

Hazen (1989) found several variables inside the tidal radius of NGC 6652, but none in the relatively crowded centre.

Due to the relatively small field-of-view (FoV) of the instrument we used, $45'' \times 45''$, we only observed the central part of these clusters. These are the regions of the clusters which benefit the most from the gain in spatial resolution afforded by EMCCD observations. Therefore, this study cannot be taken as a complete census of the variable star population in each cluster, but only of their crowded central regions. Another important part of the article is to show that the techniques introduced in Skottfelt et al. (2013b), i.e. using the very high spatial resolution and high-precision photometry of EMCCDs to locate variable stars in crowded fields, can be performed routinely on a much larger scale.

5.1   Data and reductions

5.1.1   Observations

The observations were carried out with the EMCCD instrument at the Danish 1.54m telescope at La Silla, Chile. The EMCCD instrument consists of a single Andor Technology iXon+ model 897 EMCCD camera which has an imaging area of 512×512 16μm pixels. The pixel scale is $\sim 0\rlap{.}''09$, and the FoV is therefore $45'' \times 45''$. For these observations a frame-rate of 10 Hz and an EM gain of 1/300 photons/e^- was used. The small FoV means that we were limited to targeting the crowded central regions of the clusters. The camera sits behind a dichroic mirror that acts as a long-pass filter with a cut-on wavelength of 650 nm. The cut-off

wavelength is determined by the sensitivity of the camera which drops to zero at 1050 nm over about 250 nm. The filter thus corresponds roughly to a combination of the SDSS i' + z' filters (Bessell, 2005).

The first block of observations were made over a five-month period, from the end of April 2013 to the end of September 2013. Each cluster was observed once or twice a week resulting in between 20 and 40 observations of each cluster. Due to the small FoV, it was unfortunately necessary to reject a number of the observations because of bad pointing. Because the crowded central parts of the clusters were targeted, we found that it was not possible to gain any useful information from observations that had a seeing of worse than $1''5$ in full-width at half-maximum (FWHM).

Thus only 10 to 15 observations per cluster were found to be useful, which made it nearly impossible to make reasonable period estimates of the variable stars. It was thus decided to perform a second block of observations over a 6 week period from mid-April 2014 to the start of June 2014. This increased the number of epochs to between 28 and 37, which enabled us to derive much better period estimates.

To achieve a reasonable S/N, each observation has a total exposure time of 8 minutes, except for NGC 6441 where they are 10 minutes long. With the frame-rate of 10 Hz, the 8 and 10 minute observation consist of 4800 and 6000 single exposures, respectively.

5.1.2   EM data reduction

The algorithms described by Harpsøe et al., 2012b were used to make bias, flat and tip-tilt corrections, and to find the instantaneous image quality (PSF FWHM) for each exposure.

The tip-tilt correction and image quality are found using the Fourier cross correlation theorem. Given a set of k exposures, each containing i pixel columns and j pixel rows, a comparison image $C(i, j)$ is constructed by taking the average of 100 randomly chosen exposures. The cross correlation $P_k(i, j)$ between C and a bias- and flat-corrected exposure $I_k(i, j)$ can be found using

$$P_k(i, j) = \left| FFT^{-1} \left[FFT(C) \cdot \overline{FFT(I_k)} \right] \right| \qquad (5.1)$$

where FFT is the fast Fourier transform. The appropriate shift, that will correct the tip-tilt error, can now be found by locating the (i, j) position of the global maximum in P_k.

A measure for the image quality q_k is found by scaling the maximum value of P_k with the sum of its surrounding pixels within a radius r

$$q_k = \frac{P_k(i_{\max}, j_{\max})}{\sum_{|(i-i_{\max}, j-j_{\max})| < r} P_k(i, j)}. \qquad (5.2)$$

Using this factor, instead of just the maximum value of the pixel values in the frame (Smith et al., 2009), helps to mitigate the effects of fluctuations in atmospheric extinction and scintillation that can happen over longer time scales.

A cosmic ray detection and correction algorithm was used on the full set of exposures in each observation. For a conventional CCD, where the noise is normally distributed, the mean and sigma values of each (i, j) pixel in the frame over all k exposures, can be found. Sigma clipping can then be used to reject cosmic rays. For an EMCCD the noise is not normally distributed, and we have therefore developed a method that takes this into account (Skottfelt et al., in prep.). Instead of finding the mean value, the rate of photons is estimated for each pixel in the frame over all the frames. Using this photon rate at each pixel position, the probability p for the observed pixel values in each exposure can be calculated and if a pixel value is too improbable, then it is rejected.

The output of the EM reduction of a single observation is a ten-layer image cube, where each layer is the sum of some percentage of the shift-and-added exposures after the exposures have been organised into ascending order by image quality. The specific percentages can be modified, but to preserve as much of the spatial information as possible, we have chosen the following (non-cumulative) percentages for the layers: (1, 2, 5, 10, 20, 50, 90, 98, 99, 100). This means that the first layer contains the sum of the best 1% of the exposures in terms of image quality, the second layer the second best 1%, the third the next 3%, and so on. If the shift needed to correct for tip-tilt error is too big (more than 20 pixels) for a given exposure, then the exposure is rejected. This is done to ensure that, except for a 20 pixel border, each layer has a uniform number of input exposures. The total number of exposures used to create the ten-layer image cube might therefore be a little lower than expected.

5.1.3 Photometry

To extract the photometry from the observations, the `DanDIA` pipeline[1] was used (Bramich, 2008; Bramich et al., 2013).

The pipeline has been modified to stack the sharpest layers from all of the available cubes to create a high-resolution reference image, such that an optimal combination of spatial resolution and S/N is achieved. Using this method, we were able to achieve resolutions between $0\farcs39$ and $0\farcs53$ for the reference images for the five clusters, and still have a good S/N ratio. Table 5.2 reports the combined integration time and FWHM of each of the reference images. The peculiar PSFs that can be seen in the reference images (Figs. 5.2, 5.7, 5.12, 5.15, 5.18) come from a triangular coma that is particular to the Danish telescope and this effect

---

[1] `DanDIA` is built from the DanIDL library of IDL routines available at http://www.danidl.co.uk

Table 5.2: Reference image details.

Cluster	Exp. Time (s)	PSF FWHM	Fig. No.
NGC 6388	240.0	0$''$42	5.2
NGC 6441	312.0	0$''$39	5.7
NGC 6528	348.0	0$''$48	5.12
NGC 6638	374.4	0$''$53	5.15
NGC 6652	403.2	0$''$46	5.18

Notes. Combined exposure time and FWHM for the reference images. The reference images are used to show the positions of the variable stars in Sect. 5.2 and the last column gives the Figure numbers for these.

manifests itself under good seeing conditions. The telescope was commissioned in 1979 and is therefore not built for such high-resolution instruments.

Reference fluxes and positions of the stars are measured from the reference image. Each ten-layer cube is then stacked into a single science image. The reference image, convolved with the kernel solution, is subtracted from each of the science images to create difference images, and, in each difference image, the differential flux for each star is measured by scaling the PSF at the position of the star (for details, see Bramich et al., 2011).

The noise model for EMCCD data differs from that for conventional CCD data (Harpsøe et al., 2012b). In the EMCCD noise model for a single exposure, the variance in pixel ij is found to be

$$\sigma_{ij}^2 = \frac{\sigma_0^2}{F_{ij}^2} + \frac{2 \cdot S_{ij}}{F_{ij} \cdot G_{EM} \cdot G_{PA}} \tag{5.3}$$

where σ_0 is the CCD readout noise (ADU), F_{ij} is the master flat-field image, S_{ij} is the image model (sky + object photons), G_{EM} is the EM gain (photons/e^-) and G_{PA} is the PreAmp gain (e^-/ADU).

When N exposures are combined by summation, the pixel variances of the combined frame are thus

$$\sigma_{ij,\text{comb}}^2 = \frac{N \cdot \sigma_0^2}{F_{ij}^2} + \frac{2 \cdot S_{ij,\text{comb}}}{F_{ij} \cdot G_{EM} \cdot G_{PA}}. \tag{5.4}$$

The `DanDIA` software has therefore been further modified to employ this noise model.

In Table 5.3, we outline the format of the data as it is provided at the CDS.

Table 5.3: Format for the time-series photometry of all confirmed variables in our field of view of the five clusters.

Cluster	#	Filter	HJD (d)	M_{std} (mag)	m_{ins} (mag)	σ_m (mag)	f_{ref} (ADU s^{-1})	σ_{ref} (ADU s^{-1})	f_{diff} (ADU s^{-1})	σ_{diff} (ADU s^{-1})	p
NGC6388	V29	I	2456436.95140	14.620	5.617	0.003	44901.760	4397.950	54393.674	627.525	4.6389
NGC6388	V29	I	2456455.86035	14.375	5.372	0.003	44901.760	4397.950	87182.547	578.940	3.3446
...	...	...	...	...	...	...	...	...	...	...	...
NGC6441	V63	I	2456454.78961	16.770	7.889	0.007	9899.919	2247.418	-17795.506	260.090	6.1094
NGC6441	V63	I	2456509.61751	16.561	7.680	0.005	9899.919	2247.418	-8594.633	212.423	6.0163
...	...	...	...	...	...	...	...	...	...	...	...

Notes. The standard M_{std} and instrumental m_{ins} magnitudes listed in Cols. 5 and 6 respectively correspond to the cluster, variable star, filter and epoch of mid-exposure listed in Cols. 1–4, respectively. The uncertainty on m_{ins} is listed in Col. 7, which also corresponds to the uncertainty on M_{std}. For completeness, we also list the reference flux f_{ref} and the differential flux f_{diff} (Cols. 8 and 10 respectively)., along with their uncertainties (Cols. 9 and 11), as well as the photometric scale factor p. Instrumental magnitudes are related to the other quantities via $m_{ins} = 17.5 - 2.5 \cdot \log_{10}(f_{ref} + f_{diff}/p)$. This is a representative extract from the full table, which is available at the CDS.
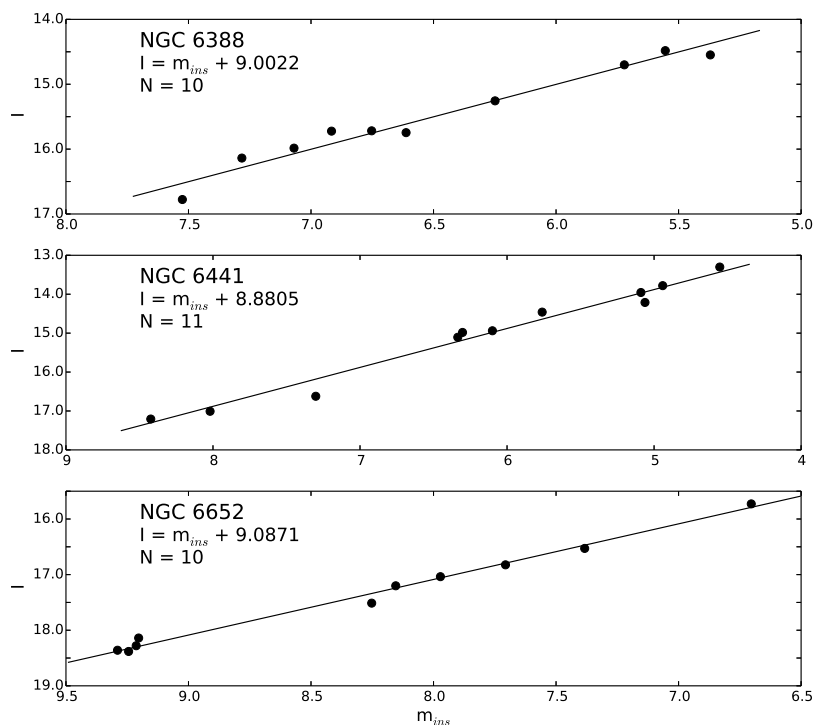
Figure 5.1: Plot of standard *I* magnitudes against the instrumental magnitudes. The solid line in each panel shows the best fit calibration.

5.1.4 Astrometry

HST observations of all five clusters have been performed during different observing campaigns (e.g. Djorgovski, 1995; Piotto, 1999; Feltzing, 2000). We made use of the high spatial resolution and precise astrometry of the HST images to derive an astrometric solution for each of our reference images.

The astrometric calibration was performed using the object detection and field overlay routines in the image display tool GAIA (Draper, 2000). The astrometric fit was then used to calculate the J2000.0 celestial coordinates for all of the variables in our field of view.

5.1.5 Photometric calibration

Using the colour information that is available from the colour-magnitude diagram (CMD) data (see Sec. 5.1.6), rough photometric calibrations can be made for NGC 6388, NGC 6441 and NGC 6652.

A number of reasonably isolated stars were selected and by matching their positions with the CMD data, their standard *I* magnitudes were retrieved. By finding

the offset between the standard *I* magnitudes and the mean instrumental magnitudes found by `DanDIA`, a rough photometric calibration was found. Fig. 5.1 shows a plot of the standard *I* magnitudes versus the mean instrumental magnitudes along with the fit for each of the clusters where CMD data are available.

Due to the non-standard filter that is used for these observations, the photometric calibration is only approximate and there is therefore some added uncertainty in the listed *I* magnitudes.

For NGC 6528 and NGC 6638 where no CMD data are available, we have chosen to adopt the photometric conversion of

$$I = m_{\mathrm{ins}} + 9.0, \tag{5.5}$$

where m_{ins} is the instrumental magnitude, to provide approximate *I* magnitudes for these two clusters as well.

5.1.6 Colour-magnitude diagrams

As we only have observations in one filter, it is not possible to make a CMD based on our own data. Three of the clusters; NGC 6388, NGC 6441 and NGC 6652; are part of *The ACS Survey of Galactic Globular Clusters* (Sarajedini et al., 2007), and the data files from the survey, that include *V* and *I* magnitudes and celestial coordinates, are available online[2].

We were able to match many of the variable stars using celestial coordinates and *I* magnitudes, enabling us to recover colour information for these objects. Unfortunately, for some of the variables, their proximity to a bright star meant that we were unable to do this.

For NGC 6528 and NGC 6638, no suitable data to create a CMD were found. The Piotto et al. (2002) study includes NGC6638, but the data files that are available do not contain any celestial coordinates and are therefore not useful for our purposes.

5.2 Results

Several methods were used to detect the variable stars in our data. Firstly an image representing the sum of the absolute-valued difference images with pixel values in units of sigma, was constructed for each cluster. These images were visually inspected for peaks indicating stars that show signs of variability. Secondly a diagram of the root-mean-square (RMS) magnitude deviation versus mean magnitude for the calibrated light curves was produced, from which we selected

---

[2]www.astro.ufl.edu/~ata/public_hstgc/

stars with a high RMS for further inspection. Finally, the difference images were blinked in sequence in order to confirm the variations of all suspected variables.

Period estimates were made using a combination of the string-length statistic S_Q (Dworetsky, 1983) and the phase dispersion minimisation method (Stellingwerf, 1978).

The results for each cluster are presented below. Note that the RR Lyrae (RRL) nomenclature introduced by Alcock et al. (2000) has been adopted for this paper; thus RR0 designates an RRL pulsating in the fundamental mode, RR1 designates an RRL pulsating in the first-overtone mode, and RR01 designates a double-mode (fundamental and first-overtone) RRL.

Stars in the upper part of the instability strip are in some parts of the literature referred to as Population II Cepheids (P2C). We have adopted the 'W Virginis' or 'CW' nomenclature, with sub-classifications CWA for CW stars with periods between 8 and 30 days, and CWB for CW stars with periods shorter than 8 days (Kholopov et al., 1998). CW stars with periods between 0.8 and 3 days are possibly anomalous Cepheids (AC), which are believed to be too luminous for their periods. If the period is longer than 30 days, then we classify them as RV Tauri stars (RV) (Clement et al., 2001).

For variable stars on the red giant branch (RGB), which in some parts of the literature are just referred to as long period variables (LPV), we have adopted the nomenclature of Kholopov et al. (1998). Thus stars on the RGB showing a noticeable periodicity and with periods over 20 days are classified as semi-regular (SR), and stars that show no evidence of periodicity are classified as long-period irregular (L). Stars with periods between 10 and 20 days, and with small amplitudes (below 0.1 mag) are classified as small-amplitude red variables (SARV). Note that some stars might actually be on the asymptotic giant branch (AGB) and not the RGB. However, distinguishing the two is difficult without a proper spectroscopic analysis and is therefore not possible from the CMDs in this study.

5.2.1   NGC 6388

5.2.1.1   Background information

The first 9 variable stars in NGC 6388 were reported by Lloyd Evans et al. (1973). These were assigned the numbers V1-V9 by Sawyer Hogg (1973) in her third catalogue of variable stars in globular clusters. Three new variables, V10-V12, were found by Lloyd Evans et al. (1977) using observations from *V* and *I* band photographic plates. They also confirmed the existence of the previous 9 variables, but were not able to provide periods for any of the variables. Using *B*-band photographic plate observations, Hazen et al. (1986) presented 14 new variables, V13-V26, within the tidal radius, and 4 field variables.

Silbermann et al. (1994) were the first to use CCD observations to search for variable stars in the cluster, and were able to find 3 new variables, V27-V29, and 4 suspected ones. Periods were given for the three new variables and for V17 and V20.

From observations obtained at the 0.9m telescope at the Cerro Tololo Inter-American Observatory (CTIO), Pritzl et al. (2002) (hereafter P02) were able to find 28 new variables, V30-V57, which includes 3 of the 4 suspected variables in Silbermann et al. (1994). The data for the P02 paper were obtained over 10 days, so only very few long period variables were found.

Due to the high central concentration (see Table 5.1) none of the variable stars found up to this point are located in the central part of the cluster, except for V29. However, when the P02 data were reanalyzed by Corwin et al. (2006) (hereafter C06) using the ISIS version 2.1 image-subtraction package (Alard, 2000; Alard et al., 1998), 12 new variables, V58-V69, and 6 suspected ones, denoted SV1-SV6, were found. All of these variables are either RRL or CW stars and most of them are located in the central parts of the cluster.

5.2.1.2   This study

A finding chart for the cluster containing the variables detected in this study is shown in Fig. 5.2 and Fig. 5.3 shows a CMD of the stars in our FoV, with the variables overplotted.

Fig. 5.4 shows the RMS magnitude deviation for the 1824 stars with calibrated *I* light curves versus their mean magnitude. From this plot it is evident that stars fainter than 18th magnitude have not been detected, which can probably be explained by the very dense stellar population in the central region of the cluster. This creates a very high background intensity, which makes it hard to detect faint stars, and which increases the possibility of blending, making some stars appear brighter than they are.

5.2.1.3   Known variables

All of the previously known variables within our FoV are recovered in this analysis. The light curves for these variables are shown in Fig. 5.5 and their celestial coordinates and estimated periods are listed in Table 5.4, along with the periods found in C06. The table also reports the mean *I* magnitude, the amplitude in our filter, and the classification of the variables.

A discussion of individual variables is given below, but generally it can be noted that we find similar periods to those given in C06. Only the three CWs; V70, V72 and V73; have very different periods. In C06 these three stars are listed as suspected variables (SV) due to uncertainty in the classification.
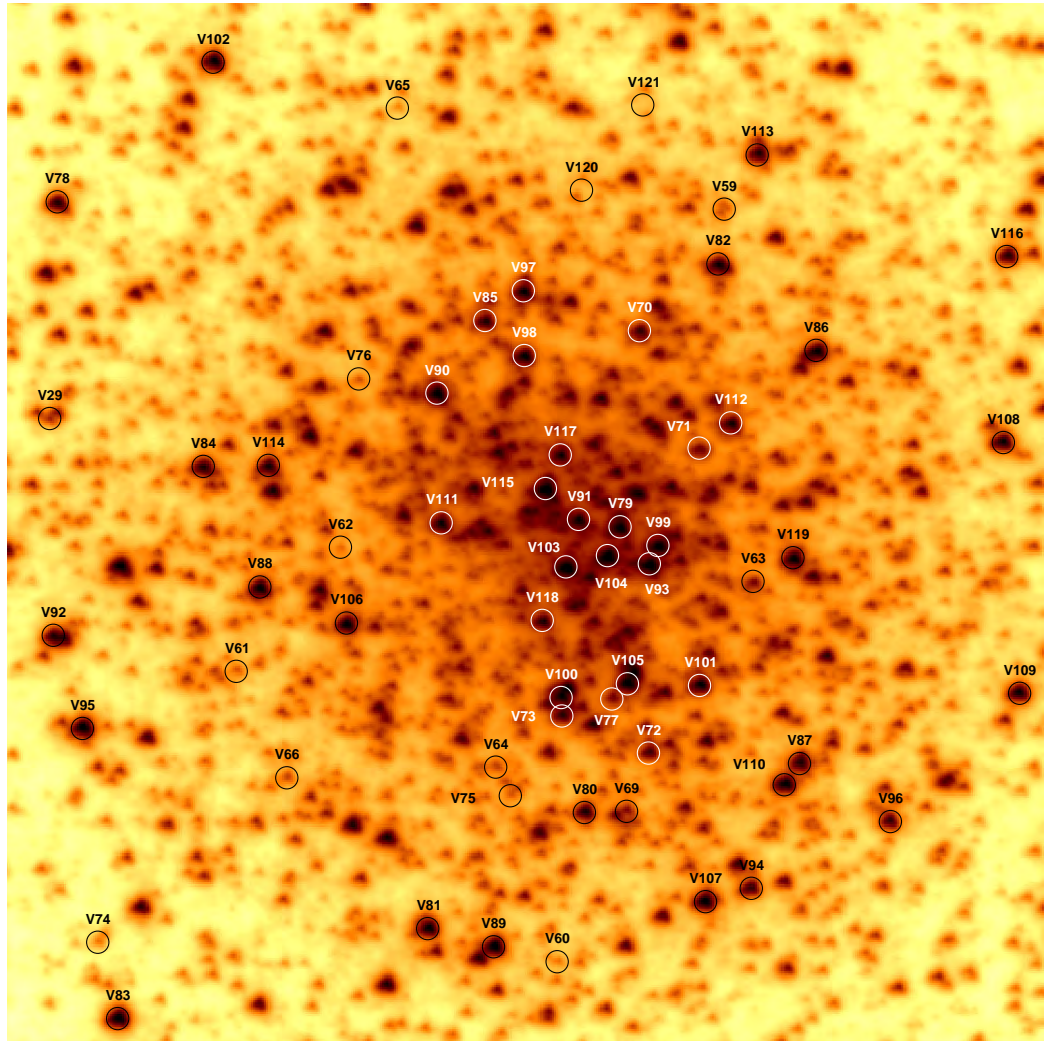
Figure 5.2: NGC 6388: Finding chart constructed from the reference image marking the positions of the variable stars. Labels and circles are white/black only for clarity. North is up and East is to the right. The cluster image is ∼ 41″ by 41″.

We find some variables to be somewhat brighter than would be expected for their classification. This is most likely due to blending with very close neighbours which, as mentioned above, can lead to an overestimation of the reference flux (e.g. see col. 9 of Table 5.4). An overestimated reference flux subsequently leads to an underestimation of the amplitude of the variable star. Errors in the mean magnitudes might also be caused by the rough photometric calibration, but this should only give discrepancies on a much lower level, and should not affect the amplitude.

Unless otherwise stated below, the classifications that are given in P02 or C06 are
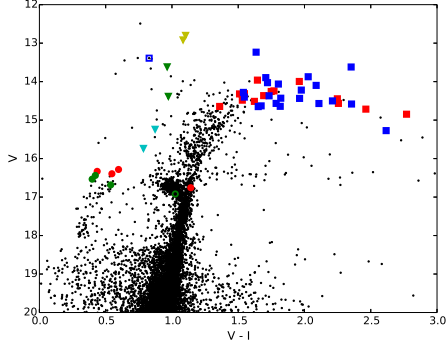
Figure 5.3: NGC 6388: $(V − I), V$ colour-magnitude diagram made from HST/ACS data as explained in Sect. 5.1.6. The stars that show variability in our study are plotted as follows: RRL as filled circles (RR0 in red, RR1 in green, RR01 in blue), CW as filled triangles (CWA in green, CWB in cyan, AC in magenta, RV in yellow), and RGB stars as filled squares (SR in red, L in blue). An open symbol means that the classification is uncertain.
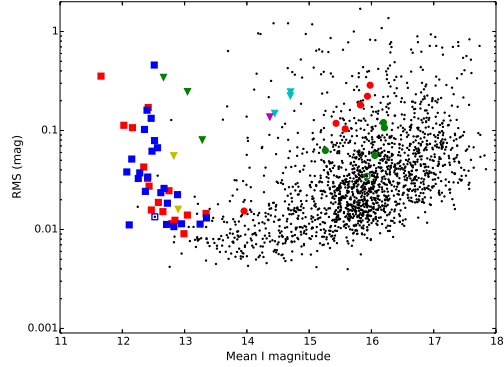
Figure 5.4: NGC 6388: Plot of the RMS magnitude deviation versus the mean magnitude for each of the 1824 calibrated I light curves. The variables are plotted with the same symbols as in Fig. 5.3.
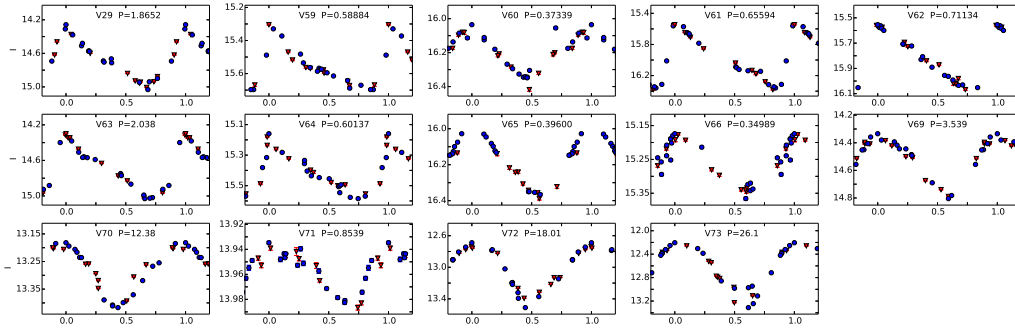
Figure 5.5: NGC 6388: Phased light curves for the known variables in our FoV. Red triangles are 2013 data and blue circles are 2014 data. Error bars are plotted but are smaller than the data symbols in many cases.

confirmed by our light curves and the CMD, and have therefore been adopted. A period-luminosity diagram for the stars in the upper part of the instability strip is shown in Fig. 5.22, and is discussed in more detail in Sect. 5.3.1.

Discussion of individual variables (square brackets gives approximate position in

Table 5.4: NGC 6388: Details of the 14 previously known variables in our FoV

Var	RA (J2000.0)	Dec. (J2000.0)	Epoch (d)	P (d)	P_{C06} (d)	$< I >$	$A_{i'+z'}$	Blend	Class.
V29	17:36:15.321	-44:44:02.62	6772.8616	1.8652	1.88^a	14.63	0.77	ii	CWB
V59	17:36:17.870	-44:43:54.77	6514.5622	0.58884	0.589	15.48	0.39	ii	RR0
V60	17:36:17.169	-44:44:24.41	6782.7705	0.37339	0.372	16.19	0.31	iii	RR1
V61	17:36:15.995	-44:44:12.73	6514.5622	0.65594	0.657	15.94	0.83	iii	RR0
V62	17:36:16.398	-44:44:07.89	6805.8471	0.71134	0.708	15.79	0.51	iii	RR0
V63	17:36:17.941	-44:44:09.50	6477.6692	2.038	2.045	14.64	0.73	ii	CWB
V64	17:36:16.958	-44:44:16.68	6797.8161	0.60137	0.595	15.35	0.43	ii	RR0
V65	17:36:16.655	-44:43:50.57	6809.7600	0.39600	0.395	16.19	0.36	iii	RR1
V66	17:36:16.174	-44:44:16.97	6763.9007	0.34989	0.350	15.25	0.19	ii	RR1
V69	17:36:17.444	-44:44:18.51	6808.8938	3.539	3.601	14.55	0.47	iii	CWB
$V70^b$	17:36:17.540	-44:43:59.52	6783.8319	12.38	~8	13.28	0.24	iii	CWA
$V71^c$	17:36:17.752	-44:44:04.20	6792.8127	0.8539	0.847	13.96	0.05	i	RR0
$V72^d$	17:36:17.532	-44:44:16.22	6784.7647	18.01	~12	13.08	0.82	iii	CWA
$V73^e$	17:36:17.211	-44:44:14.70	6792.8127	26.1	~4.5	12.74	1.11	iii	CWA

Notes. The celestial coordinates correspond to the epoch of the reference image, which is the HJD $\sim$2456522.48 d. Epochs are (HJD-2450000). $< I >$ denotes mean I magnitude and $A_{i'+z'}$ are the amplitudes found in our special $i' + z'$ filter. The blend column describes whether the star is blended with (i) brighter star(s), (ii) star(s) of similar magnitude, or (iii) fainter/no star(s). P_{C06} are periods from C06, which have been included as a reference. $^{(a)}$ Period from Pritzl et al. (2002). $^{(b)}$ Denoted SV1, $^{(c)}$ SV2, $^{(d)}$ SV4, and $^{(e)}$ SV5 in C06.

the CMD as $[V − I, V]$):

V29, V63: Based on the relation between period and luminosity compared to the other CW stars, these two stars are classified as CWB stars and not AC stars. V29 is the only variable that is also found in the P02 paper, i.e. where difference image analysis was not used.

V59, V60: No matching stars have been found in the CMD for these two variables. However, their periods, mean magnitude, and amplitude strongly indicate that the classifications as RR0 and RR1, respectively, are correct.

V61-V62, V64-V65: CMD positions, periods, magnitudes and amplitudes all verify the classifications given in C06.

V66: This RR1 seems to have an overestimated mean magnitude, and correspondingly underestimated amplitude. This is most likely caused by blending with another star, as the position in the CMD $[0.4, 16.5]$ verifies the classification.

V69: No CMD position for this star is found, but based on its period and mean magnitude it is classified as a CWB.

V70, V73: Those are two of the suspected variables from C06 that are also in our FoV. We report reliable periods in Table 5.4. The periods and CMD positions ([1.0, 14.3], [1.0, 13.6]) indicate that they are CWA stars.

V71: This star is also a suspected variable from C06. The star is highly blended with a brighter star which leads to a mean magnitude that is too bright and a heavily underestimated amplitude. No CMD position is available, but its period and light curve strongly suggest that the star is an RR0.

V72: This is the last of the C06 suspected variables in our FoV, and we report a reliable period in Table 5.4. No CMD position is found for this variable, so it could be a SR, but CWA is a more likely classification considering the relationship between magnitude and period compared to the other CW stars (see Fig. 5.22).

5.2.1.4   New variables

In this study we were able to find 48 new variable stars for NGC 6388. Their light curves are shown in Fig. 5.6 and their details are listed in Table 5.5.

Most of the new variables are RGB stars and many of them have small amplitudes, which is probably the reason why they have not been detected until now. There are however also two (possibly three) previously undetected RRL stars and three new CW stars. For many of the new long period variables it has been hard to determine a period, which may indicate that they are irregular.

Discussion of individual variables:

V74: This star has a very noisy light curve, where a period matching an RR1 has been estimated. The mean magnitude also matches this classification, but it falls on the red-clump in the CMD [1.0, 16.9]. Our RR1 classification is therefore tentative.

V75: The light curve and the position of the star in the CMD [0.5, 16.7], strongly suggest that this is an RR1.

V76: This star has a very good light curve, where the light curve shape, period and mean magnitude strongly indicate an RR0. However, the CMD position [1.1, 16.8] is a little discrepant.

V77: No CMD information is available for this star, but as the luminosity seems a bit too high compared to its period, we classify it as a possible AC (see Fig. 5.22). The star is located very close to another and much brighter variable V105, and it would have been very difficult to resolve these stars using conventional imaging.

Table 5.5: NGC 6388: Details of the 48 new variables found in the cluster.

Var	RA (J2000.0)	Dec. (J2000.0)	Epoch (d)	P (d)	$<I>$	$A_{i'+z'}$	Blend	Classification
V74	17:36:15.449	-44:44:23.35	6790.7919	0.35840	15.96	0.12	ii	RR1?
V75	17:36:17.010	-44:44:17.82	6782.7705	0.40393	16.07	0.22	ii	RR1
V76	17:36:16.483	-44:44:01.25	6792.8127	0.7574	15.98	0.67	iii	RR0
V77	17:36:17.400	-44:44:14.06	6805.8471	1.8643	14.30	0.44	iii	AC
V78	17:36:15.371	-44:43:54.06	6522.4888	24.0	12.80	0.04	iii	SR
V79	17:36:17.448	-44:44:07.26	6522.4888	27.07	12.46	0.05	ii	SR
V80	17:36:17.286	-44:44:18.53	6488.7479	30.28	12.86	0.20	iii	RV
V81	17:36:16.687	-44:44:23.02	6488.7479	33.78	12.58	0.08	iii	SR
V82	17:36:17.841	-44:43:56.93	6476.6758	40.47	12.89	0.06	ii	RV
V83	17:36:15.516	-44:44:26.38	6460.6572	50.68	12.42	0.15	iii	SR
V84	17:36:15.892	-44:44:04.61	6805.8471	55.5	12.85	0.05	iii	SR
V85	17:36:16.962	-44:43:59.02	6544.5238	56.8	13.03	0.07	iii	SR
V86	17:36:18.200	-44:44:00.41	6772.8616	57.0	12.75	0.08	ii	SR
V87	17:36:18.097	-44:44:16.73	6518.4918	58.3	12.99	0.04	ii	SR
V88	17:36:16.092	-44:44:09.41	6790.7919	58.3	12.20	0.35	iii	SR
V89	17:36:16.932	-44:44:23.78	6455.8603	70.7	12.42	0.11	iii	SR
V90	17:36:16.775	-44:44:01.86	6776.8346	70.8	12.34	0.14	ii	SR
V91	17:36:17.293	-44:44:06.94	6808.8938	113.9	12.65	0.05	iii	SR
V92	17:36:15.313	-44:44:11.19	6436.9514	114.2	12.60	0.65	ii	SR
V93	17:36:17.554	-44:44:08.74	6436.9514	157	11.97	0.43	iii	SR
V94	17:36:17.904	-44:44:21.63	6763.9007	177	13.34	0.06	iii	SR
V95	17:36:15.413	-44:44:14.89	6776.8346	180	11.91	1.06	iii	SR
V96	17:36:18.432	-44:44:19.08	-	-	12.51	1.55	iii	L
V97	17:36:17.109	-44:43:57.87	-	-	12.43	0.84	iii	L
V98	17:36:17.106	-44:44:00.43	-	-	12.52	0.60	iii	L
V99	17:36:17.588	-44:44:08.02	-	-	12.37	0.35	iii	L
V100	17:36:17.210	-44:44:13.97	-	-	12.53	0.34	ii	L
V101	17:36:17.730	-44:44:13.58	-	-	12.58	0.26	iii	L
V102	17:36:15.969	-44:43:48.64	-	-	12.54	0.21	iii	L
V103	17:36:17.241	-44:44:08.81	-	-	12.13	0.20	iii	L
V104	17:36:17.398	-44:44:08.39	-	-	12.07	0.15	iii	L
V105	17:36:17.460	-44:44:13.47	-	-	12.27	0.14	ii	L
V106	17:36:16.413	-44:44:10.89	-	-	12.28	0.12	iii	L
V107	17:36:17.731	-44:44:22.13	-	-	12.41	0.12	iii	L
V108	17:36:18.893	-44:44:04.17	-	-	12.68	0.12	iii	L
V109	17:36:18.929	-44:44:14.09	-	-	12.63	0.09	iii	L
V110	17:36:18.038	-44:44:17.56	-	-	12.38	0.08	iii	L
V111	17:36:16.778	-44:44:06.99	-	-	12.73	0.08	iii	L
V112	17:36:17.873	-44:44:03.22	-	-	12.88	0.07	iii	L
V113	17:36:17.999	-44:43:52.65	-	-	13.35	0.06	iii	L
V114	17:36:16.136	-44:44:04.61	-	-	12.71	0.05	iii	L
V115	17:36:17.172	-44:44:05.70	-	-	12.11	0.04	ii	L
V116	17:36:18.924	-44:43:56.82	-	-	13.24	0.04	iii	L
V117	17:36:17.231	-44:44:04.38	-	-	12.83	0.04	iii	L
V118	17:36:17.147	-44:44:10.91	-	-	12.95	0.04	iii	L
V119	17:36:18.093	-44:44:08.59	-	-	12.53	0.05	iii	L?
V120	17:36:17.337	-44:43:53.93	-	-	-	-	-	?
V121	17:36:17.575	-44:43:50.60	-	-	-	-	-	?

Notes. The celestial coordinates correspond to the epoch of the reference image, which is the HJD ~2456522.48 d. Epochs are (HJD-2450000). $<I>$ denotes mean *I* magnitude and $A_{i'+z'}$ are the amplitudes found in our special $i' + z'$ filter. The blend column describes whether the star is blended with (i) brighter star(s), (ii) star(s) of similar magnitude, or (iii) fainter/no star(s).
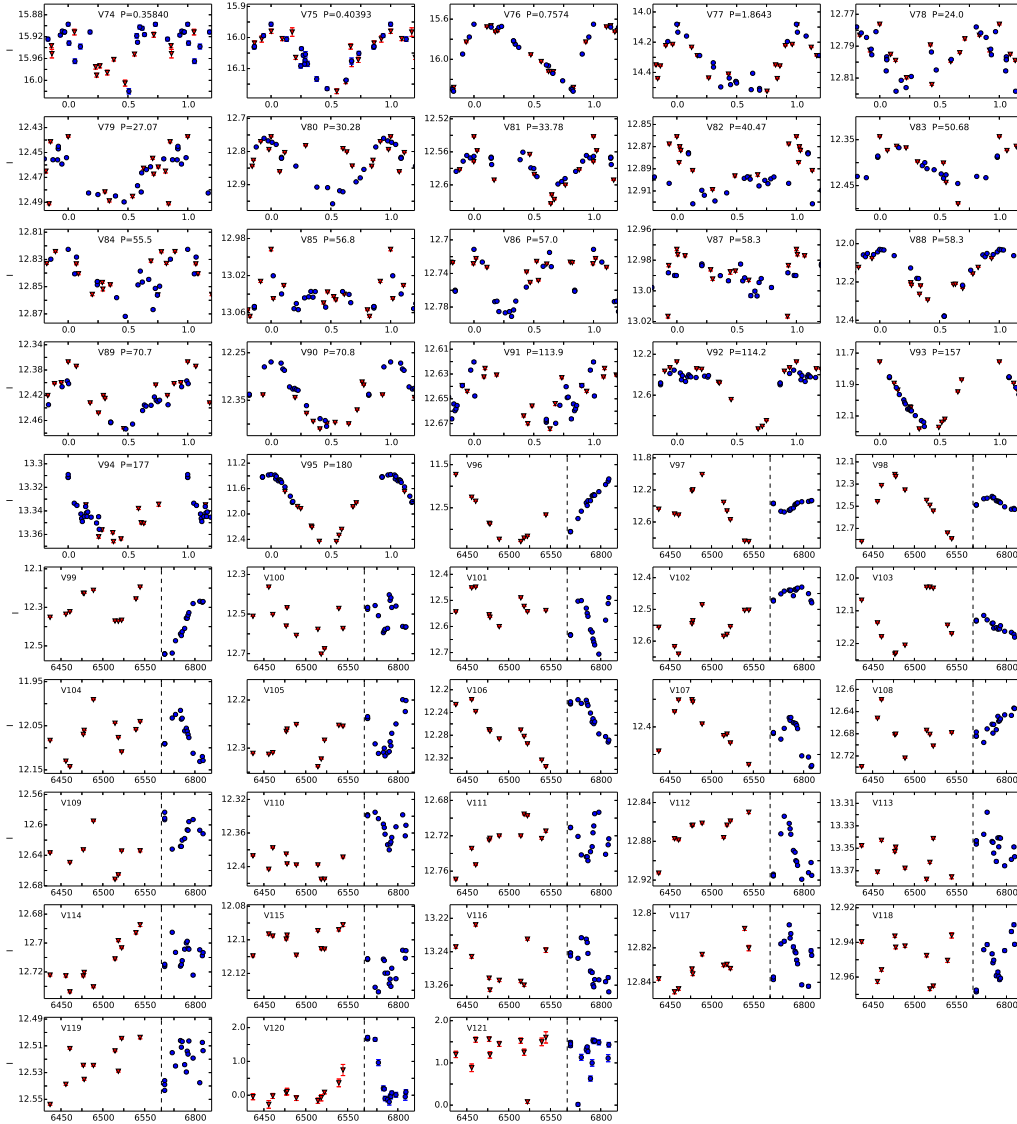
Figure 5.6: NGC 6388: Light curves for the new variables in our FoV. Red triangles are 2013 data and blue circles are 2014 data. Error bars are plotted but are smaller than the data symbols in many cases. Light curves with confirmed periods are phased. For those variables without periods the x-axis refers to (HJD - 2450000), and the dashed line indicates that the period from HJD 2456570 to 2456760 has been removed from the plot, as no observations were performed during this time range. Note that V120 and V121 are plotted in differential flux units, 10^3 ADU/s, and not calibrated I magnitudes.

V78, V79, V81: These three stars have similar positions in the CMD [1.7, 14],

and they are therefore most likely SR stars.

V80,V82: These two stars are most likely RV stars, based on their position in the CMD [1.1, 12.8] and their relation between period and luminosity (see Fig. 5.22).

V83-V92,V94,V95: All of these stars are on the RGB and combined with their long periods, these can be classified as SR stars. Most of the stars have fairly small amplitudes (0.04 – 0.15 mag)

V92, V93: These two stars are not in the CMD, but based on their periods and luminosity they are most likely SR stars.

V96-V118: These stars are also on the RGB, but it has not been possible to find any periods that phase their light curves satisfactorily. We have therefore classified them as L stars.

V119: The position of this star in the CMD [0.8, 13.4] puts it in the CW region. However, we have not been able to find a period that phases the light curve properly and the star has therefore been tentatively classified as an L star.

V120, V121: These two stars were not identified by the pipeline and no stars are visible at these positions on the reference image. However, when blinking the difference images some variability is clearly seen and the differential fluxes have thus been measured for these positions in the difference images. This means that there is no measurement of the reference flux and magnitudes or amplitudes are therefore not given. The fact that the stars are not visible on the reference image is probably because they are very faint at the epoch of the reference image. No good candidates for the stars have been found in the CMD, and no reasonable periods could be estimated. Without more information it is hard to classify the two stars, but one possibility could be a type of cataclysmic variable, as these are known to have prolonged low and high states, which can be quasi-periodic or have no clear periodicity.

5.2.2 NGC 6441

5.2.2.1 Background information

The first 10 variables in NGC 6441 were found by Fourcade et al. (1964). In Hesser et al. (1976) the authors report that they may have found two variable stars. These two stars are, however, found to be non-variable in Layden et al. (1999), whom made use of CCD imaging. Layden et al. (1999) were able to identify, classify, and determine periods for 31 long period variables, 11 RRL stars and 4

eclipsing binaries. A further 9 suspected variables were found but not classified. From CTIO observations, Pritzl et al. (2001) were able to find 48 new variables, of which 35 are RRL stars.

Similar to NGC 6388, this cluster has a high central concentration (see Table 5.1), and none of the variable stars found up to this point are located in the central part of the cluster, except for V63. Pritzl et al. (2003) (hereafter P03) used HST observations to reveal 41 previously undiscovered variables, V105-V145, the main part of which are located in the central parts.

The Pritzl et al. (2001) data were also re-analysed using ISIS in the C06 paper. In this analysis, five new variables, V146-V150, were found (and recovered in the HST data), but three variables (V136, V138, and V145) that were found in the HST data were not found in the ISIS analysis - all three bona-fide variables located within 10″ of the centre of the cluster.

5.2.2.2   This study

A finding chart for the cluster containing the variables detected in this study is shown in Fig. 5.7, and Fig. 5.8 shows a CMD of the stars within our FoV, with the variables overplotted.

Fig. 5.9 shows the RMS magnitude deviation for the 1860 stars with calibrated *I* magnitudes versus their mean magnitude. From this plot it is evident that stars fainter than 18th magnitude have not been detected, which can probably be explained by the very dense stellar population in the central region, similar to NGC 6388.

5.2.2.3   Known variables

All of the previously known variables within our FoV are recovered in this analysis. The light curves for these variables are shown in Fig. 5.10, and their details are listed in Table 5.6. The table includes the periods found in P03 and C06.

A discussion of individual variables is given below, but generally it can be noted that for all RRL and CW variables, the same periods are estimated as in P03 and/or C06. For the long period variables there are a few discrepancies. A number of the variables are found to be somewhat brighter than in P03. This is most likely due to blending with very close neighbours, leading to an overestimation of the reference flux.

The classification that is given in P03 and/or C06 seems to be correct in almost all cases and have thus been adopted, unless otherwise noted below. A period-luminosity diagram for the stars in the upper part of the instability strip is shown in Fig. 5.22, and is discussed in more detail in Sect. 5.3.1.

Table 5.6: NGC 6441: Details of the 35 previously known variables within our FoV.

Var	RA (J2000.0)	Dec. (J2000.0)	Epoch (d)	P (d)	P_P03 (d)	P_C06 (d)	$<I>$	$A_{i'+z'}$	Blend	Classification
V63	17:50:11.338	-37:02:47.42	6541.5439	0.69789	0.69781	0.700^a	16.60	0.45	iii	RR0
V105	17:50:12.320	-37:02:52.61	6476.7769	113.6	111.6	-	13.11	0.88	iii	SR
V110	17:50:14.068	-37:03:00.76	6770.9142	0.76869	0.76867	0.769	16.23	0.58	i	RR0
V111	17:50:13.685	-37:02:57.78	6509.6175	0.74464	0.74464	0.743	14.35	0.09	i	RR0
V112	17:50:13.607	-37:02:54.37	6454.7896	0.61415	0.61419	0.614	16.23	0.78	iii	RR0
V113	17:50:13.567	-37:02:56.68	6541.5439	0.58846	0.58845	0.586	15.40	0.36	ii	RR0
V114	17:50:13.441	-37:02:53.23	6541.5439	0.67389	0.67389	0.675	14.88	0.18	i	RR0
V115	17:50:13.276	-37:02:46.52	6795.7897	0.86315	0.86311	0.860	16.22	0.39	ii	RR0
V116	17:50:13.117	-37:03:22.64	6476.7769	0.58229	0.58229	0.582	16.43	0.89	iii	RR0
V117	17:50:13.096	-37:03:12.21	6781.7949	0.74537	0.74529	0.745	-	-	ii	RR0
V118	17:50:12.500	-37:03:20.74	6805.8572	0.9792	0.97923	0.979	16.09	0.54	iii	RR0
V119	17:50:12.451	-37:03:01.31	6541.5439	0.68627	0.68628	0.686	-	-	i	RR0
V120	17:50:12.190	-37:02:53.53	6789.7942	0.36396	0.36396	0.364	16.06	0.42	ii	RR1
V121	17:50:12.182	-37:02:59.46	6773.8400	0.83748	0.83748	0.848	15.66	0.25	ii	RR0
V122	17:50:11.783	-37:03:04.76	6789.7942	0.74270	0.74270	0.744	16.17	0.47	iii	RR0
V123	17:50:11.439	-37:03:06.89	6792.8040	0.33566	0.33566	0.336	16.49	0.28	iii	RR1
V126	17:50:12.539	-37:03:11.94	6782.7959	20.62	20.625	-	13.28	1.04	iii	CWA
V127	17:50:12.081	-37:03:12.26	6775.8182	19.77	19.773	-	13.27	0.74	iii	CWA
V128	17:50:11.799	-37:02:59.09	6790.8008	13.519	13.519	-	13.75	0.41	iii	CWA
V129	17:50:12.869	-37:03:18.03	6564.5424	17.83	17.832	-	13.18	0.59	iii	CWA
V130	17:50:14.433	-37:03:04.75	6476.7769	58.00	48.90	-	13.39	0.38	iii	SR?, L?
V132	17:50:12.869	-37:03:08.57	6784.7970	2.547	2.54737	-	14.32	0.44	i	CWB
V133	17:50:13.977	-37:02:57.05	-	-	122.9	-	12.85	0.41	iii	L
V136	17:50:12.687	-37:03:16.16	6791.7776	0.80574	0.80573	-	15.87	0.47	ii	RR0
V137	17:50:11.850	-37:03:02.97	-	-	51.2	-	13.12	0.12	iii	L
V138	17:50:14.000	-37:03:07.68	6797.8236	0.8020	0.80199	-	16.34	0.27	iii	RR0
V139	17:50:13.584	-37:03:16.12	6541.5439	249	249.1	-	12.20	1.72	iii	SR
V141	17:50:13.982	-37:03:16.11	6789.7942	0.8446	0.84475	0.847	16.08	0.20	iii	RR0
V142	17:50:13.823	-37:02:49.41	6784.7970	0.8840	0.88400	0.887	16.28	0.25	iii	RR0
V143	17:50:13.748	-37:02:47.86	6781.7949	0.8628	0.86279	0.863	16.42	0.32	iii	RR0
V144	17:50:11.341	-37:02:59.71	6782.7959	70.6	70.6	-	13.09	0.11	iii	SR?, L?
V145	17:50:12.716	-37:03:09.47	6770.8270	0.55588^b	0.55581	-	15.29	0.16	ii	RR01
V146	17:50:13.145	-37:03:00.51	6797.8236	0.40232	-	0.402	15.57	0.18	ii	RR1
V147	17:50:13.245	-37:02:52.43	6455.7466	0.35487	-	0.355	14.17	0.05	i	RR1
V148	17:50:12.798	-37:02:50.88	6454.7896	0.39045	-	0.390	15.46	0.17	ii	RR1

Notes. The celestial coordinates correspond to the epoch of the reference image, which is the HJD ~2456541.54 d. Epochs are (HJD-2450000). $<I>$ denotes mean I magnitude and $A_{i'+z'}$ are the amplitudes found in our special $i' + z'$ filter. The blend column describes whether the star is blended with (i) brighter star(s), (ii) star(s) of similar magnitude, or (iii) fainter/no star(s). P_{P03} and P_{C06}, are periods from P03 and C06, respectively, which have been included as a reference. $^{(a)}$ Period from Pritzl et al. (2001). $^{(b)}$ First-overtone period; fundamental period is found to be 0.72082 d.

Figure 5.7: NGC 6441: Finding chart constructed from the reference image marking the positions of the variable stars. Labels and circles are white/black only for clarity. North is up and East is to the right. The cluster image is ~ 41″ by 41″.

Satisfactory light curves are found for the three variables that were not detected by C06: V136, V138, and V145. Of the five new variables that C06 discovered, three (V146-V148) are within our FoV and have reasonable light curves. This highlights the power of EMCCD observations and DIA combined.
Discussion of individual variables:

V63: This RR0 is the only variable that is also found in Pritzl et al., 2001.

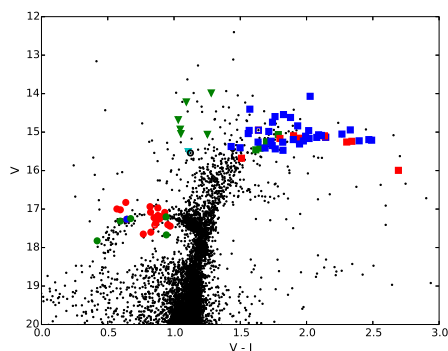**V105:** We find a slightly shorter period for this SR than in P03.

Figure 5.8: NGC 6441: $(V - I), V$ colour-magnitude diagram made from HST/ACS data as explained in Sect. 5.1.6. The stars that show variability in our study are plotted with the same symbols as in Fig. 5.3.
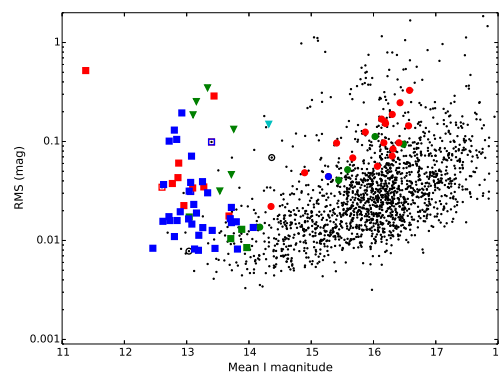
Figure 5.9: NGC 6441: Plot of the RMS magnitude deviation versus the mean magnitude for each of the 1860 calibrated I light curves. The variables are plotted with the same symbols as in Fig. 5.3.

V110, V122: No CMD positions are found for these two variables, but their periods and phased light curves clearly indicate that they are RR0 stars.

V111: This RR0 is highly blended with a brighter star, and the mean magnitude is therefore too bright. Due to the strong blending the correct position in the CMD has not been found.

V113, V121: Due to blending with nearby stars of similar brightness, these RR0 stars have overestimated mean magnitudes.

V114: This RR0 star is heavily blended with a brighter star.

V117, V119: Both stars are in a very crowded area and their positions and reference fluxes were not found by the pipeline. The correct positions of the stars were found in the summed difference image, and the differential fluxes have been measured for these positions in the difference images. Therefore, as no reference flux could be measured, magnitudes and amplitudes are not given for either of these RR0 stars.

V118: Using the period of this star, P03 and C06 can not give a certain classification, but suggest RR0 or CW. Based on the position of the star in the CMD $[0.82, 16.9]$ we classify it as an RR0 star, although the period is unusually long for this type of star.
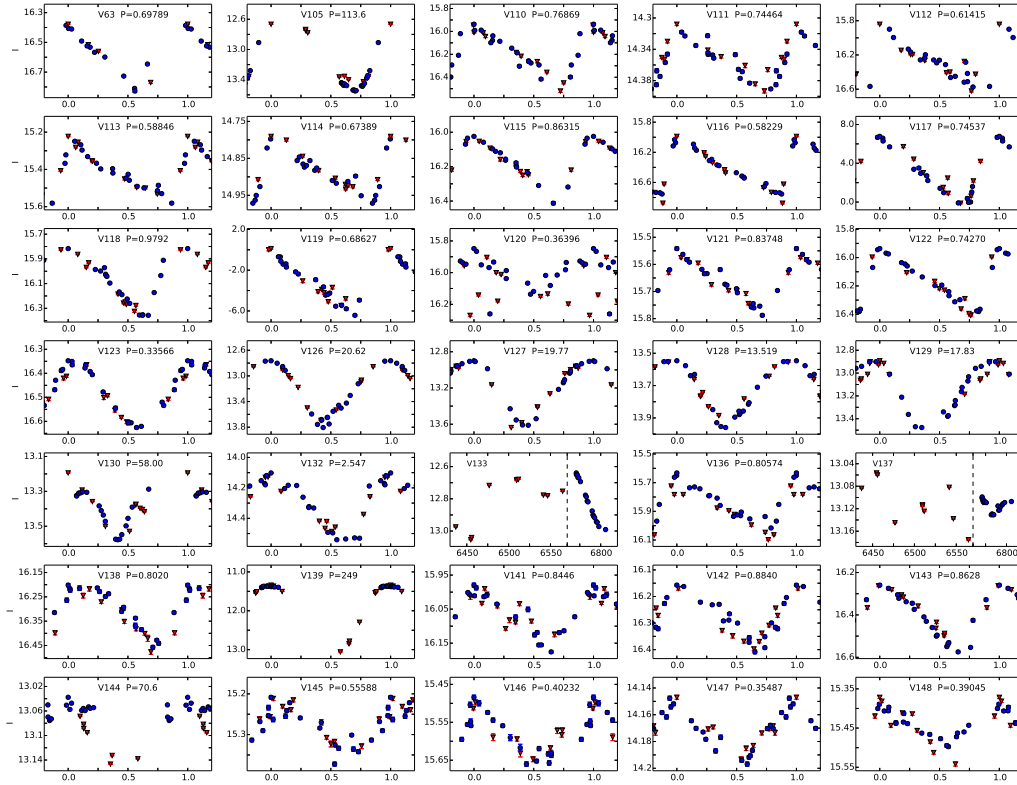
Figure 5.10: NGC 6441: Light curves for the known variables in our FoV. Red triangles are 2013 data and blue circles are 2014 data. Error bars are plotted but are smaller than the data symbols in many cases. Light curves with confirmed periods are phased. For those variables without periods the x-axis refers to (HJD - 2450000), and the dashed line indicates that the period from HJD 2456570 to 2456760 has been removed from the plot, as no observations were performed during this time range. Note that V117 and V119 are plotted in differential flux units, 10^3 ADU/s, and not calibrated *I* magnitudes.

V120: This variable is classified as an RR1 in both P03 and C06. Due to the scatter in our light curve and the position of the star in the CMD [0.60, 17.3], we have analysed the light curve for any secondary periods, but none have been found. We therefore support the RR1 classification.

V126-V129: In P03 these stars are described as CWA candidates. The positions that these stars occupy in the CMD $[(1.0 - 1.3), (14.0 - 15.5)]$, seem to support that they are indeed CWA stars.

V130: The period of P03 does not phase our light curve well and our best fit period is significantly longer. Some of the data points seem to have a sort

of systematic scatter and it may therefore be an L star, which is supported by its position in the CMD, [1.64, 15.0].

V132: This star is quite heavily blended, which is reflected in a rather scattered light curve and the fact that we found a mean *I* magnitude that is about a magnitude higher than what was found in P03. Based on its position in the CMD and the relation between period and luminosity, we classify this star as a CWB.

V133, V137: For these two stars it is not possible to phase the light curves properly with the periods given in P03, or any other period, and this suggests that they are L stars. No period is therefore given for these two variables.

V136, V138: These two RR0 stars were not found in the C06 analysis. Our data are properly phased by the periods of P03.

V139: This SR phases well with the period found by P03.

V144: The period from P03 does phase this SR reasonably well, but the phased light curve still looks a bit peculiar, so it might also be an L star.

V145: This star is highly blended with a star of similar brightness and was not found in the C06 paper. P03 classifies this as an RR1. We are able to find a fundamental and first overtone period of $P_0 = 0.72082$ and $P_1 = 0.55588$, respectively. This gives a first-overtone to fundamental period ratio of $P_1/P_0 = 0.7712$, which is only slightly higher than the 'canonical' ratio of ~ 0.745 (Clement et al., 2001). We therefore classify this as a double-mode RRL, which also agrees well with the position of the star in the CMD [0.64, 17.3].

V146-V148: These RR1 stars seems to be blended with multiple stars. However, their periods and light curves, although with some scatter, are consistent with their classification.

5.2.2.4 New variables

In this study we were able to find 49 new variable stars for NGC 6441. These are all listed in Table 5.7 and their light curves are shown in Fig. 5.11.

Similar to NGC 6388, most of the new variables are RGB stars, many with small amplitudes, which is probably the reason why they have not been detected until now. There are, however, also one (possibly two) previously undetected RRL stars and two new CW stars. For many of the new long period variables it has been hard to determine a period, which could indicate that they are irregular.

Table 5.7: NGC 6441: Details of the 49 new variables found in the cluster.

Var	RA (J2000.0)	Dec. (J2000.0)	Epoch (*d*)	P (*d*)	< *I* >	$A_{i'+z'}$	Blend	Classification
V151	17:50:11.983	-37:03:11.63	6564.5424	0.48716	16.46	0.80	iii	RR0
V152	17:50:12.843	-37:03:03.48	6564.5424	0.9432	-	-	i	RR0?
V153	17:50:12.767	-37:03:16.58	6541.5439	9.89	13.72	0.15	iii	CWA
V154	17:50:13.338	-37:03:01.06	6455.7466	10.83	13.57	0.15	iii	CWA
V155	17:50:13.231	-37:03:10.93	6564.5424	11.45	13.03	0.04	iii	?
V156	17:50:11.357	-37:03:13.57	6789.7942	11.76	13.97	0.03	iii	SARV
V157	17:50:11.670	-37:03:14.69	6775.8182	15.10	13.71	0.04	iii	SARV
V158	17:50:13.637	-37:02:48.90	6784.7970	17.50	13.89	0.05	iii	SARV
V159	17:50:13.147	-37:03:06.55	6782.7959	18.5	13.03	0.06	ii	SARV
V160	17:50:13.536	-37:03:20.37	6795.7897	20.3	13.31	0.11	iii	SR
V161	17:50:12.645	-37:03:12.61	6564.5424	24.6	12.95	0.09	iii	SR
V162	17:50:14.220	-37:02:50.97	6770.8270	29.3	13.68	0.06	iii	SR
V163	17:50:13.742	-37:03:03.30	6546.5297	41.03	12.59	0.11	iii	SR?
V164	17:50:11.919	-37:03:11.12	6564.5424	41.14	14.37	0.27	ii	?
V165	17:50:12.027	-37:03:10.81	6564.5424	51.6	12.86	0.21	iii	SR
V166	17:50:13.434	-37:02:54.72	6546.5297	52	12.83	0.17	iii	SR
V167	17:50:14.037	-37:03:02.88	6789.7942	86	12.78	0.13	iii	SR
V168	17:50:13.980	-37:03:12.93	6789.7942	128	13.13	0.11	iii	SR
V169	17:50:13.918	-37:03:25.06	-	-	12.99	0.68	iii	L
V170	17:50:13.625	-37:03:08.13	-	-	12.89	0.48	iii	L
V171	17:50:13.065	-37:02:58.75	-	-	12.71	0.29	iii	L
V172	17:50:14.561	-37:03:14.81	-	-	13.06	0.21	iii	L
V173	17:50:14.253	-37:03:04.74	-	-	13.10	0.16	iii	L
V174	17:50:12.059	-37:02:51.54	-	-	13.06	0.14	iii	L
V175	17:50:11.371	-37:03:23.18	-	-	13.27	0.14	iii	L
V176	17:50:12.222	-37:03:04.85	-	-	12.65	0.11	iii	L
V177	17:50:14.376	-37:03:19.09	-	-	13.35	0.09	iii	L
V178	17:50:12.930	-37:02:56.26	-	-	12.91	0.08	iii	L
V179	17:50:12.822	-37:03:04.36	-	-	12.72	0.07	ii	L
V180	17:50:12.433	-37:03:12.24	-	-	13.72	0.07	iii	L
V181	17:50:14.294	-37:03:15.36	-	-	13.73	0.07	iii	L
V182	17:50:13.165	-37:03:08.78	-	-	12.62	0.06	iii	L
V183	17:50:11.939	-37:02:52.42	-	-	12.72	0.06	iii	L
V184	17:50:12.906	-37:03:19.30	-	-	12.84	0.06	iii	L
V185	17:50:11.845	-37:03:00.62	-	-	13.07	0.06	iii	L
V186	17:50:13.911	-37:03:15.79	-	-	13.17	0.06	iii	L
V187	17:50:12.583	-37:02:49.07	-	-	13.25	0.06	iii	L
V188	17:50:12.364	-37:03:24.91	-	-	13.70	0.06	iii	L
V189	17:50:14.453	-37:03:08.15	-	-	13.81	0.06	iii	L
V190	17:50:13.032	-37:03:00.01	-	-	13.04	0.05	iii	L
V191	17:50:13.309	-37:03:04.07	-	-	12.46	0.04	iii	L
V192	17:50:13.406	-37:03:06.76	-	-	12.80	0.04	iii	L
V193	17:50:12.269	-37:03:10.06	-	-	13.19	0.04	iii	L
V194	17:50:13.902	-37:03:05.68	-	-	13.19	0.04	ii	L
V195	17:50:13.649	-37:02:53.87	-	-	13.41	0.04	iii	L
V196	17:50:11.542	-37:02:56.76	-	-	13.81	0.04	iii	L
V197	17:50:11.861	-37:02:49.20	-	-	14.07	0.04	iii	L
V198	17:50:13.173	-37:02:56.04	-	-	13.13	0.03	iii	L
V199	17:50:12.346	-37:02:57.29	-	-	13.46	0.03	iii	L

Notes. The celestial coordinates correspond to the epoch of the reference image, which is the HJD ~2456541.54 d. Epochs are (HJD-2450000). < *I* > denotes mean *I* magnitude and $A_{i'+z'}$ are the amplitudes found in our special $i' + z'$ filter. The blend column describes whether the star is blended with (i) brighter star(s), (ii) star(s) of similar magnitude, or (iii) fainter/no star(s).
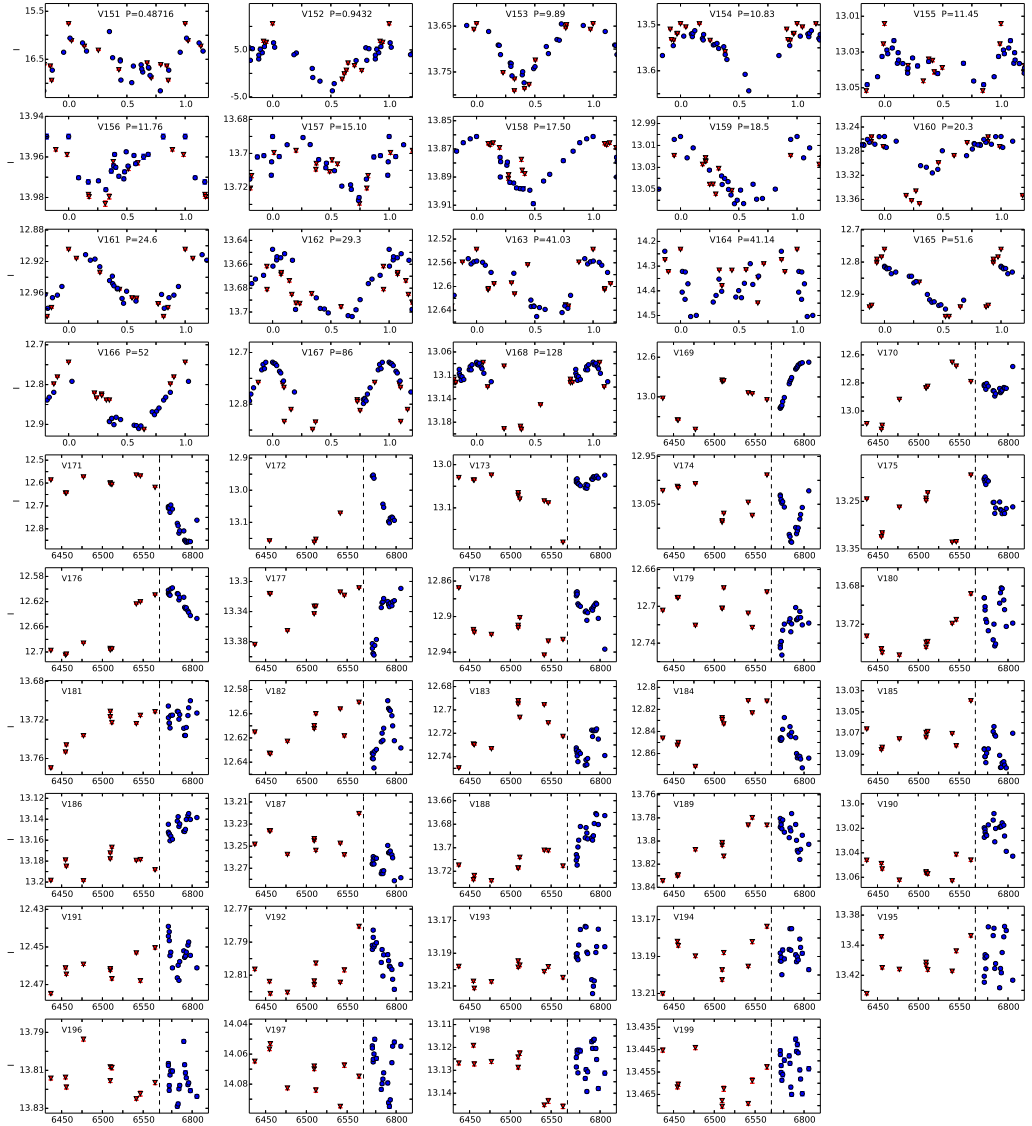
Figure 5.11: NGC 6441: Light curves for the new variables in our FoV. Red tri-angles are 2013 data and blue circles are 2014 data. Error bars are plotted but are smaller than the data symbols in many cases. Light curves with confirmed periods are phased. For those variables without periods the x-axis refers to (HJD - 2450000), and the dashed line indicates that the period from HJD 2456570 to 2456760 has been removed from the plot, as no observations were performed during this time range. Note that V152 is plotted in differential flux units, 10^3 ADU/s, and not calibrated I magnitudes.

It should be noted that three of the new variables (V151, V164, and V165) are located very close to each other. Resolving these three variables would have been

difficult using conventional imaging, as they are all within a radius of $\sim 0\rlap{.}''9$.
Discussion of individual variables:

V151: From the period and position in the CMD [0.6, 17.0] this star can be safely
classified as an RRL star, and the asymmetry of the light curve suggests
that it is most likely an RR0. The amplitude listed is very large compared
to other RRL stars, and there seems to be some scatter in the light curve
(caused by its proximity to three other brighter variables) so the actual am-
plitude is probably about $A_{i'+z'} \sim 0.8$ mag.

V152: This star is highly blended with a star of similar brightness and lies very
close to another variable star, V179. The position and reference flux were
therefore not found by the pipeline, as in the cases of V117 and V119. The
positions and differential fluxes were found manually, but again the refer-
ence flux is not measured, so no magnitude or amplitude is given. Based
on the period, light curve shape, and CMD position [0.85, 17.4], we classify
this tentatively as an RR0 star.

V153, V154: Based on their periods, light curves, and positions in the CMD
[1.05, 15.0], we classify these two stars as CWA stars.

V155: Both the period and magnitude suggest that this is either a CW or an SR
star, but the position of this star in the CMD is [−0.5, 13.5], which means
that it is far too blue to fit any of these classifications. We do not attempt to
classify this variable.

V156-V159: These stars are on the RGB in the CMD and with the short periods
and small amplitudes, they can be classified as SARV stars.

V160-V162, V165-V168: The CMD puts all of these stars on the RGB. As it has
been possible to estimate periods for them, we classify these as SR stars.

V163: This star has no CMD information, but based on the period, light curve,
and magnitude, it is most likely an SR star.

V164: The CMD position [1.1, 15.5] and the mean magnitude of this star would
normally imply that it is a CW star. However the light curve is scattered and
the derived period uncertain. We refrain from classifying this variable.

V169-V199: We have classified these RGB stars for which we have been unable
to derive periods as L stars.

5.2.3 NGC 6528

5.2.3.1 Background information

According to Sawyer Hogg (1973) there are a few variables from the rich Galactic field projected against the cluster, but none are considered to be cluster members. As NGC 6528 might be the most metal-rich cluster in the Galaxy, it has been studied quite extensively in a number of photometric studies (e.g. Ortolani et al., 1992; Richtler et al., 1998; Feltzing et al., 2002; Calamida et al., 2014). However, so far no variable stars have been reported. Ortolani et al. (1992) mention that the large spread in the RGB that is found may be due to variability, but this is not mentioned in any later article.
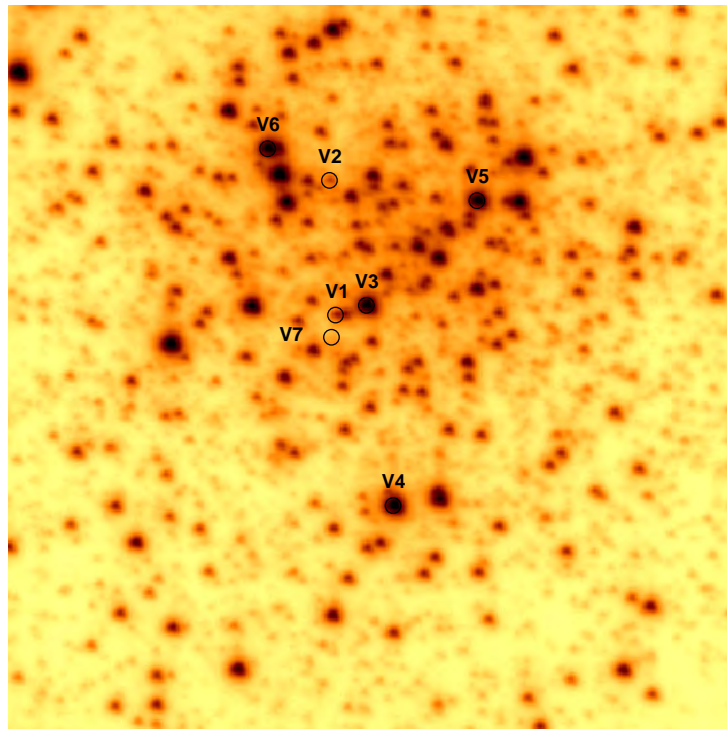

Figure 5.12: NGC 6528: Finding chart constructed from the reference image marking the positions of the variable stars. North is up and East is to the right. The cluster image is ∼ 41″ by 41″.

5.2.3.2 New Variables

A finding chart for the cluster containing the variables detected in this study is shown in Fig. 5.12, and Fig. 5.13 shows the RMS magnitude deviation for the 1103 stars with calibrated *I* magnitudes versus their mean magnitude.
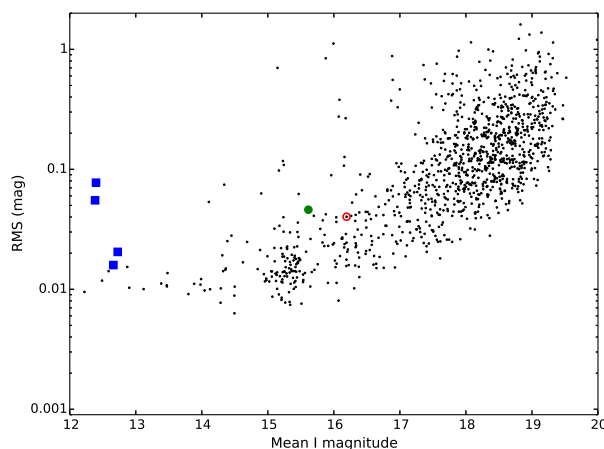
Figure 5.13: NGC 6528: Plot of the RMS magnitude deviation versus the mean magnitude for each of the 1103 calibrated *I* light curves. The stars that show variability in our study are plotted with the same symbols as in Fig. 5.3.
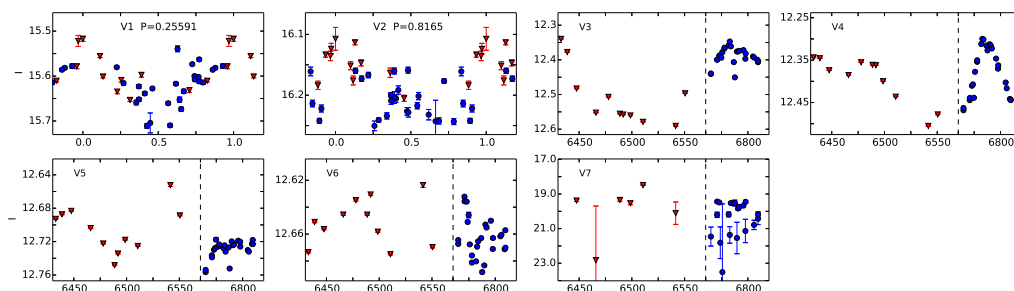

Figure 5.14: NGC 6528: Light curves for the variables in our FoV. Red triangles are 2013 data and blue circles are 2014 data. Error bars are plotted but are smaller than the data symbols in many cases. Light curves with confirmed periods are phased. For those variables without periods the x-axis refers to (HJD - 2450000), and the dashed line indicates that the period from HJD 2456570 to 2456760 has been removed from the plot, as no observations were performed during this time range.

We are able to find seven new variable stars for NGC 6528. Unfortunately there is no CMD for this cluster, which complicates the classification of the variables, but we classify one (possibly two) as RRL stars and four as long period irregular stars. The light curves for these variables are shown in Fig. 5.14 and their details are listed in Table 5.8.

V1: The period of this star suggests that it is an RR1, and the magnitude indicates that it is highly blended with a brighter star. Due to the scatter in the light curve, we have analysed it for secondary periods, but none were found.

Table 5.8: NGC 6528: Details of the 7 new variables found in the cluster.

Var	RA (J2000.0)	Dec. (J2000.0)	Epoch (*d*)	P (*d*)	< *I* >	$A_{i'+z'}$	Blend	Classification
V1	18:04:49.380	-30:03:27.25	6477.8478	0.25591	15.61	0.19	i	RR1
V2	18:04:49.368	-30:03:19.53	6541.5615	0.8165	16.18	0.14	iii	RR0?
V3	18:04:49.518	-30:03:26.74	-	-	12.46	0.25	iii	L
V4	18:04:49.614	-30:03:38.25	-	-	12.40	0.21	iii	L
V5	18:04:50.016	-30:03:20.90	-	-	12.70	0.10	iii	L
V6	18:04:49.099	-30:03:17.64	-	-	12.66	0.06	iii	L
V7	18:04:49.360	-30:03:28.52	-	-	19.6	-	-	E?

Notes. The celestial coordinates correspond to the epoch of the reference image, which is the HJD ~2456510.63 d. Epochs are (HJD-2450000). < *I* > denotes mean *I* magnitude and $A_{i'+z'}$ are the amplitudes found in our special $i' + z'$ filter. The blend column describes whether the star is blended with (i) brighter star(s), (ii) star(s) of similar magnitude, or (iii) fainter/no star(s).

V2: The period of this star indicates that it is a RR0, even though the light curve looks somewhat noisy. Since the amplitude is somewhat smaller than what we expect for an RR0 star, we leave our classification as tentative.

V3-V6: These four stars are most likely L stars, based on their magnitudes and the fact that it has not been possible to find any periods that phase their light curves in a reasonable way.

V7: The mean magnitude of this star is at the limit of our detection threshold, and it disappears in ~ 30% of our images. It is probably an eclipsing binary (E), but we refrain from making a firm classification.

5.2.4 NGC 6638

5.2.4.1 Background information

The first 19 variable stars in this cluster were found by Terzan (1968). Of these, four were classified as Mira variables with periods between 156 and 279 days, and the remaining ones were neither classified nor had their periods estimated. Sawyer Hogg et al. (1974) were able to discover the variability of a further 26 stars from a photographic collection made in 1939 and 1972. All of these 45 variable stars are distributed in a wide field of 30′ × 30′ and only a few are located close to the central parts of the cluster.

In Rutily et al. (1977) (hereafter R77) a total of 63 variables are presented. That article contains finding charts and periods for many of the variables. As NGC 6638 does not have a very dense central region, it was possible to detect variable stars quite close to the centre, but no periods for the central stars are given.
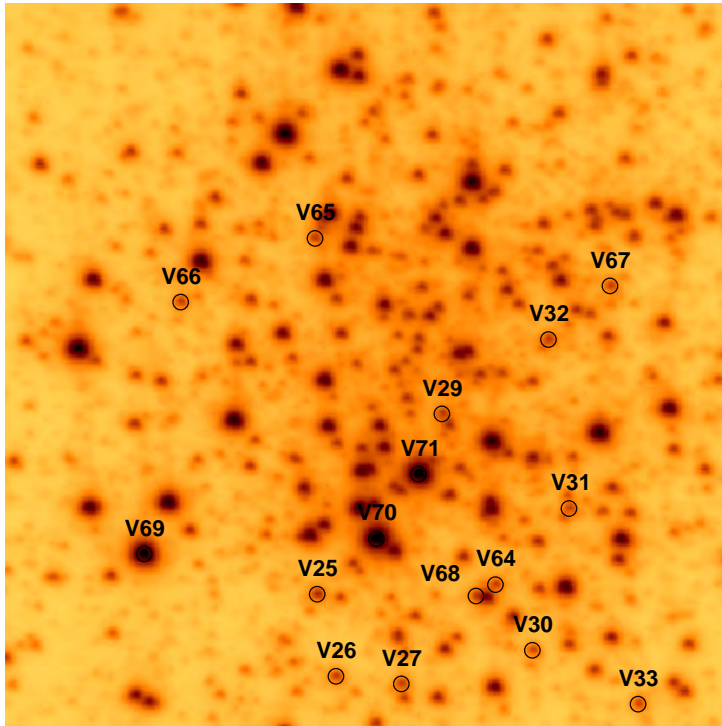
Figure 5.15: NGC 6638: Finding chart constructed from the reference image marking the positions of the variable stars. North is up and East is to the right. The cluster image is ∼ 41″ by 41″.
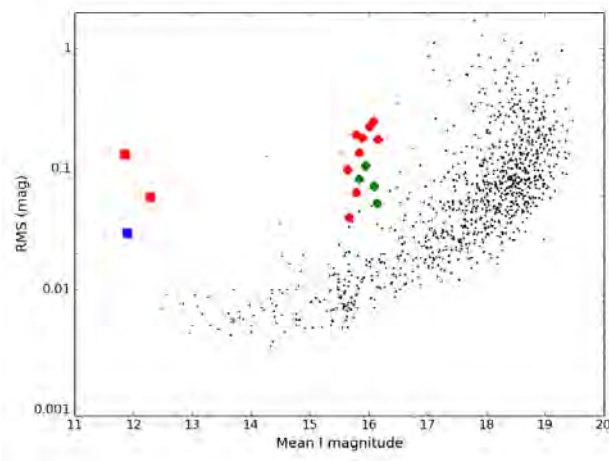

Figure 5.16: NGC 6638: Plot of the RMS magnitude deviation versus the mean magnitude for each of the 981 calibrated I light curves. The stars that show variability in our study are plotted with the same symbols as in Fig. 5.3.

A finding chart for the cluster containing the variables detected in this study is shown in Fig. 5.15. Fig. 5.16 shows the RMS magnitude deviation for the 981 stars with calibrated *I* magnitude versus their mean magnitude.

Table 5.9: NGC 6638: Details of the 8 previously known variables in our FoV.

Var	RA (J2000.0)	Dec. (J2000.0)	Epoch (*d*)	P (*d*)	$< I >$	$A_{i'+z'}$	Blend	Classification
V25	18:30:55.564	-25:30:04.05	6511.6617	0.67276	15.79	0.66	iii	RR0
V26	18:30:55.635	-25:30:08.79	6782.8404	0.66743	15.85	0.47	iii	RR0
V27	18:30:55.912	-25:30:09.31	6773.8921	0.59969	15.87	0.68	iii	RR0
V29	18:30:56.111	-25:29:53.87	6773.8921	0.257893	15.92	0.31	iii	RR1
V30	18:30:56.471	-25:30:07.56	6458.6160	0.50650	16.00	0.75	iii	RR0
V31	18:30:56.640	-25:29:59.47	6783.8751	0.45795	15.88	0.67	iii	RR0
V32	18:30:56.570	-25:29:49.75	6773.8921	0.56830	15.65	0.35	iii	RR0
V33	18:30:56.914	-25:30:10.79	6791.7951	0.32378	16.07	0.22	iii	RR1

Notes. The celestial coordinates correspond to the epoch of the reference image, which is the HJD ~2456511.65 d. Epochs are (HJD-2450000). $< I >$ denotes mean *I* magnitude and $A_{i'+z'}$ are the amplitudes found in our special $i' + z'$ filter. The blend column describes whether the star is blended with (i) brighter star(s), (ii) star(s) of similar magnitude, or (iii) fainter/no star(s).

5.2.4.2 Known variables

All of the previously known variable stars within our FoV have been located and confirmed as variables, and this is the first study to present periods and classifications for these stars. The light curves are plotted in Fig. 5.17a and their details can be found in Table 5.9.

The fact that no CMD is available for this study makes it a little harder to classify the variables, but with the periods and magnitudes found, we are quite certain that they are all RRL stars.

V25-V27, V30-V32: These stars all have periods, light curve shapes, and amplitudes typical of RR0 stars.

V29: The star given as V29 in R77 is not found to be variable. A star located 3″ away *is* found to be variable and we believe that this is the actual V29. Based on the period and magnitude, this star is classified as an RR1, despite the unusual asymmetric shape of the light curve.

V33: Based on the period, light curve shape, and magnitude, we classify this star as an RR1.

(a) Known variables
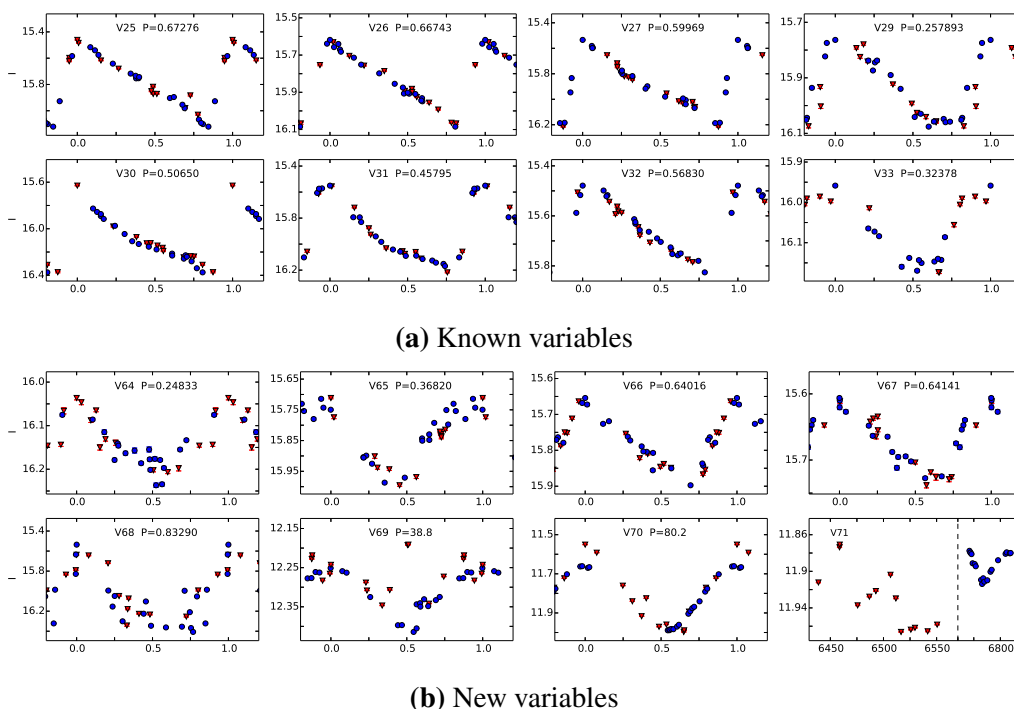

(b) New variables

Figure 5.17: NGC 6638: Light curves for the variables in our FoV. Red triangles are 2013 data and blue circles are 2014 data. Error bars are plotted but are smaller than the data symbols in many cases. Light curves with confirmed periods are phased. For those variables without periods the x-axis are in (HJD - 2450000), and the dashed line indicates that the period from HJD 2456600 to 2456750 has been removed from the plot, as no observations were performed during this time range.

Table 5.10: NGC 6638: Details of the 8 new variables found in the cluster.

Var	RA (J2000.0)	Dec. (J2000.0)	Epoch (d)	P (d)	$< I >$	$A_{i'+z'}$	Blend	Classification
V64	18:30:56.321	-25:30:03.74	6541.5840	0.24833	16.14	0.20	iii	RR1
V65	18:30:55.591	-25:29:43.63	6458.8425	0.36820	15.85	0.28	iii	RR1
V66	18:30:55.015	-25:29:47.10	6783.8751	0.64016	15.78	0.24	iii	RR0
V67	18:30:56.836	-25:29:46.75	6783.8751	0.64141	15.67	0.13	iii	RR0
V68	18:30:56.237	-25:30:04.37	6797.8372	0.83290	15.97	0.87	i	RR0
V69	18:30:54.834	-25:30:01.50	6516.5499	38.8	12.30	0.22	iii	SR
V70	18:30:55.820	-25:30:00.95	6486.7350	80.2	11.77	0.45	iii	SR
V71	18:30:56.005	-25:29:57.29	-	-	11.92	0.10	iii	L

Notes. The celestial coordinates correspond to the epoch of the reference image, which is the HJD ~2456511.65 d. Epochs are (HJD-2450000). $< I >$ denotes mean *I* magnitude and $A_{i'+z'}$ are the amplitudes found in our special $i' + z'$ filter. The blend column describes whether the star is blended with (i) brighter star(s), (ii) star(s) of similar magnitude, or (iii) fainter/no star(s).

5.2.4.3 New variables

In this study we were able to find eight new variable stars for NGC 6638. The lack of a CMD complicates the classification, but we classify five as RRL stars and three as long period variables. The light curves for these variables are shown in Fig. 5.17b and their details are listed in Table 5.10.

Especially interesting are the two variables V64 and V68, that are located very close to the same bright star (within $1''.2$ and $0''.8$, respectively). Using conventional imaging it would have been hard to distinguish these three stars from each other, but with the high resolution we achieve with the EMCCD camera this is possible.

V64, V65: Based on the period, light curve shape, and magnitude, these stars can be safely classified as RR1.

V66-V68: Three stars with periods and light curve shapes, that strongly indicate that they are RR0 stars.

V69: The period found for this SR phases the light curve reasonably well, but there are some outlier points, which might indicate that it is actually irregular.

V70: The light curve of this SR is phased well by the period.

V71: No period was found for this star, and it is therefore classified as an L star.

5.2.5 NGC 6652

5.2.5.1 Background information

Using 23 photographic plates taken with the 1m Yale telescope at CTIO in 1977, Hazen (1989) found 24 variable stars in this cluster. Nine variables (V1-9) were found within the tidal radius of the cluster, and 15 outside it. Two of the variables (V7 and V9) had already been published by Plaut (1971) as part of the Palomar-Groningen variable-star survey. None of these variable stars are close to the rather dense central part of the cluster nor do they lie within our FoV.

There are 12 known X-ray sources in NGC 6652 (Deutsch et al., 1998; Deutsch et al., 2000; Heinke et al., 2001; Coomber et al., 2011; Stacey et al., 2012; Engel et al., 2012). Sources A-C have been assigned variable numbers V10-V12, respectively, by C. Clement (private communication). Seven of the X-ray sources lie within our FoV (sources B-E and G-H). Only sources B and H show signs of variability in our difference images and for the remaining sources we cannot find any clear optical counterparts in our reference image at the positions given by

Coomber et al. (2011) and Stacey et al. (2012), although we note that our limiting magnitude is ~19.5 mag (see Fig. 5.20).

A finding chart for the cluster containing the variables detected in this study is shown in Fig. 5.18 and Fig. 5.19 shows a CMD of the stars within our FoV with the variables overplotted. Fig. 5.20 shows the RMS magnitude deviation for the 1098 stars with calibrated *I* magnitudes versus their mean magnitude. The light curves of the variables are plotted in Fig. 5.21 and their details may be found in Table 5.11.

5.2.5.2 Known variables

V11 (source B) was found by Coomber et al. (2011) to be undergoing rapid X-ray flaring on time-scales of less than 100 seconds. Like Engel et al. (2012), we have detected clear variability in the optical counterpart with an amplitude of up to ~1.1 mag (see Fig. 5.21). However, as in previous studies, we cannot find a period on which the light curve can be phased. Stacey et al. (2012) suggest that V11 might be a special type of low mass X-ray binary (LMXB) or a very faint X-ray transient (VFXT). One of the advantages of high frame-rate imaging is that it is possible to achieve a high time-resolution by combining the single exposures into short-exposure images. This technique could be applied to V11 to determine the time-scale of the optical flickering, but it is too faint to be able to do this with our data.

Table 5.11: NGC 6652: Details of the 1 known (V11) and 2 new (V13, V14) variables in our FoV.

Var	RA (J2000.0)	Dec. (J2000.0)	Epoch (*d*)	P (*d*)	< *I* >	$A_{i'+z'}$	Blend	Classification
V11	18:35:44.551	-32:59:38.38	-	-	18.72	1.09	iii	LMXB?, VFXT?[a]
V13	18:35:45.805	-32:59:35.94	-	-	14.17	0.04	iii	?
V14	18:35:46.325	-32:59:32.79	6506.6618	0.189845	17.74	0.29	iii	RR1?, EW?

Notes. The celestial coordinates correspond to the epoch of the reference image, which is the HJD ~2456458.84 d. Epochs are (HJD-2450000). < *I* > denotes mean *I* magnitude and $A_{i'+z'}$ are the amplitudes found in our special $i' + z'$ filter. The blend column describes whether the star is blended with (i) brighter star(s), (ii) star(s) of similar magnitude, or (iii) fainter/no star(s).   [a] Classification from Stacey et al. (2012)

5.2.5.3 New variables

We found two new variables in the cluster:

V13: This star has the same position as the X-ray source H, and we therefore assume that it is the same star. The star has a light curve scatter of less than
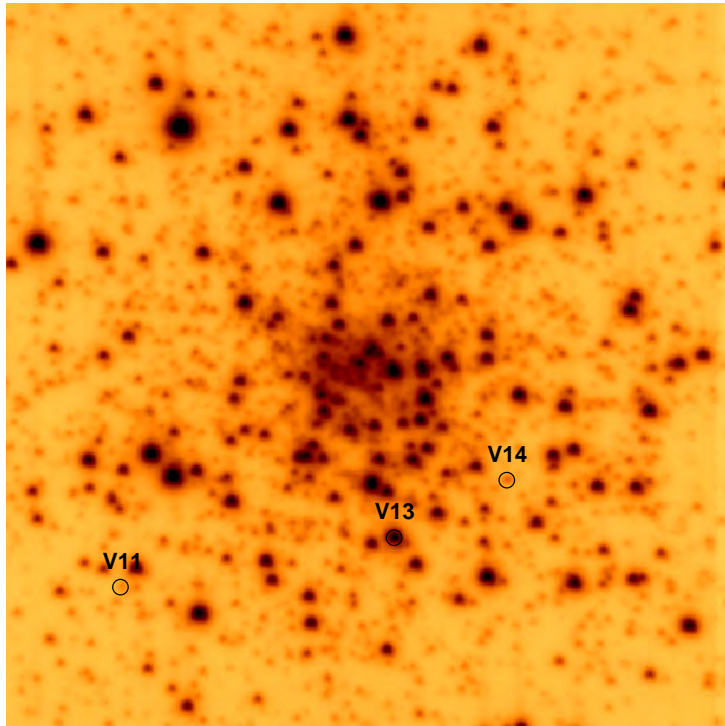
Figure 5.18: NGC 6652: Finding chart constructed from the reference image marking the positions of the variable stars. North is up and East is to the right. The cluster image is ~ 41″ by 41″.

~0.01 mag consistent with noise. However, at the epochs HJD 2456506 and 2456509 it is ~ 2 and 4% brighter than the base-line, suggesting that the star has undergone an outburst. However, the CMD puts the star on the RGB, where instead we might expect long period semi-regular variability, but this seems not to be the case for V13. We therefore refrain from classifying this variable.

V14: Based on its position in the CMD this star could be a blue-straggler eclipsing binary. The phased light curve looks like that of a RR1 star, but the period is too short for this. Furthermore, with its position ~2.5 magnitudes below the horizontal branch, it would be a field RR1 star lying behind the cluster.
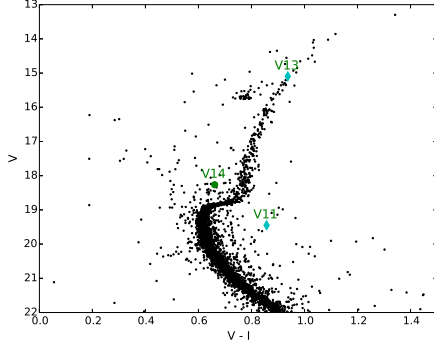
Figure 5.19: NGC 6652: $(V - I), V$ colour-magnitude diagram made from HST/ACS data as explained in Sect. 5.1.6. The three stars that show variability in our study are plotted. The two previously known X-ray sources are marked as cyan diamonds and the new found RR1 is marked with a green circle.
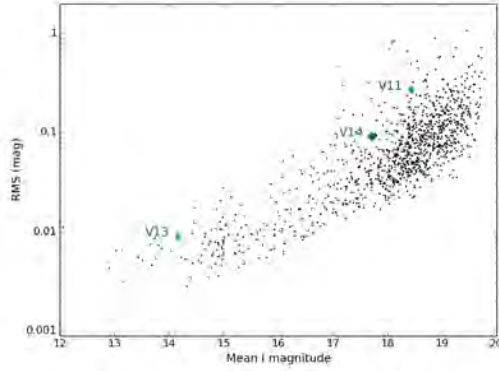
Figure 5.20: NGC 6652: Plot of the RMS magnitude deviation versus the mean magnitude for each of the 1098 calibrated I light curves. The variables are plotted with the same symbols as in Fig. 5.19.
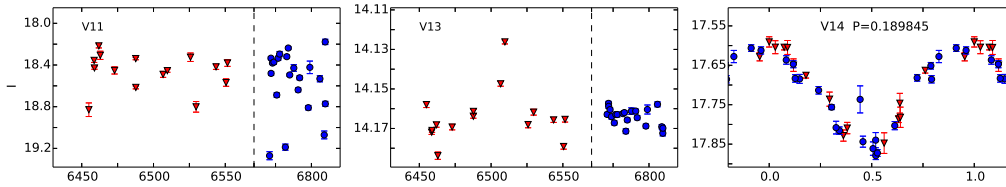

Figure 5.21: NGC 6652: Light curves for the variables in our FoV. Red triangles are 2013 data and blue circles are 2014 data. Error bars are plotted but are smaller than the data symbols in many cases. Light curves with confirmed periods are phased. For those variables without periods the x-axis refers to (HJD - 2450000), and the dashed line indicates that the period from HJD 2456570 to 2456760 has been removed from the plot, as no observations were performed during this time range.

5.3 Discussion

5.3.1 NGC 6388 and NGC 6441

Of the five clusters that we studied in this paper, NGC 6388 and NGC 6441 contain by far the largest number of variable stars. These two clusters have a very similar metallicity and central concentration (see Table 5.1) and very similar CMDs (see Fig. 5.3, 5.8). However, before the present study, NGC 6441 had twice as many

reported variables as NGC 6388.

We were able to find $\sim$ 50 new variables in each cluster, of which at least three are RRL stars and at least five are CW stars. The fact that we were able to find new short period variable stars in NGC 6441 is somewhat surprising given the fact that a HST snapshot study has been performed on this cluster. It should be noted that the HST data were analysed using the DAOPHOT/ALLSTAR/ALLFRAME routines (see Stetson, 1987; Stetson, 1994), which might not perform as well as DIA in such a crowded field.

The RR0 star V151 in NGC 6441 has a very large amplitude and the reason why this star has not been detected before is most likely due to its proximity to three other variable stars, which are all several magnitudes brighter. The fact that we are able to detect stars like this implies that there might be several other RRL stars situated close to bright stars outside our FoV that are not detected yet. Our method does, however, heighten the chances that we now have a complete census of the RRL stars in the central regions of NGC 6388 and NGC 6441.

With the newly found RRL stars there are now 23 RRL stars in NGC 6388 with robust classification (excluding V74 from our work), of which 11 are RR0 and 12 are RR1. Using these RRLs we calculate mean periods for the RR0 and RR1 stars as $< P_{RR0} >= 0.700$ d and $< P_{RR1} >= 0.389$ d, respectively, and the ratio of RR1s to the total number of RRLs as $\frac{n_{RR1}}{n_{RRL}} \approx 0.52$.

For NGC 6441 the total number of RRL stars with robust classification is now 69 (excluding V152 from our work), of which 45 are RR0, 23 are RR1, and 1 is RR01. From these we calculate $< P_{RR0} >= 0.745$ d, $< P_{RR1} >= 0.368$ d, and $\frac{n_{RR1}}{n_{RRL}} \approx 0.34$.

Oosterhoff (1939) called attention to a relation between the mean periods and relative proportions of RR0 and RR1 stars in GCs. Generally it is found that the RRLs in Oosterhoff type I (Oo I) clusters have shorter mean periods, and a lower ratio of RR1 stars, than in Oosterhoff type II (Oo II) clusters. It has also been found that Oo I clusters are usually more metal rich than Oo II clusters (Smith, 1995). NGC 6388 and NGC 6441 are therefore unusual as they do not fit into either of the Oo types. Their high metallicity indicates that they are Oo I, but the long mean periods of the RRLs and the high ratio of RR1 stars, especially for NGC 6388, indicates Oo II. Based on this Pritzl et al. (2000) suggested to create a new Osterhoff type III, but Clement et al. (2001) found that the period-amplitude relation of the RR0 variables in NGC 6441 is more consistent with that of Oo II. Our new variable star discoveries have not changed the Oo classification situation for these clusters.

Period-luminosity diagrams for the CW and RV stars that are found in the two clusters are shown in Fig. 5.22. In P03 the relation between the absolute I magnitudes (I_{abs}) of the CW stars and their periods is found to be $I_{abs} \propto -2.03 \cdot \log_{10}(P)$. The relation is actually only based on CW stars from NGC 6441, but we have
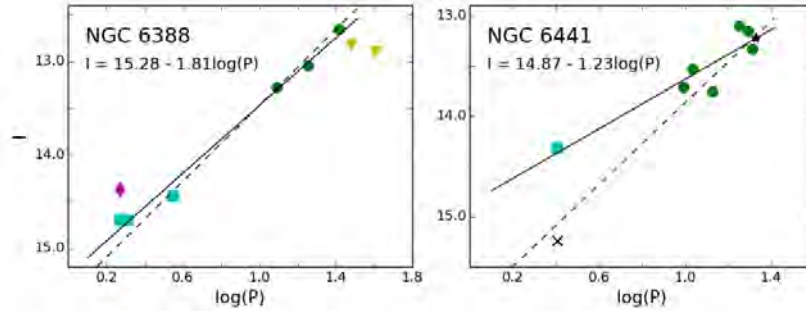
Figure 5.22: Plot of periods against *I* magnitudes for the CWs and RVs found in NGC 6388 and NGC 6441. Green circles are CWAs, cyan squares are CWBs, yellow triangles are RVs, and magenta diamonds are ACs. The black star and black cross in the NGC 6441 plot are the variable stars V6 and V132, respectively, for which mean *I* magnitudes and periods are taken from P03. The solid lines are derived based on CWAs and CWBs from this study only and have R^2-values of 0.991 and 0.848 for NGC 6388 and NGC 6441, respectively. The dashed lines are the relations found in P03 (see Sect. 5.3.1 for details).

plotted it for both clusters in Fig. 5.22 (dashed line) using the relation $I = I_0 - 2.03 \cdot \log_{10}(P)$, where I_0 is 15.5 and 15.9 mag for NGC 6388 and NGC 6441, respectively.

For NGC 6388, there are three CWs, (V29, V63, and V77) with periods below 3 days. V29 and V63 have been classified as CWB, while V77 has been classified as an AC due to the fact that it is a little too bright for its period compared with the other two (Clement et al., 2001). The two stars with periods over 30 days are the RV stars V80, and V82. RV stars also exhibit a correlation between their luminosity and periods, but with a larger intrinsic scatter than the CW stars, which is also evident for NGC 6388. We find a relation of $I \propto 1.81 \cdot \log_{10}(P)$ for NGC 6388, which is close to the relation found in P03.

In the P03 analysis of NGC 6441 there is one CWA star that is not included in this study. The star, V6, is classified as P2C in P03 and is included in the NGC 6441 plot in Fig. 5.22. The CWB star V132 is heavily blended and this is probably the reason why the pipeline has measured the star to be a magnitude brighter than in P03. Using our *I* magnitude for V132, we find the relation $I \propto 1.23 \cdot \log_{10}(P)$, which is quite far from the P03 relation. However, by using the *I* magnitude from P03 for V132 (plotted as a black cross in Fig. 5.22), the relation found in P03 looks much more feasible.

Most of the new variables found in the two clusters are RGB stars, which is not surprising due to a number of factors:

- The CMDs of the two clusters show a very prominent RGB, on which most

stars are intrinsically variable (e.g. Percy, 2007; Percy et al., 2014).

- The baseline of our data is about 14 months, which makes it possible to detect variability over a long period.

- The filter we use goes from the optical red to near-infrared wavelengths, which matches very well with the color of the RGB stars.

- The use of high frame-rate imaging makes it possible to observe much brighter stars without saturating.

Both the SR and L classifications have several subclasses, but in order to safely assign these, one would need more information on the stars, such as spectral type and a longer baseline than is available in this study.

5.3.2 NGC 6638

Of the 21 variable stars in R77 where a period has been determined, one (V24) has a period consistent with that of an RR0, and 14 with RR1 periods. Two of the RR1s (V40 and V42) are located very far from the centre and might not be cluster members. We find that a further eight of the known variables (those in Table 5.4) have periods consistent with RRLs and we also retrieve five new RRL stars (Table 5.5).

The total number of RRL stars in the cluster is therefore between 26 and 28, of which 10 are RR0 and 16-18 are RR1. The mean periods have been calculated as $< P_{RR0} >= 0.625$ d and $< P_{RR1} >= 0.305$ d excluding V40 and V42, and including them only changes this by less than 0.001 d. The ratio of RR1s to total number of RRLs is between 0.62 and 0.64, depending on the inclusion or exclusion of V40 and V42.

Fig. 5.23 shows a Bailey diagram, i.e. a plot of the period versus the amplitude for RR Lyrae stars, for NGC 6638. The black lines in this plot are the loci calculated by Kunder et al. (2013) for the Oo I clusters for the RR0 and RR1 stars (solid lines) and for the Oo II clusters (dashed lines). The dotted blue line is the locus found by Arellano Ferro et al. (2011) and Arellano Ferro et al. (2013a) for the two Oo II clusters NGC 5024 and NGC 6333, respectively. Both sets of loci are derived from the *I*-band light curves and as our $i' + z'$ filter is slightly redder, our amplitudes might also be a little smaller than true *I*-band amplitudes. Even with slightly larger amplitudes than what is plotted in Fig. 5.23, the RRL stars seem to follow the loci for Oo I clusters. There are a number of RR0 stars that lie somewhat higher than the rest, and these are probably more evolved stars, following the argumentation in Clement et al. (1997) and Cacciari et al. (2005).
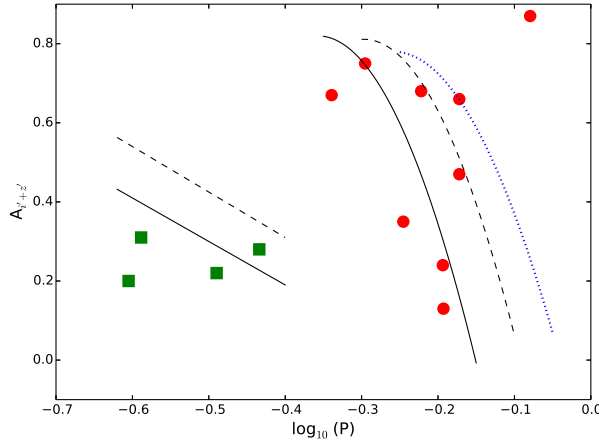
Figure 5.23: Bailey diagram of NGC 6638 for *I* amplitudes, with RR0 and RR1 stars plotted as red circles and green squares, respectively. The black solid and dashed lines are the Oo I and Oo II loci, respectively, as calculated by Kunder et al. (2013) for *I*-band. The blue dotted line is the locus found by Arellano Ferro et al. (2011) and Arellano Ferro et al. (2013a) for the two Oo II clusters NGC 5024 and NGC 6333, respectively.

Based on the Bailey diagram and the metallicity of the cluster, [Fe/H] $\simeq -0.95$, we tentatively classify NGC 6638 as an Oo I cluster, despite the high $\frac{n_{RR1}}{n_{RRL}}$ ratio.

Two of the newly found RRLs (V64 and V68) are found very close to the same bright star, and this is a very clear example of the advantages of the EMCCD data, as these would have been very hard to resolve using conventional imaging. It also makes it more likely that we now have a complete census of the RRLs in the central parts of this cluster, especially as this cluster does not have a very dense central region (see Table 5.1).

A CMD of NGC 6638 has been published by Piotto et al. (2002), and from this it is evident that the RGB of this cluster is much less prominent than the ones of NGC 6388 and NGC 6441. It is therefore not surprising that only very few variable RGB stars are found in this cluster.

5.3.3 NGC 6528 and NGC 6652

NGC 6528 and NGC 6652 have significantly different metallicities, but they share their lack of variable stars.

Until now no variable stars had been reported for NGC 6528, but we were able to find two RRLs and four long period RGB stars, plus a very faint variable star that could not be classified.

Of the three variable stars we find in NGC 6652, two seem to be optical counter-

parts of X-ray sources, and the third might be a blue-straggler eclipsing binary, or a field RR1 lying behind the cluster.

The CMDs of the two clusters (a CMD of NGC 6528 can be found in Feltzing et al. (2002)) correlate well with the number of variables found. Both clusters have very few stars in the instability strip of the horizontal branch. NGC 6652 has very few stars on the RGB, while the RGB of NGC 6528 is comparable to that of NGC 6388.

5.4 Conclusions

A detailed variability study of 5 metal rich ([Fe/H] > -1) globular clusters; NGC 6388, NGC 6441, NGC 6528, NGC 6638, and NGC 6652; has been performed, by using EMCCD observations with DIA. All previously known variable stars located within our field of view in each of the 5 clusters have been recovered and classified, and numerous previously unknown variables have been discovered. For three of the clusters; NGC 6388, NGC 6441, and NGC 6652; electronically available CMD data from a HST survey have helped in the classification of the variable stars. For the two remaining clusters CMDs exist in the literature. Common for all of the clusters is that the CMDs seem to be in agreement with the number and types of variable stars we have found.

Chapter 6

Conclusion

In this thesis I have detailed the Two-Colour EMCCD Instrument designed for the SONG 1m telescopes and the Danish 1.54m telescope, and described my contribution to its design, construction, tests, and pipeline and reduction software development. Using the software system written for this instrument, the TCI is the first routinely operated multi-color instrument providing Lucky Imaging photometry.

A performance analysis of the instrument on the Danish 1.54m telescope shows that the PSF width can be improved with up to a factor of two by doing Lucky Imaging compared to conventional imaging. There are, however, a wide spread in these numbers, and the mean values range from a 35% improvement at a 1% selection to a 20% improvement at a 100% selection. For the low selection percentages we see that the FWHM for up to a fourth of the exposures have not improved significantly, or in some cases actually even gotten worse, compared to conventional CCD imaging. One possible explanation for this could be that the 10 Hz frame-rate, that is used as default at the DK154, is not high enough in some weather conditions, for instance during high winds. However, to fully understand this issue, one would need to do a thorough analysis of the affected frames and the reduction algorithms currently used.

Despite the imperfections in the DK154 optics, I find that spatial resolutions below $0\rlap{.}''4$ are reached on a regular basis. Due to the near-diffraction limited optics on the SONG telescope, it is expected that the TCI will be able to reach $0\rlap{.}''2$, as preliminary test has shown resolutions down to $0\rlap{.}''25$. This is quite close to the sampling limit of the instrument, and it might therefore be necessary to introduce sub-pixel shifts and dithering methods into the current Fast Fourier Transform (FFT) algorithm to further increase the spatial resolution.

It might also be advantage to test other algorithms for reducing the EMCCD data, than the FFT algorithm currently used. This could provide more insight into the

advantages and pitfalls of the current analysis routines and might therefore help to improve the performance and the stability of the reduced EMCCD data.

It is shown that the TCI can give a high-precision photometric output. The photometric scatter measured on EMCCD data for a transiting planet is thus only slightly higher than what one would have gotten with a conventional CCD using the ultra-precise defocussed observation method. The results from the Chariklo observation show that even photometry on the single $0.1\,\mathrm{s}$ exposures is possible, and these observations demonstrated an unexpected additional power of high frame-rate observing by revealing a ring-system around an asteroid-like object – the first known of its kind.

The power of difference imaging analysis of EMCCD data, especially using the `DanDIA` pipeline, has also been shown. The modifications I have made to `DanDIA` enables us to create a high-resolution reference frame from the best percentage exposures. With this reference frame, `DanDIA` can be used to extract the photometry from other observations, such that we are able to preserve the total number of photons, thus achieving the highest possible S/N, while still keeping the high spatial resolution of the best few percentage images.

The method has been used to do high-precision time-series photometry of very dense stellar fields, such as microlensing events in Baades window and variability studies of the stars in cores of dense globular clusters.

The first results from the search for variable stars in globular clusters have shown that large scale EMCCD observing campaigns in crowded stellar fields using the TCI are feasible and that we are able to reveal new variable stars in otherwise well-studied globular clusters.

List of publications

Refereed articles

Arellano Ferro, A., D. M. Bramich, R. Figuera Jaimes, S. Giridhar, N. Kains, K. Kuppuswamy, U. G. Jørgensen, et al. (2013a). "A detailed census of variable stars in the globular cluster NGC 6333 (M9) from CCD differential photometry". In: *MNRAS* 434, pp. 1220–1238. DOI: `10.1093/mnras/stt1080`. arXiv: `1306.3206` [`astro-ph.SR`] (cit. on pp. 85, 86).

Bachelet, E., P. Fouqué, C. Han, A. Gould, M. D. Albrow, J.-P. Beaulieu, E. Bertin, et al. (2012). "A brown dwarf orbiting an M-dwarf: MOA 2009-BLG-411L". In: *A&A* 547, A55, A55. DOI: `10.1051/0004-6361/201219765`.

Batista, V., A. Gould, S. Dieters, S. Dong, I. Bond, J. P. Beaulieu, D. Maoz, et al. (2011). "MOA-2009-BLG-387Lb: a massive planet orbiting an M dwarf". In: *A&A* 529, A102, A102. DOI: `10.1051/0004-6361/201016111`. arXiv: `1102.0558` [`astro-ph.EP`].

Braga-Ribas, F., B. Sicardy, J. L. Ortiz, C. Snodgrass, F. Roques, R. Vieira-Martins, J. I. B. Camargo, et al. (2014). "A ring system detected around the Centaur (10199) Chariklo". In: *Nature* 508, pp. 72–75. DOI: `10.1038/nature13155`. arXiv: `1409.7259` [`astro-ph.EP`] (cit. on pp. 4, 38).

Bryan, M. L., K. A. Alsubai, D. W. Latham, N. R. Parley, A. Collier Cameron, S. N. Quinn, J. A. Carter, et al. (2012). "Qatar-2: A K Dwarf Orbited by a Transiting Hot Jupiter and a More Massive Companion in an Outer Orbit". In: *ApJ* 750, 84, p. 84. DOI: `10.1088/0004-637X/750/1/84`. arXiv: `1110.5912` [`astro-ph.EP`].

Choi, J.-Y., C. Han, A. Udalski, T. Sumi, B. S. Gaudi, A. Gould, D. P. Bennett, et al. (2013). "Microlensing Discovery of a Population of Very Tight, Very Low Mass Binary Brown Dwarfs". In: *ApJ* 768, 129, p. 129. DOI: `10.1088/0004-637X/768/2/129`. arXiv: `1302.4169` [`astro-ph.SR`].

Choi, J.-Y., I.-G. Shin, C. Han, A. Udalski, T. Sumi, A. Gould, V. Bozza, et al. (2012a). "A New Type of Ambiguity in the Planet and Binary Interpretations of Central Perturbations of High-magnification Gravitational Microlensing Events". In: *ApJ* 756, 48, p. 48. DOI: `10.1088/0004-637X/756/1/48`. arXiv: `1204.4789` [`astro-ph.EP`].

Choi, J.-Y., I.-G. Shin, S.-Y. Park, C. Han, A. Gould, T. Sumi, A. Udalski, et al. (2012b). "Characterizing Lenses and Lensed Stars of High-magnification Single-lens Gravita-

tional Microlensing Events with Lenses Passing over Source Stars". In: *ApJ* 751, 41, p. 41. DOI: 10.1088/0004-637X/751/1/41. arXiv: 1111.4032 [astro-ph.SR].

Harpsøe, K. B. W., S. Hardis, T. C. Hinse, U. G. Jørgensen, L. Mancini, J. Southworth, K. A. Alsubai, et al. (2013). "The transiting system GJ1214: high-precision defocused transit observations and a search for evidence of transit timing variation". In: *A&A* 549, A10, A10. DOI: 10.1051/0004-6361/201219996. arXiv: 1207.3064 [astro-ph.EP].

Kains, N., D. M. Bramich, A. Arellano Ferro, R. Figuera Jaimes, U. G. Jørgensen, S. Giridhar, M. T. Penny, et al. (2013a). "Estimating the parameters of globular cluster M 30 (NGC 7099) from time-series photometry". In: *A&A* 555, A36, A36. DOI: 10.1051/0004-6361/201321819. arXiv: 1305.3606 [astro-ph.SR] (cit. on p. 47).

Kains, N., R. A. Street, J.-Y. Choi, C. Han, A. Udalski, L. A. Almeida, F. Jablonski, et al. (2013b). "A giant planet beyond the snow line in microlensing event OGLE-2011-BLG-0251". In: *A&A* 552, A70, A70. DOI: 10.1051/0004-6361/201220626. arXiv: 1303.1184 [astro-ph.EP].

Leloudas, G., M. D. Stritzinger, J. Sollerman, C. R. Burns, C. Kozma, K. Krisciunas, J. R. Maund, et al. (2009). "The normal Type Ia SN 2003hv out to very late phases". In: *A&A* 505, pp. 265–279. DOI: 10.1051/0004-6361/200912364. arXiv: 0908.0537 [astro-ph.SR].

Mancini, L., S. Ciceri, G. Chen, J. Tregloan-Reed, J. J. Fortney, J. Southworth, T. G. Tan, et al. (2013). "Physical properties, transmission and emission spectra of the WASP-19 planetary system from multi-colour photometry". In: *MNRAS* 436, pp. 2–18. DOI: 10.1093/mnras/stt1394. arXiv: 1306.6384 [astro-ph.EP].

Mancini, L., J. Southworth, S. Ciceri, S. Calchi Novati, M. Dominik, T. Henning, U. G. Jørgensen, et al. (2014a). "Physical properties of the WASP-67 planetary system from multi-colour photometry". In: *A&A* 568, A127, A127. DOI: 10.1051/0004-6361/201424106. arXiv: 1406.7448 [astro-ph.EP] (cit. on p. 39).

Mancini, L., J. Southworth, S. Ciceri, M. Dominik, T. Henning, U. G. Jørgensen, A. F. Lanza, et al. (2014b). "Physical properties and transmission spectrum of the WASP-80 planetary system from multi-colour photometry". In: *A&A* 562, A126, A126. DOI: 10.1051/0004-6361/201323265. arXiv: 1312.4982 [astro-ph.EP].

Miyake, N., T. Sumi, S. Dong, R. Street, L. Mancini, A. Gould, D. P. Bennett, et al. (2011). "A Sub-Saturn Mass Planet, MOA-2009-BLG-319Lb". In: *ApJ* 728, 120, p. 120. DOI: 10.1088/0004-637X/728/2/120. arXiv: 1010.1809 [astro-ph.EP].

Muraki, Y., C. Han, D. P. Bennett, D. Suzuki, L. A. G. Monard, R. Street, U. G. Jorgensen, et al. (2011). "Discovery and Mass Measurements of a Cold, 10 Earth Mass Planet and Its Host Star". In: *ApJ* 741, 22, p. 22. DOI: 10.1088/0004-637X/741/1/22. arXiv: 1106.2160 [astro-ph.EP].

Ricci, D., A. Elyiv, F. Finet, O. Wertz, K. Alsubai, T. Anguita, V. Bozza, et al. (2013). "Flux and color variations of the doubly imaged quasar UM673". In: *A&A* 551, A104, A104. DOI: 10.1051/0004-6361/201118755. arXiv: 1302.0766 [astro-ph.CO].

Ricci, D., J. Poels, A. Elyiv, F. Finet, P. G. Sprimont, T. Anguita, V. Bozza, et al. (2011). "Flux and color variations of the quadruply imaged quasar HE 0435-1223". In: *A&A*

528, A42, A42. DOI: 10.1051/0004-6361/201016188. arXiv: 1101.3664 [astro-ph.CO].

Ryu, Y.-H., C. Han, K.-H. Hwang, R. Street, A. Udalski, T. Sumi, A. Fukui, et al. (2010). "OGLE-2009-BLG-092/MOA-2009-BLG-137: A Dramatic Repeating Event with the Second Perturbation Predicted by Real-time Analysis". In: *ApJ* 723, pp. 81–88. DOI: 10.1088/0004-637X/723/1/81. arXiv: 1009.0338 [astro-ph.SR].

Shin, I.-G., J.-Y. Choi, S.-Y. Park, C. Han, A. Gould, T. Sumi, A. Udalski, et al. (2012a). "Microlensing Binaries Discovered through High-magnification Channel". In: *ApJ* 746, 127, p. 127. DOI: 10.1088/0004-637X/746/2/127. arXiv: 1109.3295 [astro-ph.SR].

Shin, I.-G., C. Han, J.-Y. Choi, A. Udalski, T. Sumi, A. Gould, V. Bozza, et al. (2012b). "Characterizing Low-mass Binaries from Observation of Long-timescale Caustic-crossing Gravitational Microlensing Events". In: *ApJ* 755, 91, p. 91. DOI: 10.1088/0004-637X/755/2/91. arXiv: 1204.2869 [astro-ph.SR].

Shin, I.-G., C. Han, A. Gould, A. Udalski, T. Sumi, M. Dominik, J.-P. Beaulieu, et al. (2012c). "Microlensing Binaries with Candidate Brown Dwarf Companions". In: *ApJ* 760, 116, p. 116. DOI: 10.1088/0004-637X/760/2/116. arXiv: 1208.2323 [astro-ph.SR].

Skottfelt, J., D. M. Bramich, R. Figuera Jaimes, U. G. Jørgensen, N. Kains, A. Arrellano Ferro, K. A. Alsubai, et al. (2014a). "Searching for variable stars in the cores of five metal rich globular clusters using EMCCD observations". In: *Accepted to A&A*. arXiv: 1410.8827 [astro-ph.SR] (cit. on pp. 4, 32, 37).

Skottfelt, J., D. M. Bramich, R. Figuera Jaimes, U. G. Jørgensen, N. Kains, K. B. W. Harpsøe, C. Liebig, et al. (2013b). "EMCCD photometry reveals two new variable stars in the crowded central region of the globular cluster NGC 6981". In: *A&A* 553, A111, A111. DOI: 10.1051/0004-6361/201321430. arXiv: 1304.2243 [astro-ph.SR] (cit. on pp. 4, 32, 37, 47, 48).

Southworth, J., T. C. Hinse, M. Burgdorf, S. Calchi Novati, M. Dominik, P. Galianni, T. Gerner, et al. (2014). "High-precision photometry by telescope defocussing - VI. WASP-24, WASP-25 and WASP-26". In: *MNRAS* 444, pp. 776–789. DOI: 10.1093/mnras/stu1492. arXiv: 1407.6253 [astro-ph.EP] (cit. on p. 39).

Southworth, J., T. C. Hinse, M. Dominik, X.-S. Fang, K. Harpsøe, U. G. Jørgensen, E. Kerins, et al. (2012). "High-precision photometry by telescope defocusing - IV. Confirmation of the huge radius of WASP-17 b". In: *MNRAS* 426, pp. 1338–1348. DOI: 10.1111/j.1365-2966.2012.21781.x. arXiv: 1207.5797 [astro-ph.EP].

Southworth, J., T. C. Hinse, M. Dominik, M. Glitrup, U. G. Jørgensen, C. Liebig, M. Mathiasen, et al. (2009a). "Physical Properties of the 0.94-Day Period Transiting Planetary System WASP-18". In: *ApJ* 707, 167, pp. 167–172. DOI: 10.1088/0004-637X/707/1/167. arXiv: 0910.4875 [astro-ph.EP].

Southworth, J., L. Mancini, P. Browne, M. Burgdorf, S. Calchi Novati, M. Dominik, T. Gerner, et al. (2013). "High-precision photometry by telescope defocusing - V. WASP-15 and WASP-16". In: *MNRAS* 434, pp. 1300–1308. DOI: 10.1093/mnras/stt1089. arXiv: 1306.3509 [astro-ph.EP].

Southworth, J., L. Mancini, S. C. Novati, M. Dominik, M. Glitrup, T. C. Hinse, U. G. Jørgensen, et al. (2010). "High-precision photometry by telescope defocusing - III. The transiting planetary system WASP-2". In: *MNRAS* 408, pp. 1680–1688. DOI: 10.1111/j.1365-2966.2010.17238.x. arXiv: 1006.4464 [astro-ph.EP] (cit. on p. 39).

Tsapras, Y., J.-Y. Choi, R. A. Street, C. Han, V. Bozza, A. Gould, M. Dominik, et al. (2014). "A Super-Jupiter Orbiting a Late-type Star: A Refined Analysis of Microlensing Event OGLE-2012-BLG-0406". In: *ApJ* 782, 48, p. 48. DOI: 10.1088/0004-637X/782/1/48. arXiv: 1310.2428 [astro-ph.EP] (cit. on p. 4).

Other

Dominik, M., U. G. Jørgensen, F. V. Hessman, K. Horne, K. Harpsøe, J. Skottfelt, and MiNDSTEp Consortium (2011). "Exploring Hitherto Uncharted Planet Territory with Lucky-imaging Microlensing Observations". In: *AAS/Division for Extreme Solar Systems Abstracts*. Vol. 2. AAS/Division for Extreme Solar Systems Abstracts, p. 2101.

Grundahl, F., J. Christensen-Dalsgaard, P. L. Pallé, M. F. Andersen, S. Frandsen, K. Harpsøe, U. G. Jørgensen, et al. (2014). "Stellar Observations Network Group: The prototype is nearly ready". In: *IAU Symposium*. Ed. by J. A. Guzik, W. J. Chaplin, G. Handler, and A. Pigulski. Vol. 301. IAU Symposium, pp. 69–75. DOI: 10.1017/S1743921313014117 (cit. on p. 10).

Kains, N., D. M. Bramich, R. F. Jaimes, and J. Skottfelt (2014). "LIMBO: A time-series Lucky Imaging survey of variability in Galactic globular clusters". In: *IAU Symposium*. Ed. by J. A. Guzik, W. J. Chaplin, G. Handler, and A. Pigulski. Vol. 301. IAU Symposium, pp. 435–436. DOI: 10.1017/S1743921313014920 (cit. on p. 37).

Pallé, P. L., F. Grundahl, A. Triviño Hage, J. Christensen-Dalsgaard, S. Frandsen, R. A. García, K. Uytterhoeven, et al. (2013). "Observations of the radial velocity of the Sun as measured with the novel SONG spectrograph: results from a 1-week campaign". In: *Journal of Physics Conference Series* 440.1, 012051, p. 012051. DOI: 10.1088/1742-6596/440/1/012051.

Skottfelt, J., D. M. Bramich, R. Figuera Jaimes, U. G. Jorgensen, N. Kains, K. B. W. Harpsoe, C. Liebig, et al. (2013a). "VizieR Online Data Catalog: Light curves of two NGC6981 variables (Skottfelt+, 2013)". In: *VizieR Online Data Catalog* 355, p. 39111.

Skottfelt, J., D. M. Bramich, M. Hundertmark, U. G. Jørgensen, P. Kjærgaard, N. Michaelsen, J. Southworth, et al. (2014b). "(The Two-Colour EMCCD Instrument for the Danish 1.54m Telescope and SONG)". In: *Submitted on 01/11/2014 to A&A*.

Smith, A. M. S. and WASP Consortium (2014). "The SuperWASP exoplanet transit survey". In: *Contributions of the Astronomical Observatory Skalnate Pleso* 43, pp. 500–512.

Uytterhoeven, K., P. L. Palle, F. Grundahl, S. Frandsen, H. Kjeldsen, J. Christensen-Dalsgaard, M. Fredslund Andersen, et al. (2011). "The SONG project and the prototype node at Tenerife". In: *ArXiv e-prints*. arXiv: `1111.1834 [astro-ph.IM]`.

References

Alard, C. (2000). "Image subtraction using a space-varying kernel". In: *A&AS* 144, pp. 363–370. DOI: `10.1051/aas:2000214` (cit. on p. 56).

Alard, C. and R. H. Lupton (1998). "A Method for Optimal Image Subtraction". In: *ApJ* 503, p. 325. DOI: `10.1086/305984`. eprint: `astro-ph/9712287` (cit. on pp. 42, 56).

Albrow, M. D., K. Horne, D. M. Bramich, P. Fouqué, V. R. Miller, J.-P. Beaulieu, C. Coutures, et al. (2009). "Difference imaging photometry of blended gravitational microlensing events with a numerical kernel". In: *MNRAS* 397, pp. 2099–2105. DOI: `10.1111/j.1365-2966.2009.15098.x`. arXiv: `0905.3003 [astro-ph.SR]` (cit. on pp. 32, 42).

Alcock, C., R. A. Allsman, D. R. Alves, T. S. Axelrod, A. C. Becker, D. P. Bennett, K. H. Cook, et al. (2000). "The MACHO Project: Microlensing Results from 5.7 Years of Large Magellanic Cloud Observations". In: *ApJ* 542, pp. 281–307. DOI: `10.1086/309512`. eprint: `astro-ph/0001272` (cit. on p. 55).

Allen, C. W. (1973). *Astrophysical quantities*. London: University of London, Athlone Press, |c1973, 3rd ed. (cit. on p. 15).

Alted, Francesc, Ivan Vilata, et al. (2002-2014). *PyTables: Hierarchical Datasets in Python*. URL: `http://www.pytables.org/` (cit. on p. 20).

Amigo, P., P. B. Stetson, M. Catelan, M. Zoccali, and H. A. Smith (2013). "Time-series BVI Photometry for the Globular Cluster NGC 6981". In: *AJ* 146, 130, p. 130. DOI: `10.1088/0004-6256/146/5/130`. arXiv: `1308.6584 [astro-ph.GA]` (cit. on p. 37).

Andersen, J., M. I. Andersen, J. Klougart, P. Knudsen, H. H. Larsen, N. Michaelsen, R. F. Nielsen, et al. (1995). "New power for the Danish 1.54-m telescope." In: *The Messenger* 79, pp. 12–14 (cit. on p. 9).

Arellano Ferro, A., D. M. Bramich, R. Figuera Jaimes, S. Giridhar, N. Kains, K. Kuppuswamy, U. G. Jørgensen, et al. (2013a). "A detailed census of variable stars in the globular cluster NGC 6333 (M9) from CCD differential photometry". In: *MNRAS* 434, pp. 1220–1238. DOI: `10.1093/mnras/stt1080`. arXiv: `1306.3206 [astro-ph.SR]` (cit. on pp. 85, 86).

Arellano Ferro, A., D. M. Bramich, S. Giridhar, R. Figuera Jaimes, N. Kains, and K. Kuppuswamy (2013b). "Variable Stars in the Globular Cluster NGC 288: [Fe/H] and Distance". In: *Acta Astron.* 63, pp. 429–451. arXiv: `1401.5476 [astro-ph.SR]` (cit. on p. 47).

Arellano Ferro, A., R. Figuera Jaimes, S. Giridhar, D. M. Bramich, J. V. Hernández Santisteban, and K. Kuppuswamy (2011). "Exploring the variable stars in the globular cluster NGC 5024 (M53): new RR Lyrae and SX Phoenicis stars". In: *MNRAS* 416, pp. 2265–2284. DOI: 10.1111/j.1365-2966.2011.19201.x. arXiv: 1106.1880 [astro-ph.SR] (cit. on pp. 85, 86).

Bachelet, E., P. Fouqué, C. Han, A. Gould, M. D. Albrow, J.-P. Beaulieu, E. Bertin, et al. (2012). "A brown dwarf orbiting an M-dwarf: MOA 2009-BLG-411L". In: *A&A* 547, A55, A55. DOI: 10.1051/0004-6361/201219765.

Bahcall, J. N. and R. M. Soneira (1980). "The universe at faint magnitudes. I - Models for the galaxy and the predicted star counts". In: *ApJS* 44, pp. 73–110. DOI: 10.1086/190685 (cit. on p. 15).

Basden, A. G. and C. A. Haniff (2004). "Low light level CCDs and visibility parameter estimation". In: *MNRAS* 347, pp. 1187–1197. DOI: 10.1111/j.1365-2966.2004.07283.x. eprint: astro-ph/0310407 (cit. on p. 5).

Batista, V., A. Gould, S. Dieters, S. Dong, I. Bond, J. P. Beaulieu, D. Maoz, et al. (2011). "MOA-2009-BLG-387Lb: a massive planet orbiting an M dwarf". In: *A&A* 529, A102, A102. DOI: 10.1051/0004-6361/201016111. arXiv: 1102.0558 [astro-ph.EP].

Beers, T. C., K. Flynn, and K. Gebhardt (1990). "Measures of location and scale for velocities in clusters of galaxies - A robust approach". In: *AJ* 100, pp. 32–46. DOI: 10.1086/115487 (cit. on p. 29).

Bennett, D. P. and S. H. Rhie (2002). "Simulation of a Space-based Microlensing Survey for Terrestrial Extrasolar Planets". In: *ApJ* 574, pp. 985–1003. DOI: 10.1086/340977. eprint: astro-ph/0011466 (cit. on pp. 2, 37).

Bessell, M. S. (1990). "UBVRI passbands". In: *PASP* 102, pp. 1181–1199. DOI: 10.1086/132749 (cit. on p. 12).

Bessell, Michael S. (2005). "STANDARD PHOTOMETRIC SYSTEMS". In: *Annual Review of Astronomy and Astrophysics* 43.1, pp. 293–336. DOI: 10.1146/annurev.astro.41.082801.100251. eprint: http://www.annualreviews.org/doi/pdf/10.1146/annurev.astro.41.082801.100251 (cit. on pp. 43, 49).

Birkby, J. L., M. Cappetta, P. Cruz, J. Koppenhoefer, O. Ivanyuk, A. J. Mustill, S. T. Hodgkin, et al. (2014). "WTS-2 b: a hot Jupiter orbiting near its tidal destruction radius around a K dwarf". In: *MNRAS* 440, pp. 1470–1489. DOI: 10.1093/mnras/stu343. arXiv: 1402.5416 [astro-ph.EP] (cit. on p. 30).

Braga-Ribas, F., B. Sicardy, J. L. Ortiz, C. Snodgrass, F. Roques, R. Vieira-Martins, J. I. B. Camargo, et al. (2014). "A ring system detected around the Centaur (10199) Chariklo". In: *Nature* 508, pp. 72–75. DOI: 10.1038/nature13155. arXiv: 1409.7259 [astro-ph.EP] (cit. on pp. 4, 38).

Bramich, D. M. (2008). "A new algorithm for difference image analysis". In: *MNRAS* 386, pp. L77–L81. DOI: 10.1111/j.1745-3933.2008.00464.x. arXiv: 0802.1273 (cit. on pp. 32, 42, 43, 50).

Bramich, D. M., R. Figuera Jaimes, S. Giridhar, and A. Arellano Ferro (2011). "CCD time-series photometry of the globular cluster NGC 6981: variable star census and

physical parameter estimates". In: *MNRAS* 413, pp. 1275–1294. DOI: 10.1111/j.1365-2966.2011.18213.x. arXiv: 1012.5652 [astro-ph.SR] (cit. on pp. 32, 37, 41, 47, 51).

Bramich, D. M., K. Horne, M. D. Albrow, Y. Tsapras, C. Snodgrass, R. A. Street, M. Hundertmark, et al. (2013). "Difference image analysis: extension to a spatially varying photometric scale factor and other considerations". In: *MNRAS* 428, pp. 2275–2289. DOI: 10.1093/mnras/sts184. arXiv: 1210.2926 [astro-ph.IM] (cit. on pp. 32, 42, 43, 50).

Bryan, M. L., K. A. Alsubai, D. W. Latham, N. R. Parley, A. Collier Cameron, S. N. Quinn, J. A. Carter, et al. (2012). "Qatar-2: A K Dwarf Orbited by a Transiting Hot Jupiter and a More Massive Companion in an Outer Orbit". In: *ApJ* 750, 84, p. 84. DOI: 10.1088/0004-637X/750/1/84. arXiv: 1110.5912 [astro-ph.EP].

Cacciari, C., T. M. Corwin, and B. W. Carney (2005). "A Multicolor and Fourier Study of RR Lyrae Variables in the Globular Cluster NGC 5272 (M3)". In: *AJ* 129, pp. 267–302. DOI: 10.1086/426325. eprint: astro-ph/0409567 (cit. on p. 85).

Calamida, A., G. Bono, E. P. Lagioia, A. P. Milone, M. Fabrizio, I. Saviane, C. Moni Bidin, et al. (2014). "Strömgren and near-infrared photometry of metal-rich bulge globular clusters. I. NGC 6528 and its surrounding field". In: *A&A* 565, A8, A8. DOI: 10.1051/0004-6361/201323081. arXiv: 1402.0446 [astro-ph.GA] (cit. on p. 73).

Choi, J.-Y., C. Han, A. Udalski, T. Sumi, B. S. Gaudi, A. Gould, D. P. Bennett, et al. (2013). "Microlensing Discovery of a Population of Very Tight, Very Low Mass Binary Brown Dwarfs". In: *ApJ* 768, 129, p. 129. DOI: 10.1088/0004-637X/768/2/129. arXiv: 1302.4169 [astro-ph.SR].

Choi, J.-Y., I.-G. Shin, C. Han, A. Udalski, T. Sumi, A. Gould, V. Bozza, et al. (2012a). "A New Type of Ambiguity in the Planet and Binary Interpretations of Central Perturbations of High-magnification Gravitational Microlensing Events". In: *ApJ* 756, 48, p. 48. DOI: 10.1088/0004-637X/756/1/48. arXiv: 1204.4789 [astro-ph.EP].

Choi, J.-Y., I.-G. Shin, S.-Y. Park, C. Han, A. Gould, T. Sumi, A. Udalski, et al. (2012b). "Characterizing Lenses and Lensed Stars of High-magnification Single-lens Gravitational Microlensing Events with Lenses Passing over Source Stars". In: *ApJ* 751, 41, p. 41. DOI: 10.1088/0004-637X/751/1/41. arXiv: 1111.4032 [astro-ph.SR].

Clement, C. M., A. Muzzin, Q. Dufton, T. Ponnampalam, J. Wang, J. Burford, A. Richardson, et al. (2001). "Variable Stars in Galactic Globular Clusters". In: *AJ* 122, pp. 2587–2599. DOI: 10.1086/323719. eprint: astro-ph/0108024 (cit. on pp. 55, 69, 83, 84).

Clement, C. M. and I. Shelton (1997). "The Structure of the Light Curves of the RR Lyrae Variables in the Oosterhoff Type I Cluster NGC 6171". In: *AJ* 113, pp. 1711–1722. DOI: 10.1086/118387 (cit. on p. 85).

Coomber, G., C. O. Heinke, H. N. Cohn, P. M. Lugger, and J. E. Grindlay (2011). "The Unusual X-Ray Binaries of the Globular Cluster NGC 6652". In: *ApJ* 735, 95, p. 95. DOI: 10.1088/0004-637X/735/2/95. arXiv: 1105.2975 [astro-ph.HE] (cit. on pp. 79, 80).

Corwin, T. M., A. N. Sumerel, B. J. Pritzl, H. A. Smith, M. Catelan, A. V. Sweigart, and P. B. Stetson (2006). "Image-Subtraction Photometry of Variable Stars in the Globular Clusters NGC 6388 and NGC 6441". In: *AJ* 132, pp. 1014–1022. DOI: `10.1086/505745`. eprint: `astro-ph/0605569` (cit. on pp. 47, 56).

Deutsch, E. W., B. Margon, and S. F. Anderson (1998). "A Search for the Optical Counterpart of the Luminous X-Ray Source in NGC 6652". In: *AJ* 116, pp. 1301–1307. DOI: `10.1086/300512`. eprint: `astro-ph/9805280` (cit. on p. 79).

— (2000). "Ultracompact X-Ray Binaries in Globular Clusters: Variability of the Optical Counterpart of X1832-330 in NGC 6652". In: *ApJ* 530, pp. L21–L24. DOI: `10.1086/312486`. eprint: `astro-ph/9912259` (cit. on p. 79).

Díaz-Sánchez, A., A. Pérez-Garrido, I. Villó, R. Rebolo, J. A. Pérez-Prieto, A. Oscoz, S. R. Hildebrandt, et al. (2012). "High-resolution optical imaging of the core of the globular cluster M15 with FastCam". In: *MNRAS* 423, pp. 2260–2269. DOI: `10.1111/j.1365-2966.2012.21034.x`. arXiv: `1204.5340 [astro-ph.GA]` (cit. on p. 42).

Djorgovski, S. (1995). "Hot Stellar Populations in Globular Cluster Cores". In: *HST Proposal*, p. 6095 (cit. on p. 53).

Dominik, M., U. G. Jørgensen, F. V. Hessman, K. Horne, K. Harpsøe, J. Skottfelt, and MiNDSTEp Consortium (2011). "Exploring Hitherto Uncharted Planet Territory with Lucky-imaging Microlensing Observations". In: *AAS/Division for Extreme Solar Systems Abstracts*. Vol. 2. AAS/Division for Extreme Solar Systems Abstracts, p. 2101.

Dominik, M., U. G. Jørgensen, N. J. Rattenbury, M. Mathiasen, T. C. Hinse, S. Calchi Novati, K. Harpsøe, et al. (2010). "Realisation of a fully-deterministic microlensing observing strategy for inferring planet populations". In: *Astronomische Nachrichten* 331, p. 671. DOI: `10.1002/asna.201011400` (cit. on pp. 3, 37).

Draper, P. W. (2000). "GAIA: Recent Developments". In: *Astronomical Data Analysis Software and Systems IX*. Ed. by N. Manset, C. Veillet, and D. Crabtree. Vol. 216. Astronomical Society of the Pacific Conference Series, p. 615 (cit. on p. 53).

Dworetsky, M. M. (1983). "A period-finding method for sparse randomly spaced observations of 'How long is a piece of string?'" In: *MNRAS* 203, pp. 917–924 (cit. on pp. 44, 55).

Engel, M. C., C. O. Heinke, G. R. Sivakoff, K. G. Elshamouty, and P. D. Edmonds (2012). "A 2.15 hr Orbital Period for the Low-mass X-Ray Binary XB 1832-330 in the Globular Cluster NGC 6652". In: *ApJ* 747, 119, p. 119. DOI: `10.1088/0004-637X/747/2/119`. arXiv: `1201.4131 [astro-ph.HE]` (cit. on p. 79).

Feltzing, S. (2000). "Disentangling the Bulge and NGC 6528 - a proper motion study". In: *HST Proposal*, p. 8696 (cit. on p. 53).

Feltzing, S. and R. A. Johnson (2002). "A new, cleaner colour-magnitude diagram for the metal-rich globular cluster NGC 6528. Velocity dispersion in the Bulge, age and proper motion of NGC 6528". In: *A&A* 385, pp. 67–86. DOI: `10.1051/0004-6361:20011771`. eprint: `astro-ph/0201363` (cit. on pp. 73, 87).

Figuera Jaimes, R., A. Arellano Ferro, D. M. Bramich, S. Giridhar, and K. Kuppuswamy (2013). "Variable stars in the globular cluster NGC 7492. New discoveries and phys-

ical parameter determination". In: *A&A* 556, A20, A20. DOI: 10.1051/0004-6361/ 201220824. arXiv: 1305.4837 [astro-ph.SR] (cit. on p. 47).

Fourcade, C. R., J. R. Laborde, and J. D. Albarrracĭin (1964). "Atlas y catálogo de estrellas variables en cúmulos globulares al sur de -29°". In: *Boletin de la Asociacion Argentina de Astronomia La Plata Argentina* 8, p. 23 (cit. on p. 63).

Fried, D. L. (1966). "Optical Resolution Through a Randomly Inhomogeneous Medium for Very Long and Very Short Exposures". In: *Journal of the Optical Society of America (1917-1983)* 56, p. 1372 (cit. on p. 1).

— (1978). "Probability of getting a lucky short-exposure image through turbulence". In: *Journal of the Optical Society of America (1917-1983)* 68, pp. 1651–1658 (cit. on pp. 1, 8).

Frigo, Matteo and Steven G. Johnson (2005). "The Design and Implementation of FFTW3". In: *Proceedings of the IEEE* 93.2. Special issue on "Program Generation, Optimization, and Platform Adaptation", pp. 216–231 (cit. on p. 24).

Gaudi, B. S. (2012). "Microlensing Surveys for Exoplanets". In: *ARA&A* 50, pp. 411–453. DOI: 10.1146/annurev-astro-081811-125518 (cit. on pp. 3, 36).

Grundahl, F., J. Christensen-Dalsgaard, H. Kjeldsen, U. G. Jørgensen, T. Arentoft, S. Frandsen, and P. Kjærgaard (2009). "The Stellar Observations Network Group–the Prototype". In: *Solar-Stellar Dynamos as Revealed by Helio- and Asteroseismology: GONG 2008/SOHO 21*. Ed. by M. Dikpati, T. Arentoft, I. González Hernández, C. Lindsey, and F. Hill. Vol. 416. Astronomical Society of the Pacific Conference Series, p. 579. arXiv: 0908.0436 [astro-ph.SR] (cit. on p. 10).

Grundahl, F., J. Christensen-Dalsgaard, P. L. Pallé, M. F. Andersen, S. Frandsen, K. Harpsøe, U. G. Jørgensen, et al. (2014). "Stellar Observations Network Group: The prototype is nearly ready". In: *IAU Symposium*. Ed. by J. A. Guzik, W. J. Chaplin, G. Handler, and A. Pigulski. Vol. 301. IAU Symposium, pp. 69–75. DOI: 10.1017/ S1743921313014117 (cit. on p. 10).

Grundahl, F., H. Kjeldsen, S. Frandsen, M. Andersen, T. Bedding, T. Arentoft, and J. Christensen-Dalsgaard (2006). "SONG: Stellar Oscillations Network Group . A global network of small telescopes for asteroseismology and planet searches." In: *Mem. Soc. Astron. Italiana* 77, p. 458 (cit. on p. 10).

Gunn, J. E., M. Carr, C. Rockosi, M. Sekiguchi, K. Berry, B. Elms, E. de Haas, et al. (1998). "The Sloan Digital Sky Survey Photometric Camera". In: *AJ* 116, pp. 3040– 3081. DOI: 10.1086/300645. eprint: astro-ph/9809085 (cit. on p. 12).

Harpsøe, K. B. W., M. I. Andersen, and P. Kjægaard (2012a). "Bayesian photon counting with electron-multiplying charge coupled devices (EMCCDs)". In: *A&A* 537, A50, A50. DOI: 10.1051/0004-6361/201117089. arXiv: 1111.2066 [astro-ph.IM] (cit. on pp. 5, 6, 24).

Harpsøe, K. B. W., S. Hardis, T. C. Hinse, U. G. Jørgensen, L. Mancini, J. Southworth, K. A. Alsubai, et al. (2013). "The transiting system GJ1214: high-precision defocused transit observations and a search for evidence of transit timing variation". In: *A&A* 549, A10, A10. DOI: 10.1051/0004-6361/201219996. arXiv: 1207.3064 [astro-ph.EP].

Harpsøe, K. B. W., U. G. Jørgensen, M. I. Andersen, and F. Grundahl (2012b). "High frame rate imaging based photometry. Photometric reduction of data from electron-multiplying charge coupled devices (EMCCDs)". In: *A&A* 542, A23, A23. DOI: 10.1051/0004-6361/201219059. arXiv: 1202.3814 [astro-ph.IM] (cit. on pp. 5, 7, 23, 31, 32, 42, 43, 49, 51).

Harris, W. E. (1996). "A Catalog of Parameters for Globular Clusters in the Milky Way". In: *AJ* 112, p. 1487. DOI: 10.1086/118116 (cit. on p. 48).

Hazen, M. L. (1989). "The variable stars in the field of the globular cluster NGC 6652". In: *AJ* 97, pp. 771–776. DOI: 10.1086/115021 (cit. on pp. 48, 79).

Hazen, M. L. and B. H. Hesser (1986). "The variable stars in the globular cluster NGC 6388". In: *AJ* 92, pp. 1094–1099. DOI: 10.1086/114239 (cit. on p. 55).

Heinke, C. O., P. D. Edmonds, and J. E. Grindlay (2001). "Identification of the Low-Mass X-Ray Binary and Faint X-Ray Sources in NGC 6652". In: *ApJ* 562, pp. 363–367. DOI: 10.1086/323493. eprint: astro-ph/0107513 (cit. on p. 79).

Hesser, J. E. and F. D. A. Hartwick (1976). "Metal-rich globular clusters in the Galaxy. III - The 'X-ray' globular cluster NGC 6441. IV - A color-magnitude diagram for NGC 6304". In: *ApJ* 203, pp. 97–123. DOI: 10.1086/154052 (cit. on p. 63).

Kains, N., D. M. Bramich, A. Arellano Ferro, R. Figuera Jaimes, U. G. Jørgensen, S. Giridhar, M. T. Penny, et al. (2013a). "Estimating the parameters of globular cluster M 30 (NGC 7099) from time-series photometry". In: *A&A* 555, A36, A36. DOI: 10.1051/0004-6361/201321819. arXiv: 1305.3606 [astro-ph.SR] (cit. on p. 47).

Kains, N., D. M. Bramich, R. Figuera Jaimes, A. Arellano Ferro, S. Giridhar, and K. Kuppuswamy (2012). "Constraining the parameters of globular cluster NGC 1904 from its variable star population". In: *A&A* 548, A92, A92. DOI: 10.1051/0004-6361/201220217. arXiv: 1210.7242 [astro-ph.SR] (cit. on p. 47).

Kains, N., D. M. Bramich, R. F. Jaimes, and J. Skottfelt (2014). "LIMBO: A time-series Lucky Imaging survey of variability in Galactic globular clusters". In: *IAU Symposium*. Ed. by J. A. Guzik, W. J. Chaplin, G. Handler, and A. Pigulski. Vol. 301. IAU Symposium, pp. 435–436. DOI: 10.1017/S1743921313014920 (cit. on p. 37).

Kains, N., R. A. Street, J.-Y. Choi, C. Han, A. Udalski, L. A. Almeida, F. Jablonski, et al. (2013b). "A giant planet beyond the snow line in microlensing event OGLE-2011-BLG-0251". In: *A&A* 552, A70, A70. DOI: 10.1051/0004-6361/201220626. arXiv: 1303.1184 [astro-ph.EP].

Kholopov, P. N., N. N. Samus, M. S. Frolov, V. P. Goranskij, N. A. Gorynya, E. A. Karitskaya, E. V. Kazarovets, et al. (1998). "Combined General Catalogue of Variable Stars". In: *Combined General Catalogue of Variable Stars, 4.1 Ed (II/214A). (1998)*, (cit. on p. 55).

Konacki, M., G. Torres, S. Jha, and D. D. Sasselov (2003). "An extrasolar planet that transits the disk of its parent star". In: *Nature* 421, pp. 507–509. DOI: 10.1038/nature01379 (cit. on p. 30).

Kunder, A., P. B. Stetson, M. Catelan, A. R. Walker, and P. Amigo (2013). "Variable Stars in the Globular Cluster NGC 2808". In: *AJ* 145, 33, p. 33. DOI: 10.1088/0004-6256/145/2/33. arXiv: 1211.5147 [astro-ph.SR] (cit. on pp. 85, 86).

Law, N. M., C. D. Mackay, and J. E. Baldwin (2006). "Lucky imaging: high angular resolution imaging in the visible from the ground". In: *A&A* 446, pp. 739–745. DOI: `10.1051/0004-6361:20053695`. eprint: `arXiv:astro-ph/0507299` (cit. on pp. 2, 41).

Law, N. M., C. D. Mackay, R. G. Dekany, M. Ireland, J. P. Lloyd, A. M. Moore, J. G. Robertson, et al. (2009). "Getting Lucky with Adaptive Optics: Fast Adaptive Optics Image Selection in the Visible with a Large Telescope". In: *ApJ* 692, pp. 924–930. DOI: `10.1088/0004-637X/692/1/924`. arXiv: `0805.1921` (cit. on p. 2).

Layden, A. C., L. A. Ritter, D. L. Welch, and T. M. A. Webb (1999). "The Variable Stars and Blue Horizontal Branch of the Metal-rich Globular Cluster NGC 6441". In: *AJ* 117, pp. 1313–1331. DOI: `10.1086/300768`. eprint: `astro-ph/9808353` (cit. on p. 63).

Leloudas, G., M. D. Stritzinger, J. Sollerman, C. R. Burns, C. Kozma, K. Krisciunas, J. R. Maund, et al. (2009). "The normal Type Ia SN 2003hv out to very late phases". In: *A&A* 505, pp. 265–279. DOI: `10.1051/0004-6361/200912364`. arXiv: `0908.0537 [astro-ph.SR]`.

Lloyd Evans, T. and J. W. Menzies (1973). "Red Variables Stars in Metal Rich Globular Clusters". In: *IAU Colloq. 21: Variable Stars in Globular Clusters and in Related Systems*. Ed. by J. D. Fernie. Vol. 36. Astrophysics and Space Science Library, p. 151 (cit. on p. 55).

— (1977). "Near infrared photometry of globular clusters. III - The metal-rich clusters". In: *MNRAS* 178, pp. 163–193 (cit. on p. 55).

Mackay, C. D., J. Baldwin, N. Law, and P. Warner (2004). "High-resolution imaging in the visible from the ground without adaptive optics: new techniques and results". In: *Society of Photo-Optical Instrumentation Engineers (SPIE) Conference Series*. Ed. by A. F. M. Moorwood and M. Iye. Vol. 5492. Society of Photo-Optical Instrumentation Engineers (SPIE) Conference Series, pp. 128–135. DOI: `10.1117/12.550443` (cit. on pp. 2, 41).

Mackay, C. D., R. N. Tubbs, R. Bell, D. J. Burt, P. Jerram, and I. Moody (2001). "Subelectron read noise at MHz pixel rates". In: *Sensors and Camera Systems for Scientific, Industrial, and Digital Photography Applications II*. Ed. by M. M. Blouke, J. Canosa, and N. Sampat. Vol. 4306. Society of Photo-Optical Instrumentation Engineers (SPIE) Conference Series, pp. 289–298. eprint: `astro-ph/0101409` (cit. on p. 5).

Mancini, L., S. Ciceri, G. Chen, J. Tregloan-Reed, J. J. Fortney, J. Southworth, T. G. Tan, et al. (2013). "Physical properties, transmission and emission spectra of the WASP-19 planetary system from multi-colour photometry". In: *MNRAS* 436, pp. 2–18. DOI: `10.1093/mnras/stt1394`. arXiv: `1306.6384 [astro-ph.EP]`.

Mancini, L., J. Southworth, S. Ciceri, S. Calchi Novati, M. Dominik, T. Henning, U. G. Jørgensen, et al. (2014a). "Physical properties of the WASP-67 planetary system from multi-colour photometry". In: *A&A* 568, A127, A127. DOI: `10.1051/0004-6361/201424106`. arXiv: `1406.7448 [astro-ph.EP]` (cit. on p. 39).

Mancini, L., J. Southworth, S. Ciceri, M. Dominik, T. Henning, U. G. Jørgensen, A. F. Lanza, et al. (2014b). "Physical properties and transmission spectrum of the WASP-

80 planetary system from multi-colour photometry". In: *A&A* 562, A126, A126. DOI: 10.1051/0004-6361/201323265. arXiv: 1312.4982 [astro-ph.EP].

Mao, S. and B. Paczynski (1991). "Gravitational microlensing by double stars and planetary systems". In: *ApJ* 374, pp. L37–L40. DOI: 10.1086/186066 (cit. on p. 37).

Mattila, K., P. Vaeisaenen, and G. F. O. V. Appen-Schnur (1996). "Sky brightness at the ESO La Silla Observatory 1978 to 1988." In: *A&AS* 119, pp. 153–170 (cit. on p. 35).

Miyake, N., T. Sumi, S. Dong, R. Street, L. Mancini, A. Gould, D. P. Bennett, et al. (2011). "A Sub-Saturn Mass Planet, MOA-2009-BLG-319Lb". In: *ApJ* 728, 120, p. 120. DOI: 10.1088/0004-637X/728/2/120. arXiv: 1010.1809 [astro-ph.EP].

Muraki, Y., C. Han, D. P. Bennett, D. Suzuki, L. A. G. Monard, R. Street, U. G. Jorgensen, et al. (2011). "Discovery and Mass Measurements of a Cold, 10 Earth Mass Planet and Its Host Star". In: *ApJ* 741, 22, p. 22. DOI: 10.1088/0004-637X/741/1/22. arXiv: 1106.2160 [astro-ph.EP].

Oosterhoff, P. T. (1939). "Some remarks on the variable stars in globular clusters". In: *The Observatory* 62, pp. 104–109 (cit. on p. 83).

Ortolani, S., E. Bica, and B. Barbuy (1992). "CCD photometry of NGC 6528 - A high metallicity inner bulge globular cluster". In: *A&AS* 92, pp. 441–448 (cit. on p. 73).

Pallé, P. L., F. Grundahl, A. Triviño Hage, J. Christensen-Dalsgaard, S. Frandsen, R. A. García, K. Uytterhoeven, et al. (2013). "Observations of the radial velocity of the Sun as measured with the novel SONG spectrograph: results from a 1-week campaign". In: *Journal of Physics Conference Series* 440.1, 012051, p. 012051. DOI: 10.1088/1742-6596/440/1/012051.

Percy, J. R. (2007). *Understanding Variable Stars*. Cambridge University Press (cit. on p. 85).

Percy, J. R. and T. Brekelmans (2014). "A Study of Multiple-Mode Pulsating Red Giants". In: *ArXiv e-prints*. arXiv: 1407.4429 [astro-ph.SR] (cit. on p. 85).

Piotto, G. (1999). "A Snapshot Survey of Galactic Globular Clusters". In: *HST Proposal*, p. 8118 (cit. on p. 53).

Piotto, G., I. R. King, S. G. Djorgovski, C. Sosin, M. Zoccali, I. Saviane, F. De Angeli, et al. (2002). "HST color-magnitude diagrams of 74 galactic globular clusters in the HST F439W and F555W bands". In: *A&A* 391, pp. 945–965. DOI: 10.1051/0004-6361:20020820. eprint: astro-ph/0207124 (cit. on pp. 54, 86).

Plaut, L. (1971). "Variable stars in a field centred at l^{II} = 0°, b^{II} = -10° (field 3 of the Palomar-Groningen variable-star survey)". In: *A&AS* 4, p. 75 (cit. on p. 79).

Pritzl, B. J., H. A. Smith, M. Catelan, and A. V. Sweigart (2001). "Variable Stars in the Unusual, Metal-Rich, Globular Cluster NGC 6441". In: *AJ* 122, pp. 2600–2626. DOI: 10.1086/323447. eprint: astro-ph/0107341 (cit. on pp. 47, 64–66).

— (2002). "Variable Stars in the Unusual, Metal-rich Globular Cluster NGC 6388". In: *AJ* 124, pp. 949–976. DOI: 10.1086/341381. eprint: astro-ph/0204296 (cit. on pp. 47, 56, 59).

Pritzl, B. J., H. A. Smith, P. B. Stetson, M. Catelan, A. V. Sweigart, A. C. Layden, and R. M. Rich (2003). "Hubble Space Telescope Snapshot Study of Variable Stars in

Globular Clusters: The Inner Region of NGC 6441". In: *AJ* 126, pp. 1381–1401. DOI: 10.1086/377024. eprint: `astro-ph/0305339` (cit. on pp. 47, 64).

Pritzl, B., H. A. Smith, M. Catelan, and A. V. Sweigart (2000). "RR Lyrae Stars in NGC 6388 and NGC 6441: A New Oosterhoff Group?" In: *ApJ* 530, pp. L41–L44. DOI: 10.1086/312482. eprint: `astro-ph/9912217` (cit. on p. 83).

Ricci, D., A. Elyiv, F. Finet, O. Wertz, K. Alsubai, T. Anguita, V. Bozza, et al. (2013). "Flux and color variations of the doubly imaged quasar UM673". In: *A&A* 551, A104, A104. DOI: 10.1051/0004-6361/201118755. arXiv: 1302.0766 `[astro-ph.CO]`.

Ricci, D., J. Poels, A. Elyiv, F. Finet, P. G. Sprimont, T. Anguita, V. Bozza, et al. (2011). "Flux and color variations of the quadruply imaged quasar HE 0435-1223". In: *A&A* 528, A42, A42. DOI: 10.1051/0004-6361/201016188. arXiv: 1101.3664 `[astro-ph.CO]`.

Richtler, T., E. K. Grebel, A. Subramaniam, and R. Sagar (1998). "VI CCD photometry of metal-rich globular clusters: NGC 6528". In: *A&AS* 127, pp. 167–179. DOI: 10.1051/aas:1998341 (cit. on p. 73).

Robin, A. C., C. Reylé, S. Derrière, and S. Picaud (2003). "A synthetic view on structure and evolution of the Milky Way". In: *A&A* 409, pp. 523–540. DOI: 10.1051/0004-6361:20031117 (cit. on p. 27).

Roediger, J. C., S. Courteau, G. Graves, and R. P. Schiavon (2014). "Constraining Stellar Population Models. I. Age, Metallicity and Abundance Pattern Compilation for Galactic Globular Clusters". In: *ApJS* 210, 10, p. 10. DOI: 10.1088/0067-0049/210/1/10. arXiv: 1310.3275 `[astro-ph.GA]` (cit. on p. 48).

Rutily, B. and A. Terzan (1977). "Detection and study of variable stars in the globular cluster NGC 6638." In: *A&AS* 30, pp. 315–322 (cit. on pp. 48, 75).

Ryu, Y.-H., C. Han, K.-H. Hwang, R. Street, A. Udalski, T. Sumi, A. Fukui, et al. (2010). "OGLE-2009-BLG-092/MOA-2009-BLG-137: A Dramatic Repeating Event with the Second Perturbation Predicted by Real-time Analysis". In: *ApJ* 723, pp. 81–88. DOI: 10.1088/0004-637X/723/1/81. arXiv: 1009.0338 `[astro-ph.SR]`.

Sarajedini, A., L. R. Bedin, B. Chaboyer, A. Dotter, M. Siegel, J. Anderson, A. Aparicio, et al. (2007). "The ACS Survey of Galactic Globular Clusters. I. Overview and Clusters without Previous Hubble Space Telescope Photometry". In: *AJ* 133, pp. 1658–1672. DOI: 10.1086/511979. eprint: `astro-ph/0612598` (cit. on pp. 34, 54).

Sawyer Hogg, H. (1973). "A third catalogue of variable stars in globular clusters comprising 2119 entries." In: *Publications of the David Dunlap Observatory* 3, p. 6 (cit. on pp. 55, 73).

Sawyer Hogg, H., B. Rutily, and A. Terzan (1974). "26 nouvelles étoiles variables dans l'amas globulaire NGC 6638." In: *Academie des Sciences Paris Comptes Rendus Serie B Sciences Physiques* 279, pp. 333–335 (cit. on p. 75).

Shin, I.-G., J.-Y. Choi, S.-Y. Park, C. Han, A. Gould, T. Sumi, A. Udalski, et al. (2012a). "Microlensing Binaries Discovered through High-magnification Channel". In: *ApJ* 746, 127, p. 127. DOI: 10.1088/0004-637X/746/2/127. arXiv: 1109.3295 `[astro-ph.SR]`.

Shin, I.-G., C. Han, J.-Y. Choi, A. Udalski, T. Sumi, A. Gould, V. Bozza, et al. (2012b). "Characterizing Low-mass Binaries from Observation of Long-timescale Caustic-crossing Gravitational Microlensing Events". In: *ApJ* 755, 91, p. 91. DOI: `10.1088/0004-637X/755/2/91`. arXiv: `1204.2869 [astro-ph.SR]`.

Shin, I.-G., C. Han, A. Gould, A. Udalski, T. Sumi, M. Dominik, J.-P. Beaulieu, et al. (2012c). "Microlensing Binaries with Candidate Brown Dwarf Companions". In: *ApJ* 760, 116, p. 116. DOI: `10.1088/0004-637X/760/2/116`. arXiv: `1208.2323 [astro-ph.SR]`.

Silbermann, N. A., H. A. Smith, M. Bolte, and M. L. Hazen (1994). "RR Lyrae stars and color-magnitude diagram of the globular cluster NGC 6388". In: *AJ* 107, pp. 1764–1772. DOI: `10.1086/116984` (cit. on p. 56).

Sirianni, M., M. J. Jee, N. Benítez, J. P. Blakeslee, A. R. Martel, G. Meurer, M. Clampin, et al. (2005). "The Photometric Performance and Calibration of the Hubble Space Telescope Advanced Camera for Surveys". In: *PASP* 117, pp. 1049–1112. DOI: `10.1086/444553`. eprint: `astro-ph/0507614` (cit. on p. 34).

Skottfelt, J., D. M. Bramich, R. Figuera Jaimes, U. G. Jørgensen, N. Kains, A. Arrellano Ferro, K. A. Alsubai, et al. (2014a). "Searching for variable stars in the cores of five metal rich globular clusters using EMCCD observations". In: *Accepted to A&A*. arXiv: `1410.8827 [astro-ph.SR]` (cit. on pp. 4, 32, 37).

Skottfelt, J., D. M. Bramich, R. Figuera Jaimes, U. G. Jorgensen, N. Kains, K. B. W. Harpsoe, C. Liebig, et al. (2013a). "VizieR Online Data Catalog: Light curves of two NGC6981 variables (Skottfelt+, 2013)". In: *VizieR Online Data Catalog* 355, p. 39111.

Skottfelt, J., D. M. Bramich, R. Figuera Jaimes, U. G. Jørgensen, N. Kains, K. B. W. Harpsøe, C. Liebig, et al. (2013b). "EMCCD photometry reveals two new variable stars in the crowded central region of the globular cluster NGC 6981". In: *A&A* 553, A111, A111. DOI: `10.1051/0004-6361/201321430`. arXiv: `1304.2243 [astro-ph.SR]` (cit. on pp. 4, 32, 37, 47, 48).

Skottfelt, J., D. M. Bramich, M. Hundertmark, U. G. Jørgensen, P. Kjærgaard, N. Michaelsen, J. Southworth, et al. (2014b). "(The Two-Colour EMCCD Instrument for the Danish 1.54m Telescope and SONG)". In: *Submitted on 01/11/2014 to A&A*.

Smith, A. M. S. and WASP Consortium (2014). "The SuperWASP exoplanet transit survey". In: *Contributions of the Astronomical Observatory Skalnate Pleso* 43, pp. 500–512.

Smith, A., J. Bailey, J. H. Hough, and S. Lee (2009). "An investigation of lucky imaging techniques". In: *MNRAS* 398, pp. 2069–2073. DOI: `10.1111/j.1365-2966.2009.15249.x`. arXiv: `0906.3041 [astro-ph.IM]` (cit. on pp. 8, 24, 27, 50).

Smith, H. A. (1995). "RR Lyrae stars." In: *Cambridge Astrophysics Series* 27 (cit. on pp. 41, 45, 83).

Southworth, J. (2008). "Homogeneous studies of transiting extrasolar planets - I. Light-curve analyses". In: *MNRAS* 386, pp. 1644–1666. DOI: `10.1111/j.1365-2966.2008.13145.x`. arXiv: `0802.3764` (cit. on p. 31).

— (2012). "Homogeneous studies of transiting extrasolar planets - V. New results for 38 planets". In: *MNRAS* 426, pp. 1291–1323. DOI: 10.1111/j.1365-2966.2012.21756.x. arXiv: 1207.5796 [astro-ph.EP] (cit. on pp. 30, 31).

Southworth, J., T. C. Hinse, M. Burgdorf, S. Calchi Novati, M. Dominik, P. Galianni, T. Gerner, et al. (2014). "High-precision photometry by telescope defocussing - VI. WASP-24, WASP-25 and WASP-26". In: *MNRAS* 444, pp. 776–789. DOI: 10.1093/mnras/stu1492. arXiv: 1407.6253 [astro-ph.EP] (cit. on p. 39).

Southworth, J., T. C. Hinse, M. Dominik, X.-S. Fang, K. Harpsøe, U. G. Jørgensen, E. Kerins, et al. (2012). "High-precision photometry by telescope defocusing - IV. Confirmation of the huge radius of WASP-17 b". In: *MNRAS* 426, pp. 1338–1348. DOI: 10.1111/j.1365-2966.2012.21781.x. arXiv: 1207.5797 [astro-ph.EP].

Southworth, J., T. C. Hinse, M. Dominik, M. Glitrup, U. G. Jørgensen, C. Liebig, M. Mathiasen, et al. (2009a). "Physical Properties of the 0.94-Day Period Transiting Planetary System WASP-18". In: *ApJ* 707, 167, pp. 167–172. DOI: 10.1088/0004-637X/707/1/167. arXiv: 0910.4875 [astro-ph.EP].

Southworth, J., T. C. Hinse, U. G. Jørgensen, M. Dominik, D. Ricci, M. J. Burgdorf, A. Hornstrup, et al. (2009b). "High-precision photometry by telescope defocusing - I. The transiting planetary system WASP-5". In: *MNRAS* 396, pp. 1023–1031. DOI: 10.1111/j.1365-2966.2009.14767.x. arXiv: 0903.2139 [astro-ph.EP] (cit. on pp. 30, 31, 39).

Southworth, J., L. Mancini, P. Browne, M. Burgdorf, S. Calchi Novati, M. Dominik, T. Gerner, et al. (2013). "High-precision photometry by telescope defocusing - V. WASP-15 and WASP-16". In: *MNRAS* 434, pp. 1300–1308. DOI: 10.1093/mnras/stt1089. arXiv: 1306.3509 [astro-ph.EP].

Southworth, J., L. Mancini, S. C. Novati, M. Dominik, M. Glitrup, T. C. Hinse, U. G. Jørgensen, et al. (2010). "High-precision photometry by telescope defocusing - III. The transiting planetary system WASP-2". In: *MNRAS* 408, pp. 1680–1688. DOI: 10.1111/j.1365-2966.2010.17238.x. arXiv: 1006.4464 [astro-ph.EP] (cit. on p. 39).

Spergel, D., N. Gehrels, J. Breckinridge, M. Donahue, A. Dressler, B. S. Gaudi, T. Greene, et al. (2013). "Wide-Field InfraRed Survey Telescope-Astrophysics Focused Telescope Assets WFIRST-AFTA Final Report". In: *ArXiv e-prints*. arXiv: 1305.5422 [astro-ph.IM] (cit. on p. 2).

Stacey, W. S., C. O. Heinke, H. N. Cohn, P. M. Lugger, and A. Bahramian (2012). "An Examination of the X-Ray Sources in the Globular Cluster NGC 6652". In: *ApJ* 751, 62, p. 62. DOI: 10.1088/0004-637X/751/1/62. arXiv: 1204.0552 [astro-ph.HE] (cit. on pp. 79, 80).

Stellingwerf, R. F. (1978). "Period determination using phase dispersion minimization". In: *ApJ* 224, pp. 953–960. DOI: 10.1086/156444 (cit. on p. 55).

Stetson, P. B. (1987). "DAOPHOT - A computer program for crowded-field stellar photometry". In: *PASP* 99, pp. 191–222. DOI: 10.1086/131977 (cit. on pp. 30, 32, 83).

Stetson, P. B. (1994). "The center of the core-cusp globular cluster M15: CFHT and HST Observations, ALLFRAME reductions". In: *PASP* 106, pp. 250–280. DOI: 10.1086/133378 (cit. on p. 83).

Terzan, A. (1968). "Nouvelles etoiles variables autour des amas globulaires NGC 6304, 6638, et 7099 (M 30)". In: *Publications of the Observatoire Haute-Provence* 9, p. 24 (cit. on p. 75).

The HDF Group (1997-2014). *Hierarchical Data Format, version 5*. http://www.hdfgroup.org/HDF5/ (cit. on p. 25).

Tsapras, Y., J.-Y. Choi, R. A. Street, C. Han, V. Bozza, A. Gould, M. Dominik, et al. (2014). "A Super-Jupiter Orbiting a Late-type Star: A Refined Analysis of Microlensing Event OGLE-2012-BLG-0406". In: *ApJ* 782, 48, p. 48. DOI: 10.1088/0004-637X/782/1/48. arXiv: 1310.2428 [astro-ph.EP] (cit. on p. 4).

Uytterhoeven, K., P. L. Palle, F. Grundahl, S. Frandsen, H. Kjeldsen, J. Christensen-Dalsgaard, M. Fredslund Andersen, et al. (2011). "The SONG project and the prototype node at Tenerife". In: *ArXiv e-prints*. arXiv: 1111.1834 [astro-ph.IM].